Development of an Extracellular Vesicle Microfluidic Affinity Purification (EV-MAP) In Vitro Assay for Breast Cancer Management

By

© 2019

Virginia Brown

B.Sc., Kansas State University, 2017

Submitted to the graduate degree program in Bioengineering and the Graduate Faculty of the University of Kansas in partial fulfillment of the requirements
for the degree of Master of Science.

_____

Chair: Dr. Steven Soper

_____

Dr. Sue Lunte

_____

Dr. Arghya Paul

Date Defended: 22 July 2019

The thesis committee for Virginia Brown certifies that this is the
approved version of the following thesis:

Development of an Extracellular Vesicle Microfluidic Affinity Purification (EV-MAP) In Vitro Assay for Breast Cancer Management

_____

Chair: Dr. Steven Soper

Date Approved: 22 July 2019

Abstract

Breast cancer is the second-most prevalent cancer worldwide and most commonly occurring cancer type in women with roughly 2 million new cases diagnosed in 2018. Current breast cancer management is a multidisciplinary approach which uses imaging for detection and monitoring, and tissue biopsy for diagnosis. Limitations within these technologies shifted focus toward liquid biopsies which are minimally invasive, allow for frequent sampling with a simple blood draw, and represent the heterogeneity of the cancer. One biomarker recently discovered for use in liquid biopsies are extracellular vesicles (EVs). Their ability to stably carry mRNA through circulation makes them a potentially suitable marker for mRNA expression profiling, a diagnostic method currently implemented in breast cancer management. Herein, an EV microfluidic affinity purification (EV-MAP) device was developed for selective isolation of disease-associated EVs for mRNA expression analysis. The EV-MAP assay produced a $99 \pm 1\%$ specificity for the gene panel used in this study through the implementation of 1% PVP-40/1% BSA blocking and 0.2% Tween 20® washing agents . A proteolytic digestion strategy using proteinase K and subsequent sonication was developed to remove EVs from the device surfaces and produced a release efficiency of $99 \pm 1\%$. EV-MAP also captured two distinct populations of disease-associated EVs through orthogonal markers either selecting for mesenchymal or epithelial-derived EVs, with one population showing gene expression profiling differences from the cells of origin while the mesenchymal populations resulted in similar mRNA expression profiles to their host cells. Finally, healthy controls and breast cancer patient samples were processed through the EV-MAP assay. ddPCR of these samples resulted in several genes showing copy numbers below the limit of detection of ddPCR, thereby highlighting the mass limitations associated with analyzing mRNA in EVs using the EV-MAP gene panel.

Acknowledgements

First and foremost, I would like to thank my advisor Professor Steven Allen Soper for his guidance and advice throughout the EV-MAP project. Without his help, this thesis would not have been possible. I would also like to thank my committee members Professor Arghya Paul and Professor Sue Lunte for their support and understanding, always willing to meet if I have questions or concerns and helping me feel comfortable and prepared throughout the process. I would also like to thank Assistant Research Professor Maggie Witek for helping me brainstorm solutions to any issues occurring during my research and teaching me experimental techniques in the lab.

Lastly, I would like to thank Dr. Matt Jackson for collaborating with me on this project. You gave an enumerable amount of your time and effort to helping me understand the biology, chemistry, and physics behind developing the EV-MAP device. This thesis and work would not have been possible without his Monte Carlo simulations used in designing the EV-MAP device or his guidance every step of the way thereafter. He was a wonderful mentor and really made this experience the rich resource of knowledge and skills that it came to be. I am extremely grateful and fortunate for having had the opportunity to work with him.

Table of Contents

Table of Figures

Table of Tables

List of Abbreviations

List of abbreviations

DCIS – ductal carcinoma in situ

LCIS – lobular carcinoma in situ

BRCA 1 – BReast CAncer gene 1

BRCA 2 – BReast CAncer gene 2

USPSTF – United States Preventive Service Task Force

ACS – American Cancer Society

ACR – American College of Radiology

PPV – Positive predictive value

NCCN - National Comprehensive Cancer Network

MRI – Magnetic resonance imaging

BI-RADS – Breast Imaging Reporting and Data System

AJCC – American Joint Committee on Cancer

TNM – "Tumor size", "nodal status", and "metastases"

CT – Computed tomography

American Society of Clinical Oncology (ASCO)

ER – Estrogen receptor

PR – Progesterone receptor

HER2 – Human epidermal growth factor receptor 2

EMT – Epithelial – to – mesenchymal transition

EpCAM – Epithelial cell adhesion molecule

VIM – Vimentin

FAPα – Fibroblast activation protein alpha

TRNA – Total RNA

RT – Reverse transcription

qPCR – quantitative PCR

FFPE – Formalin fixed parrafin embedded

PAM50 – Prediction Analysis of Microarray 50

FDA – Food and drug administration

HR – hormone receptors

MRD – Minimal residual disease

PET – Positron emission tomography

FDG – Fluorodeoxyglucose

MBC – Metastatic breast cancer

CEA - Carcinoembryonic Antigen

CA 15-3 – Cancer Antigen 15-3

CA 27.29 – Cancer Antigen 27.29

CTCs – Circulating Tumor Cells

Ab – Antibody

CK – Cytokeratin

CD45 – Cluster of differentiation 45

DAPI – 4',6-diamidino-2-phenylindole

cfDNA – cell-free DNA

ctDNA – circulating tumor DNA

EV – Extracellular vesicles

miRNA – micro RNA

messenger RNA - (mRNA)

ILV – Intraluminal vesicles

MVB – Multivesicular bodies

HSP – Heat shock proteins

tRNA – transfer RNA

piRNA – piwi-interacting RNA

lncRNA – long non-coding RNA

snRNA – short non-coding RNA

snoRNA – small nuclear RNA

rRNA – ribosomal RNA

PEG – polyethylene glycol

EV-MAP – Extracellular Vesicle Microfluidic Affinity Purification

mAbs – monoclonal antibody

COC – Cyclic olefin copolymer

EDC – 1-Ethyl-3-(3-dimethylaminopropyl)-carbodiimide)

NHS – N-hydroxysuccinimide

MES – 2-(N-morpholino) ethanesulfonic acid

ACN – Acetonitrile

PBS – Phosphate buffer saline

SDS – Sodium dodecyl sulfate

CD81 – Cluster of differentiation 81

MEM – Minimum essential medium eagle

FBS – Fetal bovine serum

KUMC – University of Kansas Medical center

EDTA – Ethylenediaminetetraacetic acid

BRCF – Biospecimen Repository Core Facility

IMC – Invasive mammary carcinoma

IDC – Invasive ductal carcinoma

NTA – Nanoparticle tracking analysis

TEM – Transmission electron microscopy

RT- Reverse transcription

cDNA – complementary DNA

ddPCR – droplet digital PCR

dsDNA – double stranded DNA

PMMA – Poly(methyl methacrylate)

Ag – Antigen

SDS-PAGE – Sodium dodecyl sulfate – polyacrylamide gel electrophoresis

BSA – Bovine serum albumin

NPs – Nanoparticles

PVP-40 – Polyvinylpyrolidone, 40 kDa

ELISA – Enzyme-Linked Immunosorbent Assay

dPCR – digital PCR

Ct – Cycle threshold

CK19 – Cytokeratin 19

IL8 – Interleukin 8

CD24 – Cluster of differentiation 24

CD44 – Cluster of differentiation 44

WTA – Whole transcriptome amplification

TdT – Terminal deoxynucleotidyl transferase

dATPs – Deoxyadenosine triphosphates

ssDNA – Single stranded DNA

LiDS – Lithium dodecyl sulfate

Chapter 1. Introduction

1.1 Breast cancer – Prevalence and risk factors

Nearly 10 million people worldwide died from cancer in 2018 [1]. Cancer is the second leading cause of death in the United States (**Figure 1**) only behind heart diseases and accounted for 22% of all deaths in 2017 [2]. The American Cancer Society estimates 1,762,450 new cases for 2019 [3]. The high occurrence and mortality rates highlight a need to improve upon technologies or tools for early detection, diagnosis, monitoring of treatment response, and detecting relapse.
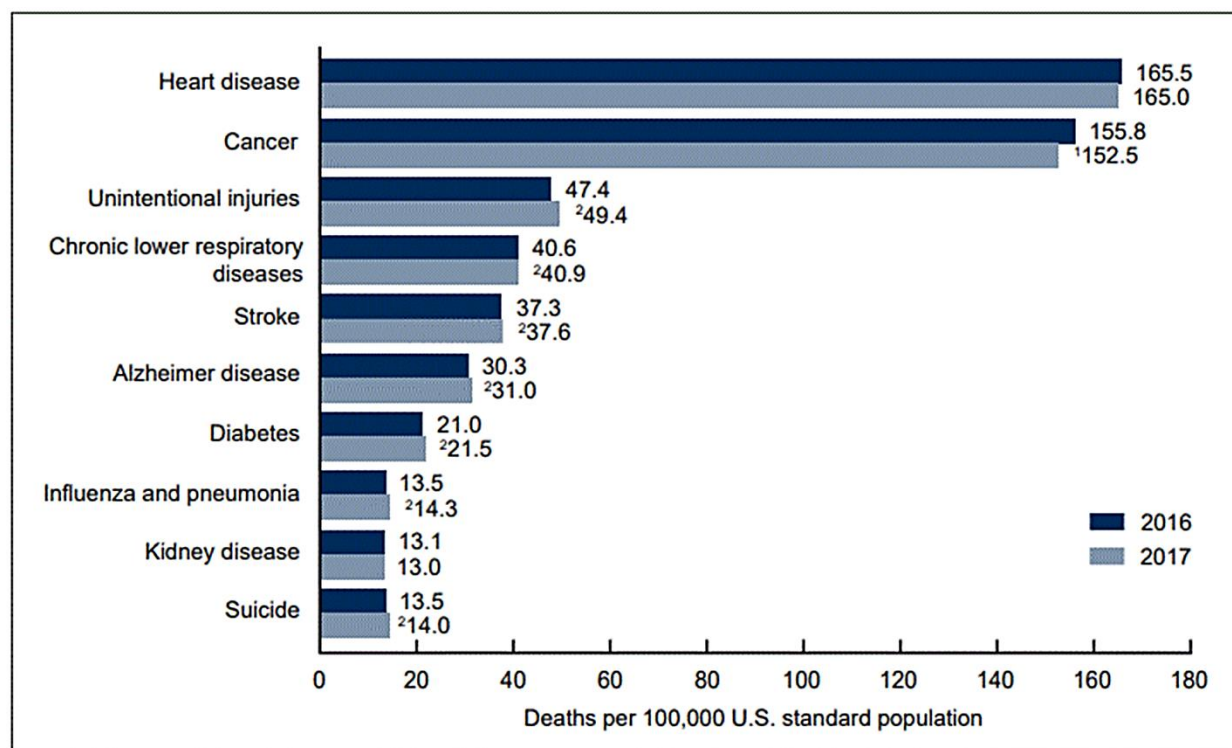
Figure 1. Death Rates in the United States from 2016 and 2017.

Only the 10 leading causes of death are included in this graph, with death rates age-adjusted. [1]Statistically significant decrease in mortality rates from 2016 to 2017 with a p-value < 0.05. [2]Statistically significant increase in mortality rates from 2016 to 2017 from a p-value < 0.05. Reproduced from "Mortality in the United States, 2017," by S. L. Murry, J. Xu, K. D. Kochanek, and E. Arias, 2018. [2].

Of all cancer cases, 80-90% are carcinomas [4], originating in the epithelial tissue that forms the skin and lines organs and body cavities, such as the chest. Carcinomas are further classified based on the type of epithelial cells – squamous cell carcinomas, basal cell carcinomas, and adenocarcinomas. Adenocarcinomas form in glandular cells capable of secretion, which keeps tissues moist, and form in organs or glands capable of secretion such as the breasts [4].

Breast cancer is the second most common type of cancer worldwide (**Figure 2A**) and was estimated to cause 626,679 deaths in 2018 according to the International Society of Cancer Research (ISCR) [1]. When categorizing cancer cases and fatalities based on sex, breast cancer is the most common in women (**Figure 2B**) [1], accounting for 15% of the estimated new cancer cases in the United States [3]. One in eight women will develop an *invasive* breast cancer in their lifetime, which can spread from the primary tumor into the surrounding soft tissue.

If a breast cancer is non-invasive, it is considered in situ and remains at the site of origin. The two main types of non-invasive or in situ breast cancers are ductal carcinoma in situ (DCIS) and lobular carcinoma in situ (LCIS). Yet, 80% of all breast cancer cases in the United States are invasive [5]. Invasive breast carcinomas can be differentiated into 21 histological subtypes [5] depending on the original cancer site or the architecture of the tissue and cells. **Table 1** lists the estimated prevalence and mortality of in situ and invasive breast cancers by age for 2017 [6]. Other non-carcinoma breast cancer types exist as well, such as pagets disease of the nipple, inflammatory breast cancer, and breast sarcomas. However, these types combined account for less than 10% of the total breast cancer cases diagnosed in the United States [7].

A

Incidence Rate in both sexes

Lung 11.6%
Breast 11.6%
Colorectum 10.2%
Prostate 7.1%
Stomach 5.7%
Liver 4.7%
Esophagus 3.2%
Cervix uteri 3.2%
Thyroid 3.1%
Bladder 3.0%
Other 36.6%

(Estimated new cases: 18.1 million)

B   **Incidence Rate**

Other 28.9%
Breast 24.2%
Colorectum 9.5%
Lung 8.4%
Cervix uteri 6.6%
Thyroid 5.1%
Corpus uteri 4.4%
Stomach 4.1%
Ovary 3.4%
Liver 2.8%
Non-Hodgkin lymphoma 2.6%

(Estimated new cases: 8.6 million)

Mortality Rate

Breast 15.0%
Lung 13.8%
Colorectum 9.5%
Cervix uteri 7.5%
Stomach 6.5%
Liver 5.6%
Pancreas 4.9%
Ovary 4.4%
Esophagus 3.6%
Leukaemia 3.1%
Other 23.1%

(Estimated new cases: 4.2 million)

Figure 2. Estimated new cases and deaths for the 10 most common cancer types worldwide from 2018. (**A**) Estimated incidence rates (out of 18.1 million total cases) of cancers in both sexes separated by cancer type. (**B**) Incidence and mortality rates (out of 8.6 and 4.2 million estimated cases, respectively) for women. Reproduced with permission from John Wiley and Sons: "Global Cancer Statistics 2018: GLOBOCAN Estimates of Incidence and Mortality Worldwide for 36 Cancers in 185 Countries," by F. Bray et al., 2018, CA: a cancer journal for clinicians, 68:6, p. 400, © 2018 by the American Cancer Society [1].

Most women develop breast cancer after the age of 40, with the highest occurrence found in women between the ages of 50 and 70 (**Table 1**) [6]. Age plays an important role in the overall risk, along with other risk factors such as inherited conditions, past treatment with hormonal therapy, and a high density of breast tissue (ratio of fatty tissue to glandular tissue).

For example, women with dense breast tissue are five times more likely to develop breast cancer than the average-risk population [8]. More than 50% of women in the United states live with dense breast tissue [9], making this a highly prevalent risk factor affecting not only the potential for developing breast cancer but also the performance of screening modalities. Furthermore, though most breast cancer cases diagnosed do not correlate with family history, females who inherit mutations in the *BRCA1* or *BRCA2* genes have a 60% higher risk in developing breast cancer compared to the general population [10]. Screening is often the first step in breast cancer clinical management for average-risk individuals, but high-risk patients may receive additional genetic counseling and risk assessment either preceding or in conjunction with routine screening. For example, doctors may suggest women with *BRCA1* or *BRCA2* mutations undergo genetic counseling [5] to determine whether high-risk screening modalities are beneficial over the screening methods routinely used for average-risk individuals.

Table 1. Estimated in situ and invasive breast cancer cases and mortalities in 2017 in the United States
These cases are further categorized based on the 10-year age group with which they are most expected to develop. Percentages may not sum to 100 because estimates were rounded to the nearest ten. Reproduced with permission from John Wiley and Sons: "Breast Cancer Statistics, 2017, racial disparity in mortality by state," by C. E. DeSantis et al., 2017, CA: a cancer journal for clinicians, 67:6, p. 440. © 2017 by the American Cancer Society [6].

Age	In situ cases No.	%	Invasive cases No.	%	Deaths No.	%
< 40	1,610	3%	11,160	4%	990	2%
40-49	12,440	20%	36,920	15%	3,480	9%
50-59	17,680	28%	58,620	23%	7,590	19%
60-69	17,550	28%	68,070	27%	9,420	23%
70-79	10,370	16%	47,860	19%	8,220	20%
80 +	3,760	6%	30,080	12%	10,910	27%
All ages	**63,410**		**252,710**		**40,610**	

Figure 3 outlines the general sequence of events in the medical care of breast cancer, from screening to treatment and surveilling recurrence. This management pathway is a multidisciplinary process that involves various forms of testing to accurately detect, diagnose, monitor treatment, and survey for disease recurrence. It is important for each patient to communicate with their physician and vice versa to ensure the process flow is beneficial to each unique individual with the final aim of curing disease or prolonging life.
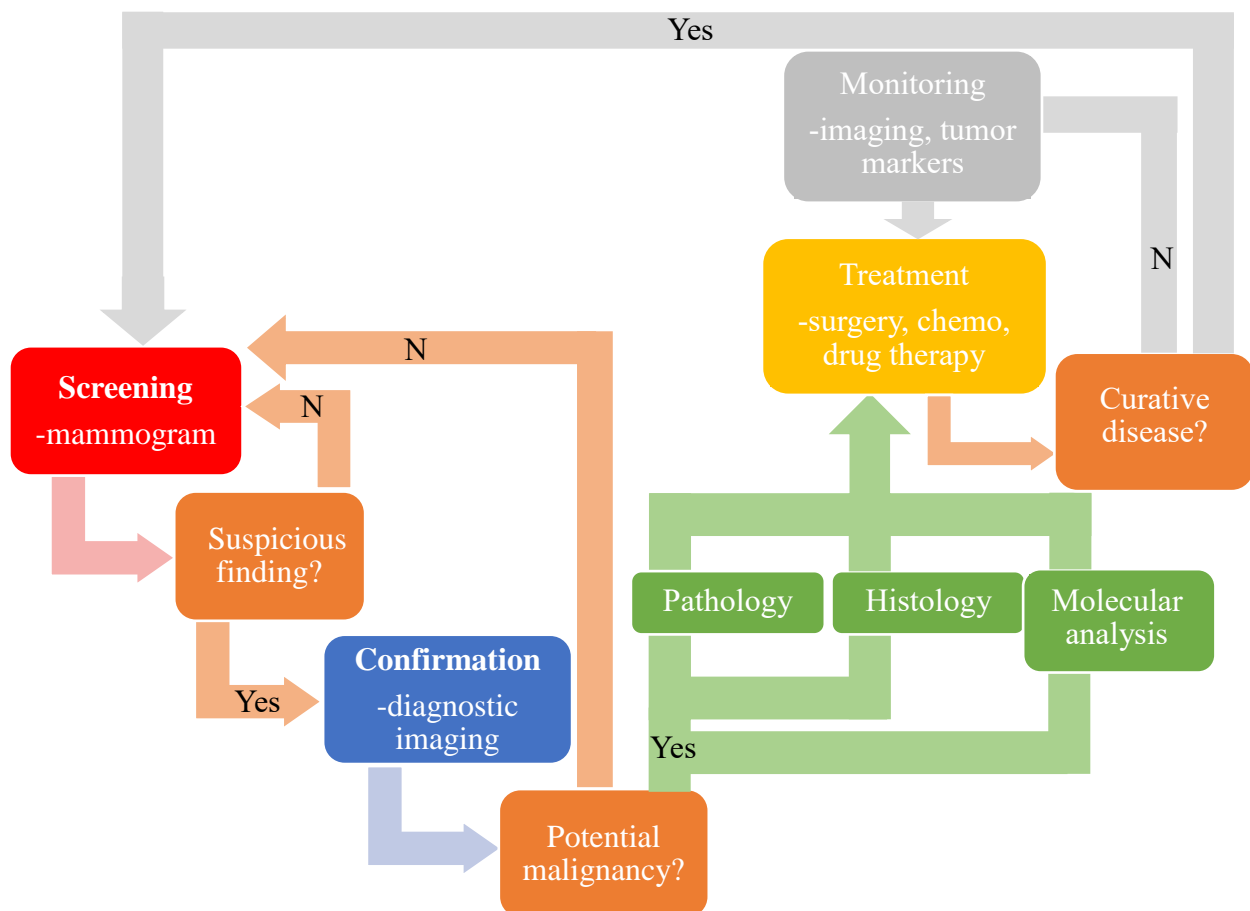
Figure 3. Flow chart outlining the general breast cancer management pathway.
Screening serves to detect cancer early. If an abnormality is present or symptoms arise, further analysis of the suspicious lesion is often performed through secondary imaging to detect false positives resulting from screening tools. If the imaging results show potential malignancy, official diagnosis of the disease includes a pathological review of the tissue to stage the disease as well as imaging in certain cases where systemic disease may be present. Various treatment options may be administered, with monitoring of the response to treatment occurring particularly in cases of non-curative disease. Patients showing complete response to primary treatment undergo surveillance to detect recurrence of disease.

Breast cancer is detected through either a routine mammogram or a mammogram prescribed to a patient based on physical signs of breast cancer such as breast swelling, pain, or redness. Some patients may undergo diagnostic imaging to help identify any benign lesions or clinically occult cancer. If the abnormality is still suspected of being malignant, a tissue biopsy is performed and analyzed to stage the disease (pathology), assign a grade (histology), and analyze the molecular components (molecular analysis) to formulate a treatment plan. If the breast cancer spreads to other locations in the body (metastasizes), the goal of treatment is to prolong life and requires monitoring the patient's response. However, upon conclusion of curative treatment, patients are surveilled using the same methods applied for screening. Each of these breast cancer management steps will be discussed further below.

1.2 Breast cancer clinical management

1.2.2 Screening

Clinically oriented organizations such as the U.S. Preventive Services Task Force (USPSTF), American Cancer Society (ACS), and American College of Radiology (ACR) developed screening guidelines to standardize early detection of breast cancer. All suggest mammography screening starting at the age of 50, while some recommend giving women the option to screen from the age of 40 to 49 for average-risk patients [11-13]. This age range is determined based on the higher incurred risk of developing cancer in women between 50-69 years of age, with risk slightly increasing as early as the age of 40.

| Normal breast | Breast cyst | Calcification | Cancer mass |
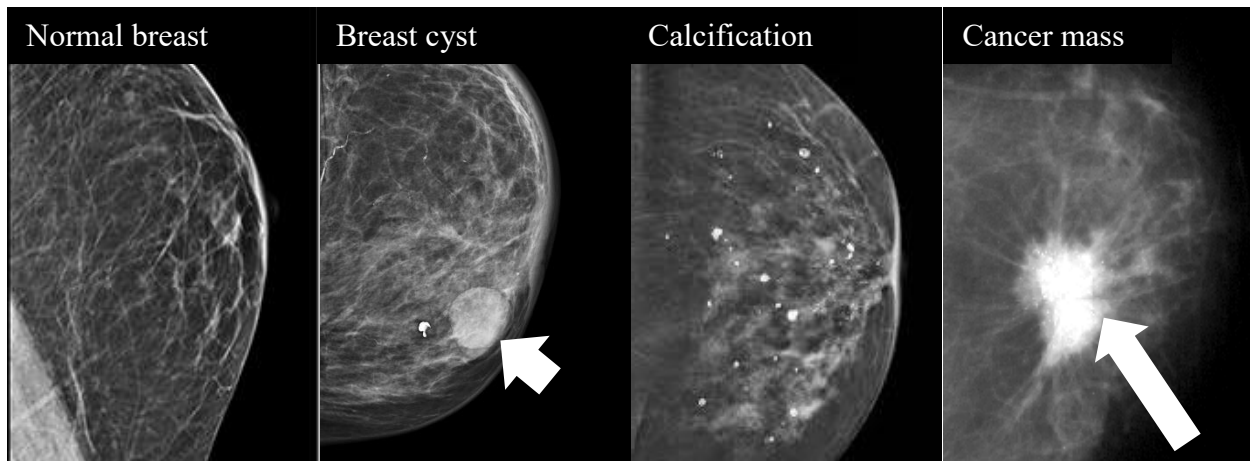
Figure 4. Example mammograms showing various breast conditions.

The first image (far left) shows a mammogram for healthy normal breast tissue. Breast cysts (second image from left) show up often as a light oval, with a secondary imaging technique often required to distinguish them from a cancerous mass. Calcifications (third image from left) either form on the macro- or microscale (this picture shows microcalcification) and are characterized by a cluster or single white dots. Breast cancer often shows up as a bright white dense mass in an irregular shape. Normal breast image reproduced from the Austin Diagnostic Clinic, 2019, retrieved from https://www.adclinic.com/confusion-breast-density/Cyst. Copyright 2019 by The Austin Diagnostic Clinic. Cyst image adapted from Radiopaedia, 2019, retrieved from open access https://radiopaedia.org/cases/ simple-breast-cyst-2. Copyright 2019 by Radiopaedia. Calicification image reproduced from Radiopaedia, 2019, retrieved from https://radiopaedia.org/cases/benign-breast-calcifications?lang=us. © 2019 by Radiopaedia. Breast cancer image adapted from http://www.klinikaikozpont.u-szeged.hu/radiology/radio/emlo/aemlo6a.htm, 2019.

Mammography uses low-dose x-rays to construct images of each breast. Specialized equipment compresses the breast between two plates, so the low-dose x-rays can pass through the fatty tissue. Cysts, microcalcifications, or potential cancerous tumors are distinguishable by a bright appearance compared to the surrounding tissue. **Figure 4** shows a comparison of these breast conditions when viewed from a screening mammogram. Screening mammography has an average clinical sensitivity of 87% and clinical specificity of 89% [14], which decreases to 76.5% and 83.8%, respectively, for women younger than 40 [15]. Clinical sensitivity refers to how well the test or equipment identifies disease when disease is present, with a high sensitivity correlating to the majority of disease-positive cases being detected. Clinical specificity measures

the ability of a test to correctly distinguish individuals who do not have the disease and would therefore result in a low specificity if many false positive readings occurred. The median size of tumor detected through a screening mammogram is 1-1.5 cm [16]. Screening mammography often detects early stage breast cancer before a mass becomes large enough to identify through physical examination [17]. However, this improvement is countered by false positives. The low positive predictive value (PPV 28.6%) yields a ~70% chance of incorrectly identifying disease in a patient free of cancer [14], which further decreases for younger women. Because false positives cause unnecessary emotional strain and are followed by time-consuming and costly tests that may not be covered by insurance, mammograms are not recommended for screening average-risk individuals until 40 years of age.

Dense breast tissue creates an additional limitation for mammography. For these patients, clinical sensitivity drops to 47.8-64.4%, because x-rays cannot travel through thick glandular tissue [18]. Such dense breast tissue also appears bright on a mammogram, making cancerous masses difficult to detect (**Figure 5**). This limitation led the ACR to recommend additional ultrasound imaging for patients with dense breast tissue [13]. Studies have found supplementary ultrasound detected more breast cancer cases than solo mammography for women with dense breast tissue [19-22]. However, results from these studies only show a slight improvement in detecting cancer over screening with mammography alone [19]. Further, imaging by both ultrasound and mammography increases false positive rates, potentially decreasing the PPV to 16% [20]. Due to this inherent disadvantage, the ACS and National Comprehensive Cancer Network (NCCN) do not recommend ultrasounds.

Figure 5. Gradient of mammograms taken from breasts with mostly fatty tissue to dense breast tissue. The light appearance of the dense breast tissue (far right) could hide potential cancerous masses from view, making mammography a less accurate method of screening for breast cancer in the dense breast patient population. Image reproduced from The Austin Diagnostic Clinic, 2019, retrieved from open access https://www.adclinic.com /confusion-breast-density/. © 2019 by The Austin Diagnostic Clinic.

For women at high familial risk for developing breast cancer, in particular due to any *BRCA1* or *BRCA2* gene mutations, mammography sensitivity decreases to 33-55%, potentially because many of these women are suggested to screen earlier than 50 years of age [23-26]. Therefore, the ACS and ACR both include adjunct magnetic resonance imaging (MRI) screening with annual mammography for high-risk individuals [12, 13]. MRI uses magnetic fields to manipulate hydrogen atoms in the water of tissues, often with the aid of contrast agents, and can differentiate fatty, glandular, and cancer tissues. With this high contrast, MRIs achieve sensitivities up to 100% [24, 27-31], consistently higher than mammography, ultrasound, or both modalities combined for high-risk patients [24, 32-35]. However, MRI screening is not recommended for average-risk patients due to high cost and lower accessibility to the equipment, and therefore is only suggested as supplemental to mammography for high-risk patients because

the lower specificity requires unnecessary biopsies or tests (as low as 80% in detecting benign growths) [23].

1.2.3 Diagnosis

Diagnostic imaging. If an abnormality is found during screening, or if symptoms arise, the NCCN recommends follow-up according to the ACR Breast Imaging Reporting and Data System (BI-RADS) category. The BI-RADS categories range from 1 to 5 with increased risk that the detected lesion is indeed malignant, and the NCCN recommends increased levels of intervention based on these categories (**Table 2**) [36].

Table 2. Breast Imaging Reporting and Data System (BI-RADS) categories.
Categories are listed with their associated imaging follow-up tests described in accordance with the NCCN guidelines. The radiologist assesses mammography images to provide a score, dictating what subsequent diagnostic imaging methods are prudent. Information adapted from "Breast Cancer Screening and Diagnosis, Version 3.2018, NCCN Clinical Practice Guidelines in Oncology", T. B. Bevers et al., 2018, 11:16 [36].

BI-RADS category	Number indication	Action required
1-2	1= negative finding 2 = benign	Resume routine screening
3	3 = probably benign	Diagnostic mammogram after 6 months, followed by imaging every 6–12 months for 1–2 subsequent years. If the lesion increases in size or changes in characteristics, perform biopsy
4-5	4 = suspicious of malignancy 5 = highly suggestive of malignancy	Perform tissue biopsy – pathology report must correlate with imaging findings. If they are discordant, repeat breast imaging with additional surgical excision recommended if findings still discordant
6	6 = proven malignancy	Malignancy previously proven by biopsy, patients undergoing treatment. Perform follow-up mammograms.

Firstly, initial screens may produce false positives if benign lesions are mistaken for tumors. For results indicating that a mass is probably benign, clinicians withhold intervention

until a second diagnostic mammogram 6 months later [36]. Unlike screening mammography that only captures two images from two viewpoints for each breast, diagnostic mammography incorporates additional views and can magnify the suspected area. Patients with physical symptoms present may receive a diagnostic mammography directly.

Similarly, ultrasound or MRI may be combined with diagnostic mammography to further exclude benign masses and clinically occult cancers [37], particularly if patients are symptomatic despite negative screening results [36]. For example, using both diagnostic mammography and ultrasound in symptomatic patients resulted in a clinical specificity of 97.7%, clinical sensitivity of 92%, and a 68% PPV [38]. Likewise, MRI may be helpful for patients exhibiting nipple discharge or skin discoloration whose initial diagnostic images point toward negative results or a benign mass (BI-RADS category 1-3) [39]. In such cases, MRI has been useful to identify less common breast cancers such as pagets disease of the nipple or inflammatory breast cancer [40, 41].

Staging of the Disease. The American Joint Committee on Cancer (AJCC) developed a standard reporting system for staging breast cancers called the TNM classification system[42]. The system combines results from several analyses, such as imaging and lymph node biopsies, to "score" the tumor size (T), lymph node status (N), and presence of metastases (M).

The T score measures the diameter of the primary tumor through screening and diagnostic images. A "T0" score is reserved for an unobservable tumor. Tumors smaller than 2 cm are scored as "T1", between 2-5 cm as "T2", and greater than 5 cm as "T3" (**Table 3**). The highest score "T4" indicates that the tumor has spread outside the breast to the chest wall and/or skin[42]. **Table 3** only provides an abridged version of the T scores used in staging.

Table 3. Summarized AJCC scores for tumor size.

The general prognosis worsens, and stage increases from T0 to T4. Information summarized from "Breast Cancer – Major Changes in the American Joint Committee on Cancer eighth edition cancer staging manual," A. E. Giuliano et al., 2017, 8th edition, p. 624, John Wiley and Sons. ©2017 by the American Cancer Society [42].

T score	Size/characteristics of tumor
T0	No tumor physically evident
T1	tumor is ≤ 2cm
T2	tumor is >2cm but ≤ 5cm
T3	tumor is > 5cm
T4	Tumor has spread to the chest wall and/or skin

Beyond the breast tumor itself, clinicians gauge the metastatic spread of the cancer through the lymph system. The first area for breast cancer to often spread to is the sentinel lymph nodes found closest to the breast, with the second site for metastases most commonly in the axillary lymph nodes under the arm. Via a tracer dye injected into the breast, sentinel lymph nodes first absorbing the tracer are removed for an initial screening by histological analysis, which if present, are further extracted during tumor resection [43]. The number of lymph nodes containing cancer cells, the abundance of cancer cells in the lymph nodes, and corresponding imaging results are compiled into a "N" score (**Table 4**) that gauges the potential for metastatic spread.

Table 4. Abridged scoring system for nodal status from the AJCC TNM staging system.
Prognosis worsens, and stage increases from a score of N0 to N3. Information summarized from "Breast Cancer –
Major Changes in the American Joint Committee on Cancer eighth edition cancer staging manual," A. E. Giuliano et
al., 2017, 8th edition, p. 624, John Wiley and Sons. ©2017 by the American Cancer Society [42].

N score	lymph node status
N0	
1. axillary and other nearby lymph nodes do not have cancer present OR 2. only show individual cancer cells (cells ≤ 0.2mm)	
N1	
N1mi	1. micro metastases between 0.2-2mm OR 2. > 200 cancer cells present
N1a	metastases in 1-3 axillary lymph nodes, with at least 1 cancer cell group > 2mm
N1b	metastases in internal mammary nodes
N1c	metastases in 1-3 axillary lymph nodes, with at least 1 cancer cell group > 2mm AND metastases in internal mammary nodes
N2	
N2a	metastases in 4-9 axillary lymph nodes, with at least 1 cancer cell group > 2mm
N2b	metastases in internal mammary nodes present on mammogram or other imaging, with no metastases found in axillary lymph nodes
N3	
N3a	1. ≥ 10 axillary lymph nodes show metastases, with at least 1 cancer cell group > 2mm OR 2. metastases in infraclavicular nodes
N3b	1. Metastases in 1-9 axillary lymph nodes with at least 1 cell group > 2mm AND metastases in internal mammary nodes seen on mammogram OR 2. Metastases in 4-9 axillary lymph nodes with at least 1 cancer cell group > 2mm AND metastases in internal mammary nodes seen from biopsy
N3c	metastases in nodes above the clavicle

Cancer spread through lymph nodes is considered local metastases. In advanced stages of
breast cancer, distant metastases can form. Clinicians traditionally examine metastases through
computed tomography (CT) of the chest, bones, abdomen, and pelvis. The NCCN recommends
additional imaging when symptoms and/or physical examination leads clinicians to suspect
metastases [44]. For example, bone scans rely on an injectable radioactive tracer to highlight
metastatic cancer cells disseminated into the bones, but the NCCN only advises such tests if the
patient experiences bone pain [44]. Similarly, a chest CT for lung metastasis is mainly
implemented when pulmonary symptoms are present, and abdominal CT/MRI imaging is only

performed in cases of abnormal physical examination results. Regardless of where distant metastases are found, patients are reported with a score of "M1" indicating metastatic breast cancer. However, imaging is not shown to provide any clear benefit for the early detection of metastases in asymptomatic patients and are only ordered at the discretion of the physician [45]. Thus, although CT imaging is required for staging metastases, a patient can be reported as "no metastasis present" or "M0" in the AJCC staging system without any imaging results [46].

The findings for tumor size, node status, and presence of metastasis are all combined in officially staging breast cancer according to the AJCC's TNM system [46]. The stages range from 0-4, with higher stages corresponding to worse prognosis. Stage 0 refers to any breast cancer diagnosed as non-invasive; stage I-III describes any locally invasive breast cancer; and any sign of metastasis (M1) results in a stage IV diagnosis. The AJCC changed their staging guidelines to also require assessment of the grade of the breast cancer and receptor status in 2017 [46], with these clinical procedures described below.

Grading Breast Cancer by Histology. For all malignant cases, tissue biopsies of the tumor are required. Biopsies are extracted prior to treatment or surgery, with some patients receiving an additional biopsy after surgery to assess response to neoadjuvant therapy or determine the need for adjuvant therapies. Pathologists perform histological analyses of the extracted tumor material. These results coupled with image findings (discussed above) help clinicians stage the cancer and predict prognosis for disease progression.

Pathologists "grade" the cancer by microscopic examination of cell morphology. This grade is based on the glandular formation, mitotic index, and nuclear pleomorphism observed in the tissue sample. Glandular formation refers to the ability of cancerous cells to form normal glands (tubules). Pathologists observe the number of cancer cells actively dividing (mitotic

index) and the shape and structure of cells, particularly gauging size of the cell nuclei and uniformity in cell size and shape (nuclear pleomorphism). Invasive breast cancers are graded on a scale from I to III, with a grade III breast cancer correlating with abnormally-shaped, fast-growing cells that cannot form organized glandular structures (**Figure 6**).

Grade 1	Grade 2	Grade 3
Glandular/Tubular Differentiation: >75% of tumor forms glands	**Glandular/Tubular Differentiation**: 10% to 75% of tumor forms glands	**Glandular/Tubular Differentiation**: <10% of tumor forms glands
Nuclear Pleomorphism: Uniform cells with small nuclei similar in size to normal breast epithelial cells	**Nuclear Pleomorphism**: Cells larger than normal with open vesicular nuclei and moderate variability in size and shape	**Nuclear Pleomorphism**: Cells with vesicular nuclei and marked variability in size and shape
Mitotic Count: <7 mitoses per 10 high power fields	**Mitotic Count**: 8-15 mitoses per 10 high power fields	**Mitotic Count**: >16 mitoses per 10 high power fields

Figure 6. Illustrations outlining the characteristics associated with the 3 grades of breast cancer.
Glands are formed by a high level of cellular organization. Nuclear pleomorphism compares the cell morphology and nucleus size to that found in normal breast epithelial cells, with higher differentiation correlating to a worse grade and prognosis. An increase in mitotic count refers to a high level of proliferation found in higher grade cases of breast cancer. Reproduced from open access Johns Hopkins Medicine Pathology, 2019, Retrieved from https://pathology.jhu.edu/breast/my -results/staging-grade/. © 2019 by Johns Hopkins University.

Molecular Profiling. Molecular analysis provides physicians with important information for deciding personalized treatment pathways for each breast cancer patient. The American Society of Clinical Oncology (ASCO) recommends testing of three markers for all invasive breast cancer

cases: estrogen receptor (ER), progesterone receptor (PR), and human epidermal growth factor receptor 2 (HER2) [47]. Tumor expression of ER or PR indicates promoted tumor growth in response to their associated hormones (estrogen or progesterone, respectively), whereas overexpression of the HER2 receptor causes uncontrolled cell growth. Another less-common molecular marker tested is Ki-67. The Ki-67 protein is expressed during the mitotic process within cells and a strong indicator of cancer proliferation. Pathological reports use immunohistochemical staining against these molecular markers to indicate whether a tumor is positive or negative based on the level of proteins present in the tissue sample.In the last two decades, researchers have used gene expression profiling to further classify breast cancers from the traditional molecular analysis, with the benefit of providing separate information about prognostic prediction or predictive response to therapy to help make treatment decisions. Perou *et al.* first profiled 65 breast cancer tissue specimens and found most tumors had high expression of either basal or luminal epithelial cell genes, or overexpression of the *HER2* gene [48]. Another group of tumors showed profiles similar to normal breast specimens in their high expression of basal and adipose genes but low expression of luminal genes (**Figure 7A**). Since this revolutionary study, further transcriptomic profiling [49] has resulted in defining four major molecular subtypes for breast cancer : luminal A, luminal B, HER2 enriched, and basal-like. Luminal A and B are largely differentiated based on the high expression of proliferation genes found in luminal B but not in luminal A.
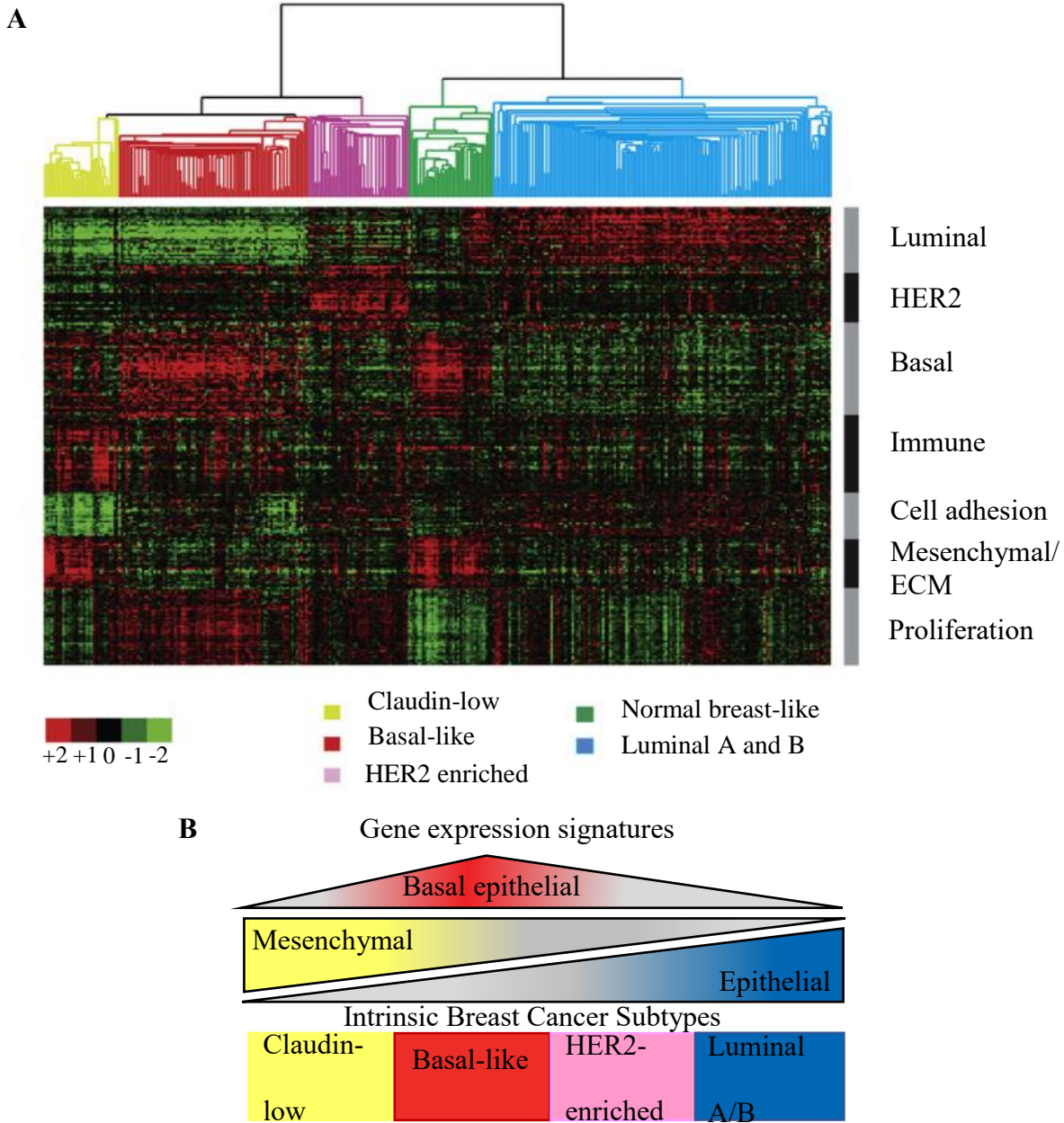
Figure 7. Molecular profiling of intrinsic breast cancer subtypes

(**A**) Prat et al. performed gene and array clustering according to the intrinsic gene list from Parker et al. [56] with the top dendrogram colors correlating to the intrinsic subtypes. Expression patterns to the right are based on gene clusters associated with breast cancer tumors or cell lines. The colored squares correlate to the transcript abundance, light red = high expression and light green = low expression. Reproduced from John Wiley and Sons: "Deconstructing the molecular portraits of breast cancer," by A. Prat and C. M Perou, 2011, Mol. Onc., 5:1, p.7. © 2011 with permission under CC BY-NC-ND: https://creativecommons.org/licenses/by-nc-nd/4.0/legalcode. Link to publication: https://doi.ord/10.1016/j.molonc.2010.11.003 [54]. (**B**) Five intrinsic subtypes and their gene expression similarity to breast cell gene signatures. Reprinted by permission from Springer Nature: Nature Reviews, *Nat. Med.* "Mammary development meets cancer genomics," b C.M Perou, 2011, 15:8, p. 843, John Wiley and Sons. © 2011.

Herschkowitz *et al.* discovered another molecular subtype claudin-low, recognized by the low expression of claudins and genes involved in cell adhesion with relatively high expression of genes associated with the epithelial to mesenchymal transition (EMT) (**Figure 7A**) [50]. The epithelial-to-mesenchymal transition occurs when epithelial cells lose expression of cell adhesion proteins such as epithelial cell adhesion molecule, EpCAM [51], or E-cadherin [52] and gain expression of mesenchymal genes such as vimentin, VIM [52], or fibroblast activation protein, FAPα [53]. This causes epithelial cells to detach and become mobile due to the development of mesenchymal-like morphology [54]. Each molecular subtype correlates with a certain level of mesenchymal or epithelial (luminal/basal cell) phenotypic expression with claudin-low showing the highest signature of mesenchymal characteristics while luminal subtypes fall on the opposite end, mostly expressing luminal epithelial cell characteristics (**Figure 7B**).

The discovery of intrinsic molecular subtypes complemented the traditional classification system with molecular analyses that advanced clinical methods for classifying breast cancer cases. Though certain types of receptor status appear more frequently in one intrinsic subtype over another (**Figure 8**) , no one combination of hormone or HER2 status definitively identifies a single subtype. Thus, traditional receptor testing remains as the standard method of molecular analysis used in clinics.
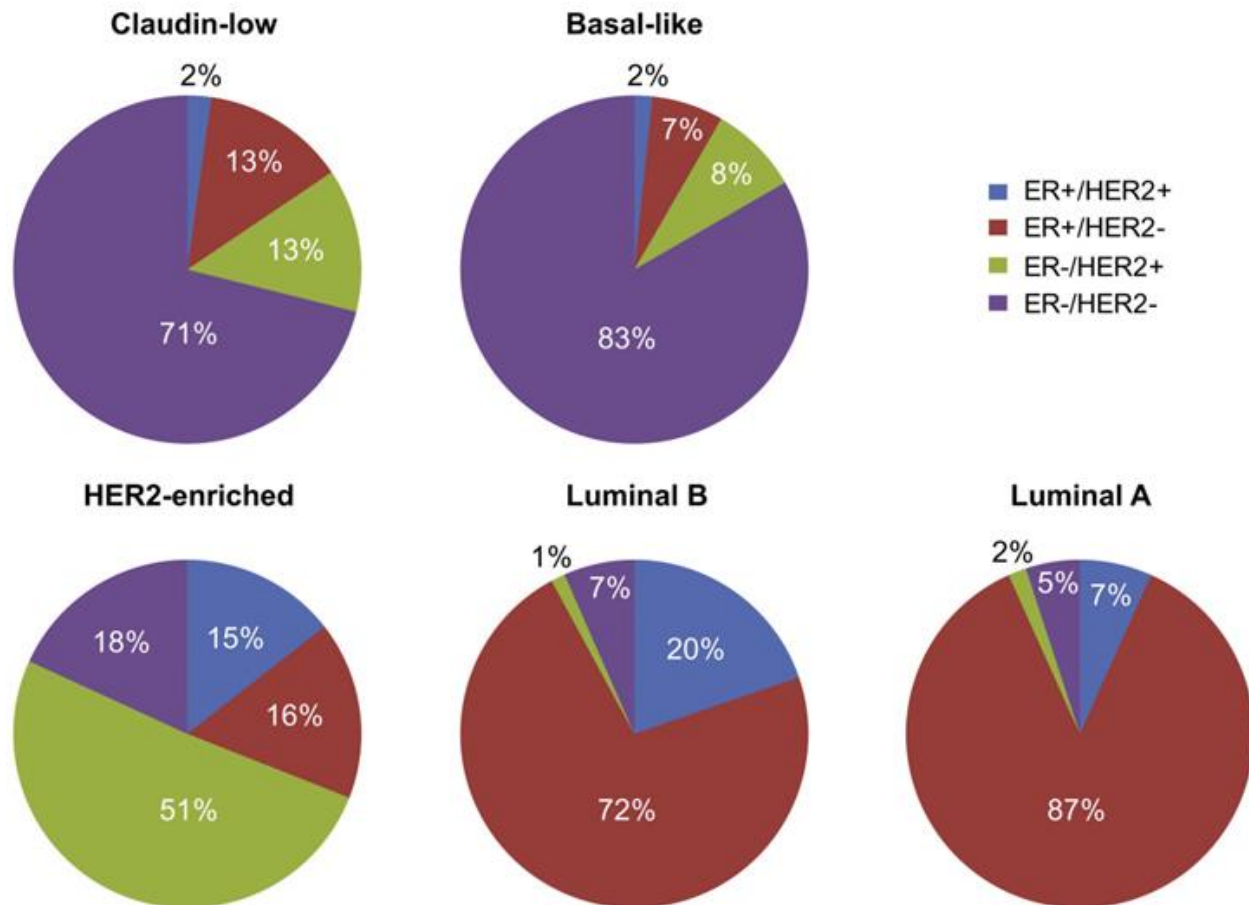
Figure 8. Relative prevalence of ER+/HER2+, ER-/HER2+, ER-/HER2- in the five intrinsic molecular subtypes. Most claudin-low and basal-like cases are triple negative or show low expression of all three common molecular markers. Luminal A and B often exhibit higher expression of the estrogen receptor, while HER2-enriched breast cancer shows high expression of HER2 in an average of 66% of cases. Reproduced from John Wiley and Sons: "Deconstructing the molecular portraits of breast cancer," by A. Prat and C. M Perou, 2011, Mol. Onc., 5:1, p.7. © 2011 with permission under CC BY-NC-ND: https://creativecommons.org/licenses/by-nc-nd/4.0/legalcode. Link to publication: https:/ /doi.ord/10.1016/j.molonc.2010.11.003 [54].

The subtypes have also been characterized for their correlation with various breast cancer grades. Claudin-low and basal-like breast cancer often result in a clinical grade of III, with roughly 70 and 80% showing triple negative receptor status [55]. HER2 enriched is also associated with a high clinical grade of III [56], while a majority of luminal A and luminal B are grade I-II or II-III, respectively [56]. Luminal B are higher grade than luminal A due to the overexpression of proliferation genes allowing cancer to grow more rapidly.Research has

demonstrated the ability of these subtypes to predict disease prognosis or progression with high

certainty. To help investigate the prognosis and progression using a simplified gene panel, Parker

et al. [57] discovered 50 genes to best differentiate the intrinsic subtypes [57]. Total RNA

(TRNA) was extracted from 189 formalin-fixed paraffin-embedded (FFPE) or fresh frozen

samples for subsequent reverse transcription (RT) and quantitative PCR (qPCR) as well as

microarray profiling. The selected genes and their respective expressions in the four main

intrinsic subtypes and in normal control samples taken from reduction mammoplasty are shown

in **Figure 9**. Prat *et al.* assessed a large sample set that included microarray samples tested by

Parker *et al.* [57] for disease-free and overall survival rates based on each intrinsic subtype [58].

A separate predictor was used for the identification of claudin-low samples. HER2 enriched,

basal, luminal B, and claudin-low all follow a similarly short disease-free timeframe and lower

likelihood of long-term survival when compared to luminal A (**Figure 10**). Luminal A breast

cancers showed a much higher chance for exceeding 5 years with no disease recurrence after

treatment.

The realization that molecular profiling breast cancers through gene expression assays

could highly predict the risk of recurrence or relapse led to the Food and Drug Administration

(FDA) approving several assays for use in the clinic, with one analyzing the 50 genes discovered

by Parker *et al.* [57] (test called Prosigna®). The Prosigna® Breast Cancer Prognostic Gene

Signature Assay examines these genes (listed in **Figure** 9) through direct expression

measurements from isolated RNA using nCounter® technology (NanoString). A reporter probe

to supply the fluorescent signal and capture probe to immobilize the product are hybridized

directly to the specific RNA of interest. The expression data is collected through a scanning

fluorescence microscope, and a software program then creates a risk of relapse score that can

predict the distant recurrence-free survival at 10 years for post-menopausal women diagnosed with breast cancer who are HR+, node-negative (stage I or II) or node-positive (stage II). These risk scores stratify patients based on the benefit of chemotherapy post-surgery in addition to hormone therapy [59].
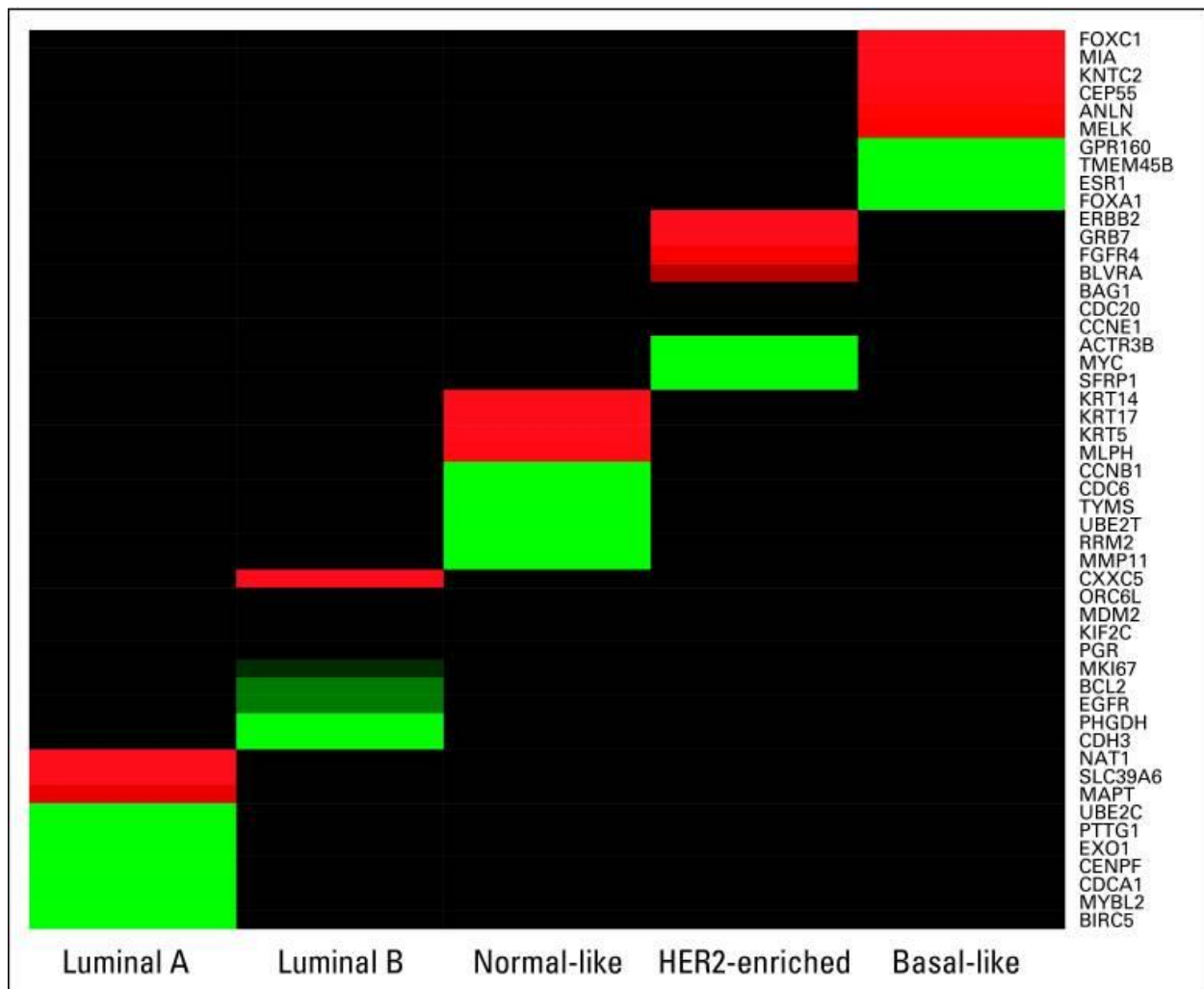
Figure 9. Prevalent expression of PAM50 genes to four intrinsic subtypes and normal breast tissue
Clustering of the 50 genes included in the PAM50 predictor and their associated genes of interest based on the intrinsic subtypes. Green correlates to highly expressed genes in the intrinsic subtype; red-colored genes are expressed at low levels; and black is either normal expression or blocked out. Reprinted with permission. © 2009 by American Society of Clinical Oncology. All rights reserved. Parker, J et al: "Supervised risk predictor of breast cancer based on intrinsic subtypes," *J Clin Oncol*, Vol. 27(8), supplemental figure A2. [56].
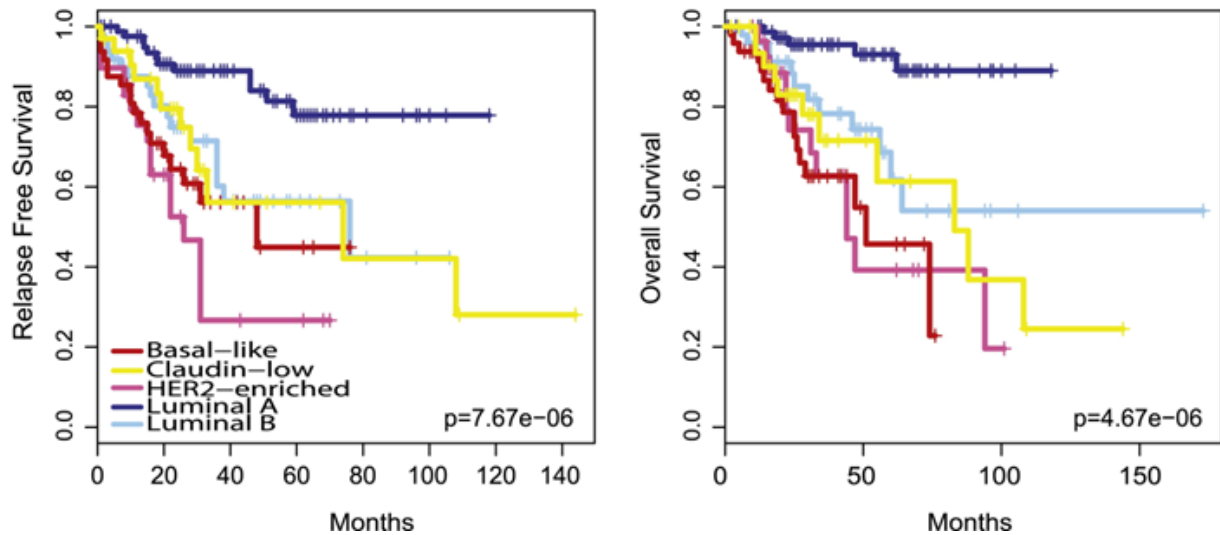
Figure 10. Figure 10. Kaplan-Meier graph showing overall and relapse free survival for

The UNC337 dataset of breast cancer tumor gene expressions were analyzed by Prat *et al.* [57]. This data was later modified in a publication by Prat and Perou [54]. The sample cohort included a heterogeneous spread of treatment methods that were determined based on molecular marker status. The graphs mainly show the markedly higher relapse-free and overall survival associated with the Luminal A subtype. . Reprinted from John Wiley and Sons: "Deconstructing the molecular portraits of breast cancer," by A. Prat and C. M Perou, 2011, *Mol. Oncol.*, 5:1, p.7. © 2011 with permission under CC BY-NC-ND: https://creativecommons.org/licenses/by-nc-nd/4.0/legalcode. Link to publication: https:/ /doi.ord/10.1016/j.molonc.2010.11.003 [54].

In contrast to the PAM50 assay, the Oncotype Dx examines only 21 genes through traditional reverse transcription-polymerase chain reaction (RT-PCR) that are important to cell proliferation or found in ER and HER2 signaling processes [60]. The expression patterns of these genes correlate with a quantitative score to distinguish the probability of recurrence. The recurrence score distinguishes hormone receptor positive (HR+) cases based on predicted hormone therapy outcome and sensitivity to chemotherapy [61], providing physicians with knowledge pertinent to choosing the right treatment pathway.

Though molecular profiling is a promising new classification technique for breast cancer management, it is currently still not fully recommended in clinical guidelines and is considered secondary to the traditional pathology testing of receptor status for determining treatment and prognosis. Thus, these assays are only ordered if enough tissue sample remains after the initial

pathological review, and the AJCC does not require gene profiling as a test for assigning stage [46]. However, the AJCC does suggest use of the Oncotype Dx assay in certain cases because large-scale prospective clinical trial data supports its use in determining whether adjuvant chemotherapy is beneficial to patients with node-negative, ER+ breast cancer [62].

1.2.4 Treatment

After receiving the pathological report, a physician will use the information to create a treatment plan for each patient. The one common treatment procedure for all breast cancer patients is surgical excision to remove the cancer tissue. However, the extent of breast removal is guided by the prognosis of the disease, the predicted response to therapies, and the stage at which the breast cancer is diagnosed.

A surgeon may either perform a mastectomy or lumpectomy. Mastectomy requires removal of the entire breast and is often the optimal option for women with small breasts and large tumors, many malignant calcifications, locally advanced breast cancer, or patients with tumors fixed to the chest wall [63]. However, for patients that desire breast-conserving surgery, the therapies discussed below can also be administered prior to surgery (neoadjuvant therapy) to shrink the tumor before resection [63]. For patients with non-invasive or early stage invasive cancers without wide spread of the tumor, a lumpectomy is suggested that only resects cancerous tissue and leaves most of the breast intact. While this surgery is less invasive and cosmetically maintains the breast, radiation after surgery (adjuvant therapy) targets remaining cancer cells and yields comparable overall survival rates to mastectomies [64].

For all cases, pathologists perform margin assessment of the excised mass to detect any remaining signs of cancer. The "margin" is a ring of non-cancerous tissue surrounding the cancerous mass that the surgeon removes. If cancer cells are present within this margin, re-

excision is required to remove remaining cancer from the breast. Lymph nodes removed during surgery are similarly tested to detect whether the cancer has further metastasized into the lymph system and if there is a need for additional surgical resection.

Adjuvant therapy is recommended for patients with a strong likelihood of cancer recurrence [63]. However, a physician may suggest adjuvant therapy to any patient after surgery to kill any residual cancer cells, as they cannot be visualized through current diagnostic tools. Chemotherapy serves as the only systemic treatment option beneficial to patients with triple negative (ER-/PR-/HER2-) breast cancer [63]. For patients positive for hormone receptors, endocrine therapies can be implemented to inhibit cancer growth by targeting estrogen and progesterone receptors. The most common drugs used for ER-based endocrine therapy are tamoxifen or aromatase inhibitors. Tamoxifen blocks estrogen from binding to ER receptors, while aromatase inhibitors block the enzymes responsible for producing estrogen [65]. Both older and younger women either post or pre-menopause have benefited from tamoxifen, but only post-menopausal women over the age of 50 saw equivalent or greater benefit when compared to chemotherapy [66]. For patients with HER2 enriched cancers, the anti-HER2-specific monoclonal antibody (mAb) trastuzumab binds to HER2, which causes the receptor to internalize and blocks signal transduction. The addition of trastuzumab to chemotherapy regimens for HER2+ untreated metastatic breast cancer was found to increase overall survival and create a longer median response to therapy when compared to chemotherapy alone [67].

The use of adjuvant therapy as a precautionary treatment to kill residual cancer cells in any patient highlights the fact that no widely available diagnostic tool is sensitive enough to detect minimal residual disease (MRD) at very low cancer burden, which can cause relapse if not treated. Thus, while the initial clinical workflow for diagnosis and the identification of therapy

options is robust, adjuvant therapy is often recommended because of the technological limits currently found in monitoring of disease.

1.2.5 Monitoring

Monitoring is important to gauge both treatment response and detect cancer recurrence. For all but metastatic cases, monitoring is considered "surveillance" and is enacted after treatment. The ASCO [68] and NCCN [44] recommends routine physical examinations and mammography after treatment, but only 40% of recurrence cases are identified by mammography before physical symptoms arise [69]. More sensitive testing, such as MRI, is not used for routine monitoring and is instead only supplemental for inconclusive mammograms [13]. Further, patients who undergo mastectomy having their entire breast removed currently have no guidelines to address the replacement of mammograms as the surveillance method. It is left to each individual health professional or their institution in how to monitor post-mastectomy patients [70].

Once breast cancer has metastasized to distal sites, the disease is considered incurable. Tests throughout treatment seek to assess the overall health of the patient (toxicity levels) and response to treatment. For example, if the disease continues to progress through treatment, physicians may switch therapies. The NCCN recommends a panel of tests for patient health that are continuously monitored throughout treatment – such as liver function tests and complete blood counts – and CT imaging for monitoring progression of the metastases in the pelvis, chest, abdomen, or bone scans for monitoring metastasis in bones [71]. However, bone scans can result in false positives due to the metabolic activity created by several disease processes such as trauma or inflammation that is visualized through the use of radio tracers [71]. CT monitors treatment response based on the size of the tumor, with tracers sometimes applied to increase contrast in the images. Both tests require 2-3 hours for the radio tracer to reach the metastatic

sites from the intravenous injection, expose the patient to additional radiation, and can cause side-effects from the contrast agents that range from nausea to cardiopulmonary arrest [72].

Combining positron emission tomography (PET) with CT can visualize both anatomic changes and abnormal metabolic activity because fluorodeoxyglucose (FDG) is taken up by the rapidly growing cancer cells (FDG PET/CT). PET/CT is an optional method advised by the NCCN [70], but there are no reproducible or validated standards of assessment for the examination of PET/CT images for detecting disease progression. However, standardization could make PET/CT a powerful tool as multiple studies found PET/CT to outperform conventional imaging technologies in detecting metastasis [73, 74].

Though imaging remains the mainstay for assessing treatment response in metastatic breast cancer, it is still limited by sampling frequency and tumor size detection limit (7 mm for PET [75] and 3 mm for CT [76]). Furthermore, the interpretation of results is heavily dependent on the experience of the radiologist analyzing the images. These limitations among others motivated researchers to look for other tests to monitor disease such as liquid biopsies (discussed below).

1.3 Liquid biopsy biomarkers for cancer management

Liquid biopsies extract biomarkers from bodily fluids such as blood, urine, saliva, or cerebrospinal fluid for detecting, diagnosing, or monitoring disease. Liquid biopsies are minimally invasive and more accurately convey the heterogeneous nature of the cancer [77] as well as allowing for more frequent sampling over a longer period of time when compared to traditional tissue biopsy or imaging modalities. Therefore, clinical oncology research has focused on investigating the ability of liquid biopsies to provide equivalent or further information to clinicians than is currently received from solid tissue analysis or imaging. The impact of a liquid

biopsy depends highly upon the biomarker chosen for assessment. The biomarker needs to provide actionable information by indicating disease recurrence, progression, or survival to help guide treatment decisions [78].

1.3.1 Proteins

In monitoring treatment response for metastatic breast cancer (MBC) patients, protein markers that are indicative of tumor progression can also be analyzed through a serum sample taken from a blood draw. The tests are minimally invasive to the patient [79] and may show signs of relapse prior to physical symptoms appearing on images. While ASCO does not approve such testing as stand-alone care for monitoring, they can facilitate certain treatment decisions, such as the benefit of continuing therapy, when used in conjunction with imaging [62]. One protein biomarker is a glycoprotein overexpressed on cancer cells, mucin 1 (MUC-1). Another protein marker is normally associated with fetal development that decreases in healthy adults but is elevated to 40-50% in metastatic breast cancer patients and is called carcinoembryonic antigen (CEA).

Two common immunoassays use antibodies (Abs) that target different epitopes of the same solubilized MUC-1 protein, cancer antigen 15-3 (CA 15-3) and cancer antigen 27.29 (CA 27.29). Though both markers have generated concordant results [80], CA 15-3 is backed by more clinical data validating its role in monitoring metastatic breast cancer [79]. CA 15-3 is associated with a 60.3% clinical sensitivity and 71.1% clinical specificity in determining therapy response, with the combined use of CEA increasing the specificity to 95.5% but decreasing the sensitivity to 32% [81]. Because CEA is only elevated in 40-50% of metastatic breast cancer patients, current clinical guidelines only suggest CEA be used in cases where CA 15-3 is inconclusive due to normal MUC-1 antigen levels [62]. The ASCO only suggests any tumor markers for

monitoring metastatic breast cancer when disease cannot be measured by imaging. For example, neither PET [75] or CT imaging can detect a tumor < 3 mm [76]. In these cases, an increase in these tumor markers coincides with treatment failure.

1.3.2 Circulating tumor cells (CTCs)

CTCs are shed from the primary tumor or areas of micro/macro-metastases and released into blood circulation. This motility transports CTCs to distant organs where they promote metastasis, with high levels of CTCs often detected in metastatic breast cancer [82, 83]. Anywhere from 1 to 3000 CTCs may be detected in 1 mL of blood [84].

Researchers have heavily assessed CTCs for clinical use as there are over 17,000 publications [85] and 10 years of large-scale clinical studies investigating their merit in cancer management [86]. This extensive research helped lead to the FDA approval of the CellSearch System™ as a prognostic tool for metastatic breast cancer. The system and the associated assay use EpCAM Abs to isolate CTCs from whole blood, then stains the cells for both positive markers using an epithelial-associated gene (CK+) and a nuclear stain (DAPI+) as well as a negative marker (CD45-) to differentiate the CTCs from white blood cells.

Increased CTC levels indicate poorer prognosis and lower response to treatment for metastatic breast cancer patients [87-90]. Smaller studies also investigated the use of CTCs in non-metastatic cases for predicting likelihood of relapse [90-94]. However, clinical guidelines do not suggest isolating CTCs [62] in clinical practice due to the lack of actionable information provided from quantification alone [95]. For example, a phase III clinical trial found enumeration of CTCs by the CellSearch System™ to provide no benefit for high-risk patients when changing therapy based on the CTC results [96].

Analyzing CTC nucleic acid content in addition to enumeration may prove more impactful in the clinical setting. The CellSearch™ profile kit allows for isolation of CTCs much as the standard CellSearch™ system assay, but includes lysis of the cells for molecular analysis [95]. However, CTC tests aimed at extracting genetic material and analyzing that material are still not approved by the FDA. Furthermore, because the CellSearch™ system only targets epithelial phenotypic cells, the assay lacks inclusion of CTCs undergoing or having undergone EMT [97] where epithelial cells lose expression of epithelial associated genes related to cell-cell adhesion such as EpCAM [51] and gain expression of genes facilitating cell motility and degradation of the extracellular matrix such as FAPα [53]. Other CTC isolation strategies have proven to mitigate this issue by including mesenchymal phenotypic markers, resulting in a sensitivity of 100% with 90% of CTCs showing no co-expression of these markers [98].

1.3.3 Circulating tumor DNA (ctDNA)

All cells release DNA into the blood stream through apoptosis or necrosis [85]. Initial discovery of cell-free DNA (cfDNA) indicated the presence of cancer due to higher concentrations of cfDNA in cancer patient blood compared to healthy individuals and a subsequent decrease after treatment [99]. However, other health conditions also create increased levels of cfDNA such as stroke, trauma, sepsis, or autoimmune disease [100]. Rather, the quantification of epigenetic or genetic changes such as somatic mutations, translocations, and amplifications found in ctDNA [101] provides more disease-specific information beneficial to breast cancer management.

No liquid biopsy assay isolating cfDNA is currently approved by the FDA for use in breast cancer clinical care, though studies highlight mutational analysis of ctDNA to indicate therapeutic resistance. Oncogenic mutations of the ESR1 ligand have been detected in ctDNA of metastatic breast cancer patients diagnosed as hormone receptor (HR)+, correlating to hormone

therapy resistance [102-106]. The identification of resistive mutations through serial tracking of ctDNA could provide critical information in altering treatment [107-109]. Monitoring ctDNA levels may also provide actionable information before physically identifiable presence of the disease, having detected relapse 8-11 months before symptoms arose [110, 111]. The detection of heightened ctDNA levels also produced higher sensitivity for predicting treatment response than the CellSearch™ assay or traditional tumor markers such as CA 15-3 [112]. A higher abundance of mutations was also found in isolated cfDNA compared to CTCs [113], thereby providing larger mutant input masses for downstream PCR analysis. However, neither the transcriptome nor the proteome can be analyzed through ctDNA.

1.3.4 Extracellular vesicles (EVs)

Similar to cfDNA, most cells shed EVs into circulation [114]. Like CTCs, EVs have been found to play a role in the disease process by stimulating tumor growth, suppressing immune response, inducing angiogenesis, and contributing to the metastatic process [115-117]. CTCs and cfDNA have been heavily investigated in the literature as biomarkers for breast cancer, with attention shifted toward EVs in the last few years due to their recent discovery as a stable carrier of nucleic acids and proteins originating from cancer cells.

Cancer patients have consistently produced higher concentrations of EVs [118] when compared to healthy individuals. However, EV enumeration alone lacks disease specificity because other conditions such as diabetes or cardiovascular diseases also increase their concentration in the blood [119, 120]. Therefore, EVs are isolated for molecular analysis of proteins, nucleic acids, or lipids that can provide more concise information on the nature of a specific disease [121, 122]. Markers of clinical significance must first be discovered in EVs as a

target for liquid biopsy assays before fully understanding their role as a biomarker for a specific cancer-related disease.

EV-encapsulated micro RNAs (miRNAs) can differentiate cancer types and promote angiogenesis and metastasis [123]. Multiple miRNAs have proven to exist at higher levels in breast cancer patients compared to healthy individuals [124], suggesting their potential for detecting disease and distinguishing molecular subtypes [125]. The expression of EV proteins, such as fibronectin and developmental endothelial locus 1 (Del-1), may provide a venue for detection of early-stage breast cancer and monitor minimal residual disease post-surgery [126, 127].

EV membrane proteins can be targeted to enrich cancer-derived EVs, or as a disease marker for breast cancer detection or molecular subtype identification. Several studies have found that the isolation of HER2 expressing EVs through anti-HER2 Abs that can be used to differentiate HER2+ breast cancer patients from healthy and HER2- controls [128, 129]. The results aligned well with the traditional molecular analysis of HER2 protein from a tissue sample.

EV messenger RNA (mRNA) has also been investigated as potential disease biomarkers for cancers [115, 130-132] owing to the discovery that EVs transfer host-cell mRNAs to recipient cells for protein translation [133]. Evidence of EV mRNA as a disease biomarker for breast cancer is lacking, with only one study investigating the transcriptome from metastatic breast cancer patients in comparison to CTC mRNA expression for monitoring therapy [134]. Investigating EV mRNAs for their potential use as disease biomarkers is important in breast cancer because gene expression profiling is currently performed on solid tissue from biopsies to procure further information into disease prognosis and potential therapies than is already

received from traditional pathology (further discussed in the molecular analysis section).

Therefore, a need exists to investigate mRNA expression profiles from breast cancer cell derived

EVs to determine if EV mRNA could serve as an alternative source of material extracted through

the less invasive liquid biopsy for molecular subtyping of the disease.

Biogenesis and structure.EVs protect and transport proteins, lipids, and nucleic acids to

facilitate cell-cell communication, influencing functions of the recipient cell [135]. They are

spherical and surrounded by a lipid bilayer membrane [136]. EVs are separated into three

categories depending on their size and mechanism of release (biogenesis): exosomes,

microvesicles, and apoptotic bodies (**Figure 11**)**.**
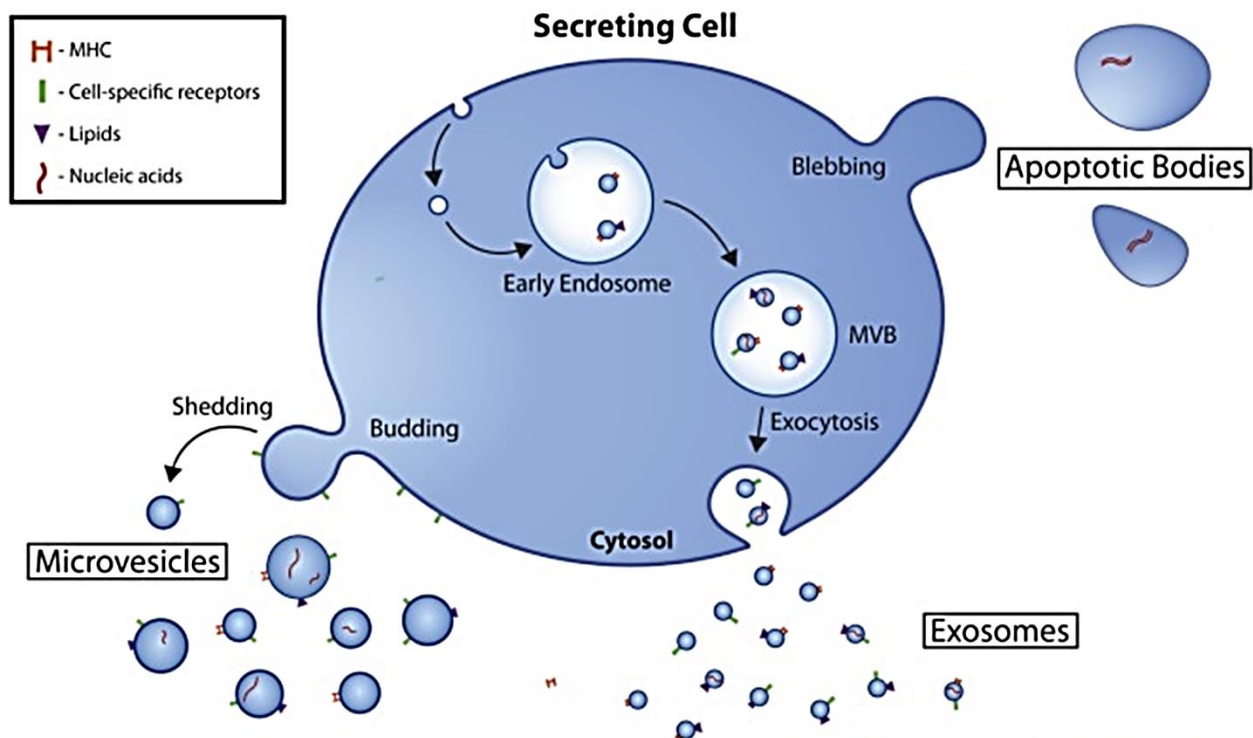
Figure 11. The biogenesis of EV subpopulations

Apoptotic bodies range in size from 50 nm – 2 μm, microvesicles from 50 nm – 1 μm, and exosomes from 30 – 150
nm. Adapted from *Front. Cardiovasc. Med*.: "Extracellular vesicles as protagonists of diabetic cardiovascular
pathology," by D. Gustafson, S. Veitch, and J. E. Fish, 2017, 4:71, p. 3. © 2017 Gustafson, Veitch and Fish. Adapted
with permission under CC-BY: https://creativecommons.org/licenses/by/4.0/legalcode. Link to Publication:
https://www.frontiersin.org/articles/10.3389/fcvm.2017.00071/full [18].

Exosomes form through the collection of intraluminal vesicles (ILVs) inside

multivesicular bodies (MVBs) and subsequent secretion by inward budding of the endosomal

membrane [137]. They are the smallest EVs, ranging anywhere from 30 to 150 nm in diameter

[118]. Microvesicles are generated through outward budding of the membrane and range in

diameter from 50 to 1000 nm [136]. Finally, apoptotic bodies can form the largest size

subpopulation, ranging between 50 and 2000 nm. They are only secreted from cells undergoing

apoptosis, where they are released into the surrounding environment [135].

Composition and cargo. Different EV subtypes are also similar in their composition, but do

include distinct cargo dependent upon the physiological and pathological state of the cell of

origin as well as the stimuli and mechanisms initiating biogenesis [136]. Little is known about

the composition of apoptotic bodies, with most research focusing on exosomes and

microvesicles. However, the presence of organelles may distinguish apoptotic bodies from other

EV subclasses [138]. Further, proteins involved in the macrophage-mediated phagocytosis of

apoptotic bodies such as annexin V, thrombospondin, and C3b serve as specific markers [139]

found in the outer membrane. Finally, apoptotic bodies can transfer DNAs, proteins, and lipids to

recipient cells [140-142].

Exosomes and microvesicles share some similarity in terms of membrane and

intercellular protein composition due to the biogenesis of these vesicles. Both EV types contain

heat shock proteins (HSP70, HSP90) for protection from stress and regulation of protein folding,

complex assembly, and subcellular sorting. Proteins for biogenesis (e.g. ALIX, TSG101) are

found in both exosomes and microvesicles, but some proteins are still distinct to each EV

subtype. Proteins for facilitating signal transduction (e.g. protein kinases, β-catenin) are

important for transferring information within an exosome or microvesicle [136] as well as

through the outer membrane to recipient cells. Because the microvesicles originate in the cytoplasm, cytoskeletal components (e.g. actin, tubulin) and cytoplasmic material (Tau, TDP43) are packaged into these EVs exclusively [136].

Cell adhesion and intracellular trafficking facilitate the transfer of cargo to recipient cells and reside in the membrane of exosomes and microvesicles. In fact, many studies have used annexins as a method of labeling and thereby detecting EVs because they are common membrane proteins on all EV populations [143]. Tetraspanins facilitate the organization of multi-molecular membrane complexes to aid in signal transduction [144]. Proteins distinct to the cell of origin or cell-type-specific proteins are also found within the membrane. Lipids contained in the membranes include phosphatidylserine and sphingolipids, with distinct lipids such as cholesterol and ceramides or phosphatidylethanolamine residing on exosomes or microvesicles, respectively. **Figure 12** illustrates the molecular composition of both subtypes providing examples of molecules of various functions.

Exosomes and microvesicles protect RNAs from RNase digestion occurring in the blood [101]. Most RNAs found in EVs measure around 200-500 nucleotides in length [136]. Derived from the cell of origin, EV-resident RNAs can be transferred to recipient cells to alter their pathology or physiology. Valadi *et al.* initially found miRNAs and poly-adenylated mRNAs that are capable of protein translation to exist in EVs [133]. More recently, RNAs including transfer RNA (tRNA), piwi-interacting RNA (piRNA), long non-coding RNA (lncRNA), short non-coding RNA (snRNA), and small nuclear RNA (snoRNA) have been detected in EVs through sequencing [145, 146].

Exosome composition (top)

Membrane organisers
Tetraspanins: CD9, CD81, CD63, TSPAN6, TSPAN8, CD151, CD37, CD53, Flotilin 1 and 2

Lipids
Phosphatidylserine, cholesterol, ceramide and other sphingolipids, LBPA

Cell adhesion
E.g. integrin, lactadherin, ICAM

Intracellular trafficking
E.g. RAB GTPases, annexins

Cell-type-specific proteins
E.g. MHC-I, MHC-II, APP, PMEL, TCR, FasL, CXCR4, HSPG, CD86, PrP, TFR, WNT

Exosome limiting membrane

A

Exosome lumen

Enzymes
Peroxidases, pyruvate kinase, enolase, GAPDH

Signal transduction
Protein kinases, β-catenin, 14-3-3, G proteins

Biogenesis factors
ALIX, TSG101, syntenin, ubiquitin, clathrin, VPS32, VPS4

Chaperones
HSP70, HSP90

Nucleic acids
microRNA and other non-coding RNAs, mRNA, DNA (and histones)

Microvesicle composition (bottom)

Membrane organisers
Tetraspanins: CD9, CD81, CD82

Lipids
Phosphatidylserine, phosphatidylethanolamine, sphingolipids

ECM adhesion
E.g. integrin, PECAM1, fibronectin

Intracellular trafficking
E.g. RAB GTPases, annexins

Cell-type-specific proteins
E.g. MHC class I, LFA1, CD14

Microvesicle limiting membrane

Microvesicle lumen

Cytoplasmic material
Tau, TDP43, GAPDH

Signalling molecules
For example, ARF6, RAB11, ROCK

Biogenesis factors
ALIX, TSG101, ERK, PLD, VPS4

Chaperones
HSP70, HSP90

Cytoskeletal molecules
Actin, tubulin

Nucleic acids
microRNA and other non-coding RNAs, mRNA, DNA (and histones)

Figure 12. General composition of exosomes and microvesicles.

Exosomes composition = top, microvesicle composition = bottom. Cargo consists of proteins, lipids, and nucleic acids. ALIX – ALG-2 interacting protein X; APP – amyloid precursor protein; ARF6 – ADP-ribosylation factor 6; ARMMs – arrestin-domain-containing protein 1-mediated microvesicles; CXCR4 – CXC-chemokine receptor 4; GAPDH – glyceraldehyde-3-phosphate dehydrogenase; HSP70 – heat shock 70 kDa protein; HSPG – heparan sulfate proteoglycan; ICAM – intercellular adhesion molecule; LBPA – lyso-bis-phosphatidyl acid; LFA1 – lymphocyte function-associated antigen 1; MHC – major histocompatibility complex; PECAM1 – platelet endothelial cell adhesion molecule; PLD – phospholipase D; PrP – prion protein; ROCK – RHO-associated protein kinase; TCR – T cell receptor; TDP43 – TAR DNA-binding protein 43; TFR – transferrin receptor; TSG101 – tumor susceptibility gene 101 protein; TSPAN – tetraspanin; VPS – vacuolar protein sorting-associated protein. Reprinted by permission from Springer Nature: Nature Reviews, *Molecular cell biology,* "Shedding light on the cell biology of extracellular vesicles," by G. van Niel, G. D'Angelo, and G. Raposo, 2018, 4:19, p. 214. © 2018 [135].

Most studies find little or no amounts of full-length 18S and/or 28S RNA in EVs [133, 146, 147], contrasting the typical abundance observed in cellular RNA. However, fragmented ribosomal RNA (rRNA) has been observed in multiple studies performing RNA sequencing of EV cargo with the rRNA accounting for at least 90% of total RNA (TRNA) found in EVs [122, 148]. Wei *et al.* conducted RNA sequencing on both microvesicles and exosomes to quantify the levels of each RNA species from glioma stem cell lines [148]. Within the remaining 10% of RNA that was found to be non-rRNA fragments, only 8-25% was considered long RNA (denoted as >100 nt) which was further broken into coding RNA or mRNA (accounting for ≤10% of long RNA) and non-coding RNA [148]. It is important to note that mRNA accounted for only ~ 0.25% of TRNA and a higher abundance of mRNA was found in microvesicles compared to exosomes. The other 75-92% of non-rRNA is small RNA (denoted as 15-25 nt) including miRNA which only accounted for about 2% and 6% of small RNA found in exosomes and microvesicles, respectively [148].

Overall, the mechanism with which nucleic acids are packaged into EVs is still unknown, creating a challenge in characterizing EV RNA [136]. Furthermore, the EV source, data collection modality, and isolation procedure contribute to the final resultant RNA quantification and characterization. Therefore, it is important to develop robust EV isolation methods to facilitate the discovery of packaging mechanisms and standardize knowledge about the cargo of EVs.

Chapter 2. Development of EV-MAP for breast cancer management

2.1 Introduction

This study aimed at investigating a less invasive method of isolating mRNA from breast cancer patients through a liquid biopsy biomarker, as mRNA is used for the intrinsic subtyping of breast cancer cases to provide further information into disease prognosis and potential treatment pathways than is received from traditional pathology. EVs are ideal for this purpose as they are stable carriers of mRNA within the blood. Once deciding upon a biomarker, it is next important to determine how these EVs will be isolated. As previously stated in the EV composition section of Chapter 1, the isolation method may affect the downstream analysis of EV internal cargo. With many isolation methods currently available, it is important to understand the advantages and limitations of each in order to choose the technique most beneficial for the specific downstream application of EVs, such as gene expression analysis of disease-associated EVs in the case of this study.

2.1.1 EV isolation

Benchtop methods. The traditional and most common technique for EV isolation is differential ultracentrifugation. This procedure separates EVs from cells or proteins based on size and density. Culture media or whole blood is centrifuged at 300g for 10 min to remove cells followed by 2,000g for 10 min to remove most apoptotic bodies, dead cells, and cell debris. A step at 10,000-14,000g for 30 min pellets most larger microvesicles [149], which may be resuspended for separate analysis from exosomes still remaining in the supernatant [150, 151]. Several subsequent steps of ultracentrifugation at 100,000-110,000g aim to purify the exosomes of any contaminating proteins.

Sucrose gradient centrifugation can further purify exosome fractions by eliminating sedimented proteins [149]. EVs remain in the gradient while contaminants sink to the bottom. Though differential ultracentrifugation is still the EV isolation gold standard, it fails to enrich certain subpopulations of EVs because it only isolates particles <150 nm [152]. Further, the laborious process may take 5-12 hours, requires expensive equipment often difficult to access, and results in a recovery of up to 60% even from a non-complex sample such as culture media [153].

Precipitation techniques decrease processing time and cost, with many commercial kits available using polyethylene glycol (PEG). These kits isolate EVs within 30 min after use of a centrifugation step at 10,000g [118]. PEG is an agglutinating agent [154] that reduces the solubility of EVs <250 nm [153] while keeping proteins in the aqueous phase. PEG precipitation improves EV recovery compared to differential centrifugation, isolating up to 90% of EVs [153]. However, studies have shown relatively low purity in EV fractions compared to those isolated through differential ultracentrifugation [155-157] due to proteins stuck in the PEG matrix and thereby pelleted with EVs.

Performing microfiltration before differential ultracentrifugation saves time by removing cells and larger EVs [158, 159]. Commercially available ultrafiltration membranes separate exosomes from smaller proteins, rendering any centrifugation steps unnecessary [153]. However, clogging by contaminants or trapping of EVs produces low EV yields [154] in comparison to centrifugation. Filtration as an additional step before size-exclusion chromatography clears the biological fluid of larger particles [160, 161]. During size-exclusion chromatography, smaller proteins reside in the stationary phase while EVs elute more quickly (**Figure 13**) [118].

Appropriate selection of the matrix and accurate timing of elution collection are critical to the success of this isolation procedure.
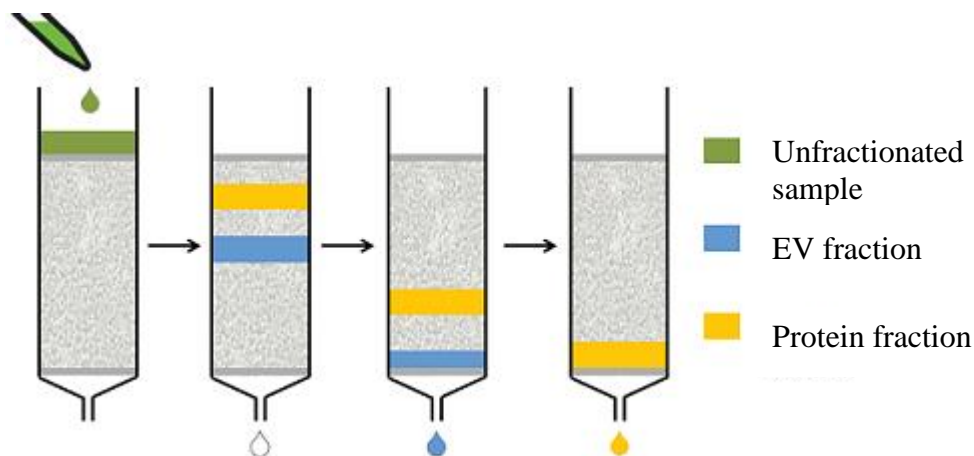
Figure 13. Illustration outlining size exclusion chromatography (SEC) for isolation of EVs.
The pores in the gradient preferentially trap the smaller proteins, causing EVs to elute faster and in a separate fraction. Reproduced from Biovision Incorporated, 2019, retrieved from https://www.biovision.com/e xopuretm-chromatography-columns.html. © 2018 by Biovision Inc.

None of the methods previously stated exclusively isolate cancer-derived EVs from the normal EV background, which could confound disease specific genetic signatures in downstream analysis. For example, isolation of glioblastoma patient EVs through differential ultracentrifugation resulted in lower mRNA expression of a tumor-specific gene EGFRvIII and created a higher background of GAPDH housekeeping gene, suggesting that size-based methods of EV isolation confound the expression of genes derived from disease-associated EVs [162]. Little consensus is provided within the literature for the number of EVs found in healthy individuals due to discrepancies between various isolation and enumeration techniques. However, to give an understanding of the EV background found in healthy individuals, ~ 10^7[163] to 10^9 [164] EVs are found in 1 mL of healthy plasma, with 50% of these EVs originating from either platelets or erythrocytes [163].

Immunoaffinity isolation serves as a method of mitigating background EVs confounding disease-related expression signals by selecting EVs through antibodies (Abs) bound to a surface, such as the surface of microbeads. For example, affinity-decorated microbeads can be incubated with the biological sample for time periods ranging from 1 to 4 h [165], then require post-processing steps such as magnetic separation and centrifugation to yield the final purified EV fraction. The antibody may select the general EV population by targeting tetraspanins (e.g. CD81, CD63, or CD9), or subpopulations derived from targeted cell types required for a specific clinical application. Researchers have targeted cell-specific markers for enriching EVs from a cancer origin [156, 166, 167], with one study using anti-HER2 Abs for the isolation of cancer-derived EVs from human breast cancer patients [168].

Immunoaffinity isolation produces highly enriched fractions of disease-associated EVs, as was shown in the average 10-fold increase of EV-associated proteins from immunoaffinity microbeads selecting for EpCAM from colorectal cancer EVs in comparison to differential ultracentrifugation which resulted in a higher protein concentration, but lower enrichment of EV-associated proteins [156]. Immunoaffinity isolation of EVs has also proven to enrich EVs from ovarian cancer patient serum compared to healthy controls, amounting to detectable levels of miRNA from the anti-EpCAM isolated EVs from patient serum while the healthy serum produced no detectable miRNAs [169]. However, immunoaffinity isolation using microbeads may result in low purity with one study finding a 15-fold enrichment of the common plasma protein albumin from anti-EpCAM microbead isolated EVs when compared to differential ultracentrifugation with a sucrose gradient [170].

Each benchtop technique includes complex workflows comprised of multiple steps potentially requiring expensive equipment and experienced operators. Microfluidics may

improve upon these limitations by rapidly isolating EVs from small volumes (50 µL – 1 mL) on a single platform capable of performing multiple processing steps, thereby decreasing target loss or contamination risks [118]. Some technologies also integrate both EV enrichment and proteome or transcriptome analysis into one device through on-chip immunofluorescence assays or PCR, further simplifying the workflow and potentially eliminating the need for expert operators making EV-based assays more accessible.

Microfluidics for EV isolation. Many researchers have applied microfluidics to isolate EVs. Some platforms take advantage of size-based isolations by incorporating unique geometries to either direct the flow of EVs away from contaminants or directly capture EVs on the device. For example, microfluidics employing microfiltration as an isolation strategy [171, 172] may include a double-filtration set-up for initial large EV removal followed by a smaller pore membrane to eliminate proteins while capturing exosomes within the filter (**Figure 14A**) [173, 174]. Novel size-based sorting techniques not amenable to benchtop operation have also been used including nanowire trapping, acoustic isolation, deterministic lateral displacement (DLD), and viscoelastic flow sorting.
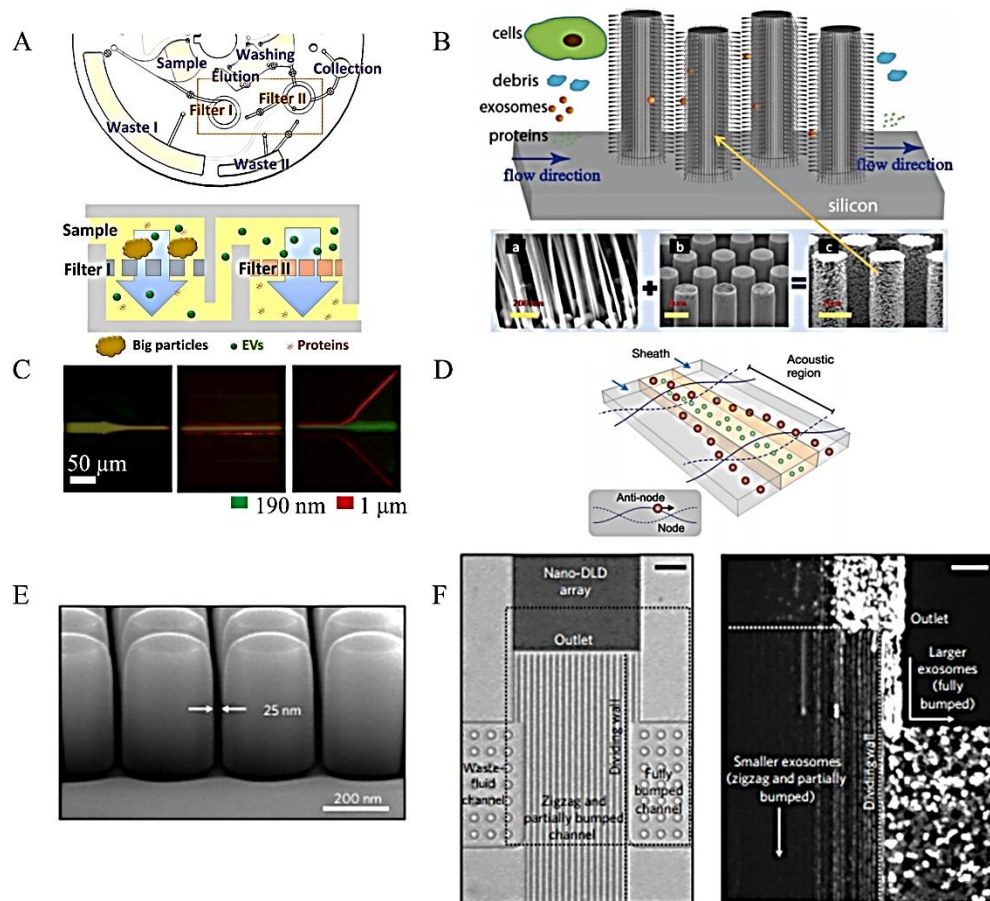
Figure 14. Microfluidics for size-based EV isolation

(**A**) Schematic of the Exodisc double-filter device (top), with a cross-sectional illustration of the EVs journey through the two filters. Reprinted with permission from "Exodisc for rapid, size-selective, and efficient isolation and analysis of nanoscale extracellular vesicles from biological samples," by Woo et al., 2017, *ACS Nano,* 11:2, p. 1361. © 2017 American Chemical Society [165]. (**B**) Schematic of a ciliated micropillar array showing the passage of cell debris and proteins, with exosomes trapped in the wires. The panel below shows the (a) silicon nanowires (200 nm scale bar), (b) micropillars (2 µm scale), and (c) fully assembled ciliated micropillars. Reprinted with permission of The Royal Society of Chemistry, from "Ciliated micropillars for the microfluidic-based isolation of nanoscale lipid vesicles," by Wang et al., 2013, *LOC,* 13:15, p. 2880.© 2013; permission conveyed through Copyright Clearance, Inc. [167]. (**C**) Application of the acoustic field concept illustrated in (**D**) with fluorescently labeled particles of different sizes injected. The larger particles are pushed toward the sides (1 µm). Adapted with permission from "Acoustic purification of extracellular microvesicles," by K. Lee et al., 2015, *ACS Nano,* 9:3, p. 2322,2324. © 2015 by American Cancer Society [170]. (**E**) Scanning electron microscope image of a nano-DLD sorting array with many of these pillars fabricated in the Nano-DLD array section of the device in (**F**), showing the schematic (left) and operation (right) of a nano-DLD device. Larger EVs displace laterally to congregate in the "fully bumped channel" while smaller exosomes follow the straight path through the device. Reprinted by permission from Springer Nature: *Nature Nanotech,* "Nanoscale lateral displacement arrays for the separation of exosomes and colloids down to 20 nm," by B. H. Wunsch et al., 2016, 11:11, p. 937,939. © 2016 [174].

Nanowires trap EVs much like filters but are placed vertically on micropillars and can dissolve in a solvent for EV release [175-177] (**Figure 14B**). Applying an acoustic field across a fluidic channel forms a force gradient that differentially effects particles based on their size, density, and compressibility to enrich EVs from a sample [178-181] (**Figure 14C, D**). This method eliminates clogging that may occur through trapping techniques. DLD separates particles using an array of different pillar geometries, forcing particles to move streamline or laterally based on their size. Particles with a diameter larger than the pillar spacing will displace horizontally, while smaller particles follow the flow path [182, 183] (**Figure 14E, F**). EVs of varying sizes will experience differing elastic lift forces when flowing through a viscoelastic medium, pushing large EVs toward the center and leaving exosomes along the channel sidewalls [184]. However, this approach needs further investigation using complex biological fluids.

Size-based microfluidic isolation methods incur similar shortcomings to benchtop methods in their inability to selectively isolate disease-associated EVs. However, these techniques could provide benefit in the research and study of EV biology and physiology by enriching all EV subpopulations. Immunoaffinity isolation techniques must be employed when isolating disease-specific EVs in order to prevent the loss of disease-related mRNA or miRNA expressions because of a large background of EVs (see immunoaffinity section of bench top techniques for further discussion) [162].

Microfluidics may use microbeads containing surface-immobilized antibodies as demonstrated on the benchtop using magnetic beads or direct attachment of antibodies to the surface of a microfluidic device. Integration of microbeads into a microfluidic platform may eliminate handling steps, therefore decreasing the risk of contamination and complexity of the assay compared to benchtop immunoaffinity techniques. However, microfluidics requiring

incubation of sample and beads off-chip for isolation offer little benefit in decreasing operator steps or assay time. Coupling initial sample preparation to a device that can perform on-chip analysis of target molecules such as proteins mitigates this limitation by decreasing handling steps post-processing [129, 185, 186]. Researchers have also developed microfluidic devices with internal incubation (**Figure 15A,B**) [187], facilitated by on-chip mixing and microbead trapping [188, 189]. Immunoaffinity capture through microbeads provides a large surface area-to-volume ratio for potential high loads of EVs. However, microbeads add cost to the assay and may still require long incubation times, potentially leaving direct surface modification as a more viable alternative.

Surfaces of microfluidic devices may be immobilized with antibodies through coupling reactions, such as EDC/NHS or avidin/biotin [95]. Chen *et al.* initially demonstrated surface modification for isolating EVs in a straight microchannel populated with herringbone grooves to facilitate convection, increasing EV interaction with the device surfaces to improve recovery [190]. Another device immobilized antibodies on a mica surface to capture EVs for subsequent AFM analysis [191]. Kanwar *et al.* used reservoirs serially attached through small microchannels to increase the recovery of EVs by increasing residence time (**Figure 15C-E**) [192]. These devices were only optimized and developed through pan-EV markers, such as tetraspanins for isolation of all EV subpopulations. Therefore, they did not provide evidence for the ability to isolate specific disease-associated EVs that may be necessary for use in liquid biopsies.
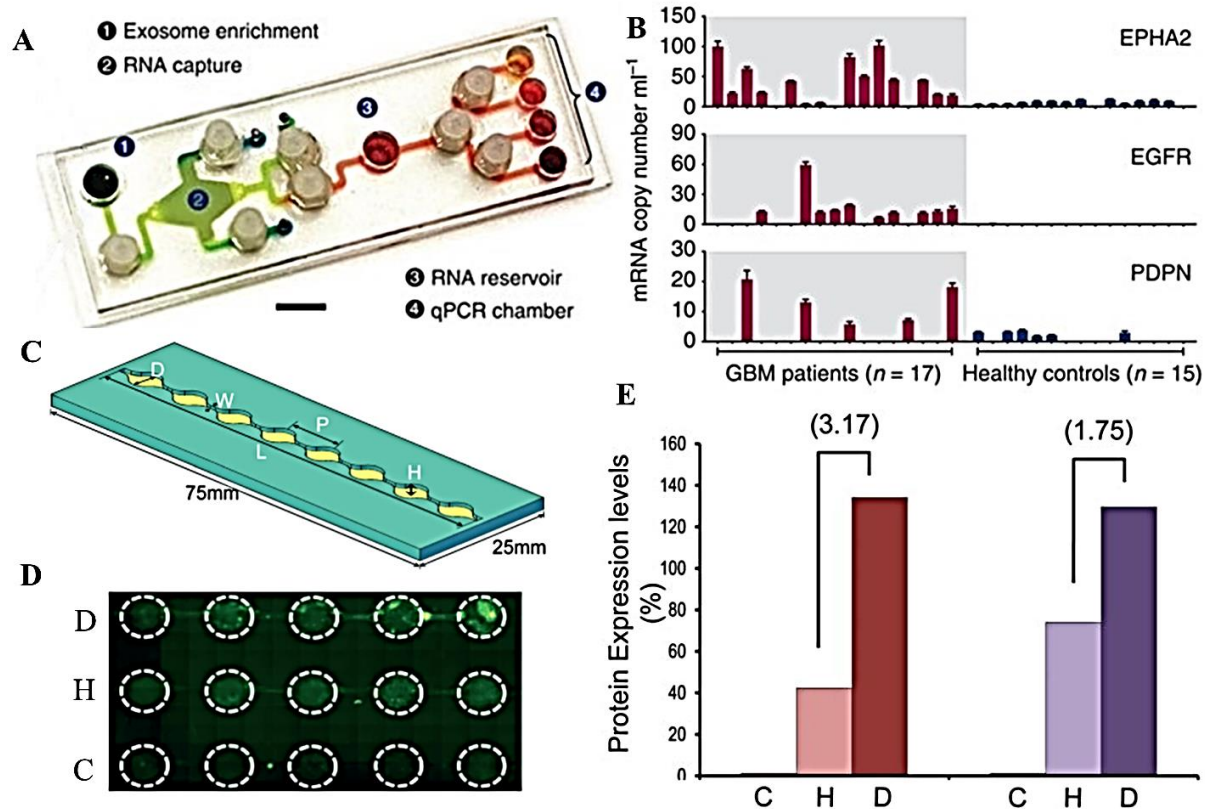
Figure 15. Microfluidic immunoaffinity isolation of EVs.

(**A**) Schematic of the immunomagnetic exosomal RNA (iMER) platform. Scale bar is 1 cm. (**B**) Average higher mRNA copies of three genes associated with glioblastoma were observed in the patient samples compared to healthy controls. Reprinted from *Nat. Comm.*: " Chip-based analysis of exosomal mRNA mediating drug resistance in glioblastoma," by Shao et al., 2015, Vol. 6, p. 3, 7. © 2015 Macmillan Publishers Limited. With permission under CC-BY: https://creativecommons.org/licenses/by/4.0/legalcode. Link to publication: https://www.nature.com/articles/ncomms7999#additional-information [178].(**C**) The ExoChip design. 5 mm diameter (D), 9 mm spacing (P), 73 mm length (L), and 100 µm height (H). These reservoirs are connected through narrower channels featuring a width of 0.75 mm (W). The anti-CD63 immobilized extracellular vesicles were stained with DiO, then quantified using the encircled areas to calculate fluorescence intensity collected from fluorescence microscopy images. (**D**) The reservoirs infused with pancreatic cancer samples (D) show higher concentration of EVs than the healthy (H) samples, with little fluorescence present in the non-specific light chain's immunoglobulin (LC-IgG) control (C). (**E**) Protein expression levels of the isolated EV populations were then calculated using densitometry analysis in image J. The plot shows relative densities for the control (C), healthy (H), and disease (D) samples. The brackets indicate fold change in expression levels between the diseased (D) and healthy (H) EVs. Reproduced with permission of The Royal Society of Chemistry, from "Microfluidic device (ExoChip) for on-chip isolation, quantification and characterization of circulating exosomes," by S. S. Kanwar, C. J. Dunlay, D. M. Simeone, and S. Nagrath, 2014, *LOC,* 14:11, p. 1892, 1897. ©2014; permission conveyed through Copyright Clearance Center, Inc. [183].
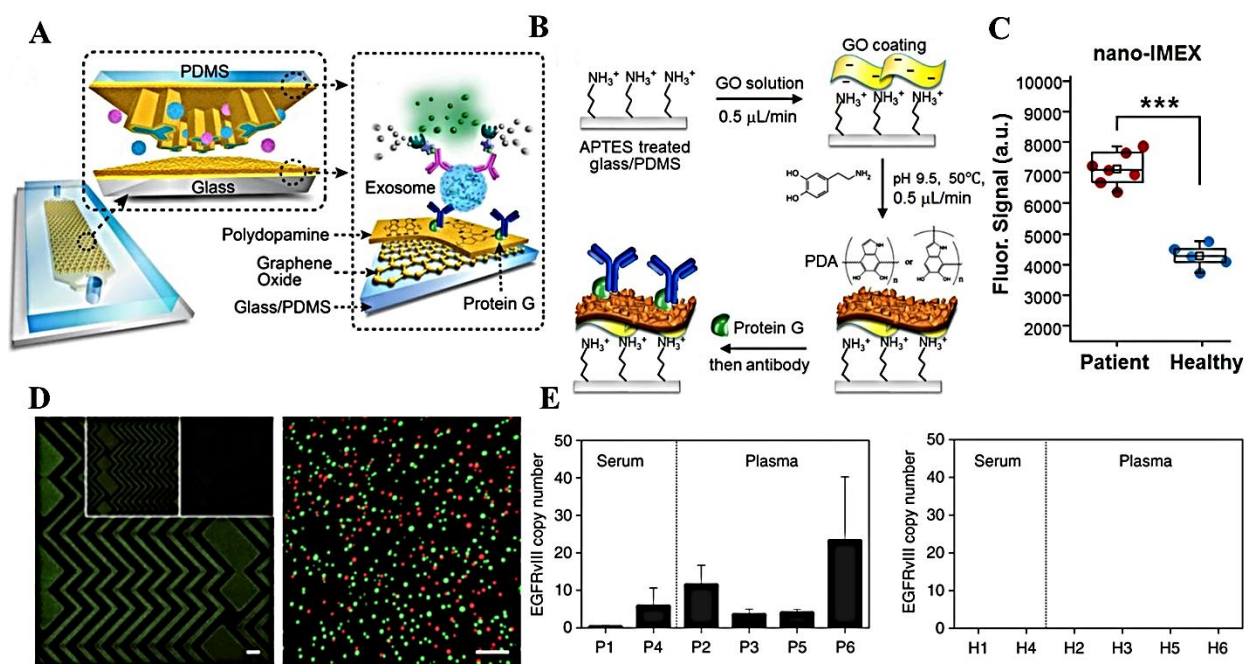
Figure 16. Surface modification with 3D nanostructuring for isolation of EVs.
(A) Schematic of the nano-interfaced microfluidic exosome platform (nano-IMEX), made of glass/PDMS coated with graphene oxide (GO)-induced, nanostructure polydopamine (PDA) film. The scheme also highlights Y-shaped microposts built on the surface. **(B)** The PDA-induced 3D nanostructuring through an intial GO coating for attachment of proteins and antibodies subsequently attached. **(C)** Ovarian cancer samples produced a fluorescence intensity significantly higher (***$p < 0.001$) than that found from healthy controls. Reprinted from The Royal Society of Chemistry: " Ultrasensitive microfluidic analysis of circulating exosomes using a nanostructured graphene oxide/polydopamine coating," by P. Zhang, M. Hei, and Y. Zeng, 2016, *LOC,* 16:16, p. 3034, 3040. © 2016. Permission under the CC BY-NC: https://creativecommons.org/licenses/by-nc/3.0/legalcode. Link to publication: https://pubs.rsc.org/en/content/articlehtml/2016/lc/c6lc00279j [184]. **(D)** Microscopy images showing successful capture of fluorescently labeled EVs in the herringbone channels through selective isolation using cetuximab (large under-layed image, scale bar 50 µm), anti-EGFRvIII (left insert), or a cocktail of both (right insert). **(E)** Signals of EVs from glioma cells encoding either palmitoylated-tdTomato (red) or -GFP (green). Scale bar 1 µm. **(F)** Healthy plasma EVs captured produced no EGFRvIII copies, delineating them from the glioblastoma samples. EVs were isolated using an antibody cocktail, and copy numbers were normalized to sample input. Reprinted from *Nature Comm.:* "Engineered nanointerfaces for microfluidic isolation and molecular profiling of tumor-specific extracellular vesicles," by Reategui et al., 2018, 9:1, p. 3,6. With permission under CC-BY: https://creativecommons.org/licenses/by/4.0/legalcode. Link to publication: https://www.nature.com/articles/s41467-017-02261-1#rightslink [185].

Recent microfluidic devices have selectively targeted host-cell specific EVs to investigate the clinical relevance of these biomarkers. Most have modified the surface within the

microfluidic to maximize recovery without increasing the device footprint. Zhang *et al.* used a coating of nanopores created through a layer-by-layer deposition of graphene oxide and polydopamine to increase capture surface area while a Y-shaped microstructure facilitated mixing for EV-surface interactions [193] (**Figure 16A-C**). This technology selectively detected ovarian cancer-derived EVs using anti-EpCAM selection. The herringbone device previously developed by Chen *et al. [190]* was modified from its original design to include layer-by-layer deposition of functionalized nanopores to increase the recovery of glioblastoma-derived EVs[162] (**Figure 16D-F**). Another microfluidic composed of nanohole arrays functionalized with anti-EpCAM and anti-CD24 antibodies on a gold surface specifically captured ovarian cancer cell-derived EVs [121].

Though several microfluidic devices have been developed for the immunoaffinity capture of EVs through surface modification, they often lack definition of performance parameters, such as recovery, purity, and EV load (**Table 5**). The high recovery and purity of EV fractions from biological samples is extremely important when using them for downstream proteome, transcriptome, or genome analyses.

Further, many of the aforementioned technologies are based on complex and time-consuming fabrication methods and thus, do not coincide with high-scale manufacturing to accommodate clinical applications that demand one-time use devices. Therefore, a need exists for a high purity, high recovery, and high yield EV isolation platform whose fabrication is low cost for accommodating large-scale clinical studies to facilitate the discovery of EV-associated biomarkers for use in cancer liquid biopsies. Further, only a few microfluidic devices have been applied for isolation of EV RNA for mRNA expression analysis and was implemented in

glioblastoma patient samples [121, 162], highlighting another need for new microfluidic technology geared toward isolation of EVs for internal cargo assessment.

Table 5. Performance of microfluidic technologies for EV purification.
NP refers to nanoparticles as some studies only used polystyrene beads or liposomes for characterization. NR means the value was not reported. Adapted from "Microfluidics for exosome isolation and analysis: enabling liquid biopsy for personalized medicine," by J. C. Contreras-Naranjo, H. J. Wu, and V. M. Ugaz, 2017, *LOC,* 17:21, p. 3562. ©2017 by the Royal Society of Chemistry [114].

Microfluidic technology	Separation Property	NP capacity	Throughput (μL/min)	Recovery	Purity	Ref.
Nanowire trapping	Size	NR	10	10%	NR	[175]
Membrane filtration	Size	4×10^{10}	20	65%	83.6% removal of proteins	[172]
Exodisc (filtration)	Size	1.47×10^{11}	36	95.7%	>95% removal of proteins	[173]
Double filtration	Size	NR	33	74.2%	80% removal of proteins	[174]
Membrane filtration	Size	NR	2	1.5%	NR	[171]
Deterministic lateral displacement	Size	NR	0.0002	NR	NR	[182]
Deterministic displacement (DLD)	Size	NR	2.13	39%	98.5% of particles were desired microvesicles	[183]
Acoustophoresis	Size, density, compressibility	NR	~ 0.24	> 80%	NR	[178]
Acoustic trapping	Size, density, compressibility	NR	30	NR	NR	[180]
Large particle acoustic trapping	Size, density, compressibility	~25,000 microvesicles	10	~10%	88.6% of trapped particles were microvesicles	[181]
Continuous viscoelastic sorting	Viscoelastic flow	3×10^{10}	~3	93.6%	>90% purity of particles <200 nm from large particles	[184]
Microfluidic capture of affinity microbeads	Immunomagnetic beads	~5×10^{11}	2	NR	NR	[186]
		NR	2	NR	NR	[129]
RInSE	Immunomagnetic beads	NR	70	NR	38% nonspecific RNA for streptavidin coated beads with no antibody	[185]
iMER	Immunomagnetic beads	NR	4	>93%	<5% nonspecific binding on isotype control	[187]

Microfluidic technology	Separation Property	NP load	Throughput (µL/min)	Recovery	Purity	Ref.
ExoSearch	Immunomagnetic beads	NR	0.8	72%	NR	[188]
µMED	Immunomagnetic beads	~1×10^{10}	≤ 3	NR	~41% signal gain compared to isotype controls	[189]
Surface plasmon Resonance (SPR)	Affinity-purification	6×10^{10}	8.3	NR	4% SPR signal for isotype control	[121]
HB-Chip	Affinity-purification	NR	13.1	42-94%	13% nonspecific for isotype control	[190]
Nanostructured HB, 4 chips in series	Affinity-purification	Between 2×10^{7}-3×10^{7}	16.7	59% in PBS 8% in plasma	100-150 fold enrichment ratio for cell line mRNA (GFP)	[162]
ExoChip	Affinity-purification	NR	4	NR	NR	[192]
AFM-coupled mica device	Affinity-purification	~230	2	NR	0.6-37.6% nonspecific for isotype control	[191]
Nano-IMEX	Affinity-purification	2.2×10^{7}	0.05	NA	~10% nonspecific for no Ab control	[193]

Herein, an in vitro device for extracellular vesicle microfluidic affinity selection (EV-MAP) was developed which addresses the limitations stated above. The mechanism of isolation is immunoaffinity selection in order to capture only disease-associated EVs so any background EVs cannot mask or confound mRNA expression or expression differences between genes, as has occurred with implementing size and density-based technologies [162]. The EV-MAP device uses surface modification of mAb because it mitigates the need for time-consuming preparation steps and expensive microbeads which do not align well with the goal of creating a low cost one-time use disposable device. Further, as is also seen for the benchtop application of microbeads, microfluidic microbead assays often result in low purity (as seen in **Table 5**) when compared to surface modification.

EV-MAP is produced using a simple fabrication process of imprinting a pattern from a brass mold into a plastic substrate, thereby aligning with manufacturing methods for high-scale

production such as injection molding. Because these devices are made out of plastic, they are produced at low cost which makes them appropriate for one-time use in in vitro liquid biopsy tests unlike a majority of the microfluidics listed above (**Table 5**). The device consists of micropillar arrays which facilitate mAb-EV interactions by decreasing the diffusional distance required for EVs to come in contact with a mAb-conjugated surface to increase recovery and yield when compared to other surface modification microfluidic platforms (see **Table 5**), with many not even reporting on these parameters. Two forms of the EV-MAP device exist: one with three beds populated with micropillars set up in series while the other holds seven beds processed in parallel which creates a ~ 5-fold increase in surface area and consequently EV load. In this study, the three-bed design of EV-MAP was used.

The EVs isolated from the EV-MAP device are then lysed for transcriptome analysis through mRNA expression profiling, aligning the technology with analysis currently used in clinics for identifying molecular subtypes of breast cancer. This highlights the importance of maximizing EV load as EVs have been found to carry mRNA in quantities of 0.25% of the TRNA.

2.2 Methods

2.2.1 EV-MAP device fabrication and design

Fabrication procedure. The fabrication procedure is summarized in **Figure 17A**, with a diagram flow of the process in **Figure 17B.** The brass metal mold master was fabricated using high precision micromilling (KERN 44, KERN Micro- und Feinwerktechnik GmbH & Co.KG; Murnau, Germany) from a 100 µm milling bit (Precision Micro Tool). The 3" master contained two EV-MAP devices, each containing 3 beds with an array of 15,202 holes and inlet and outlet ports for capillary connections (365 µm OD, 150 µm ID, Polymicro Technologies). The EV-MAP device was embossed into 6013S-04 cyclic olefin copolymer (TOPAS Advanced Polymers) using the mold master at 162° C with 900 lb. of force using a precision press (Wabash MPI), with the replicated devices demolded at 150° C. A full cycle time for replication took 12 min. Mold release agent (MoldWiz® F57-NC), provided by Axel Plastics, kept plastic from sticking to the mold master.

The devices were then taped to cover channels and protect them from any debris produced while cutting them apart (Skil, 120V, 9-inch bandsaw). The tape was removed followed by sonicating the devices in 10% Micro-90® (Sigma-Aldrich). Subsequent rinsing with reagent-grade isopropyl alcohol (IPA, Fischer Scientific) and nanopure water was performed before devices were placed in a drying oven at 60° C for ≥ 60 min.
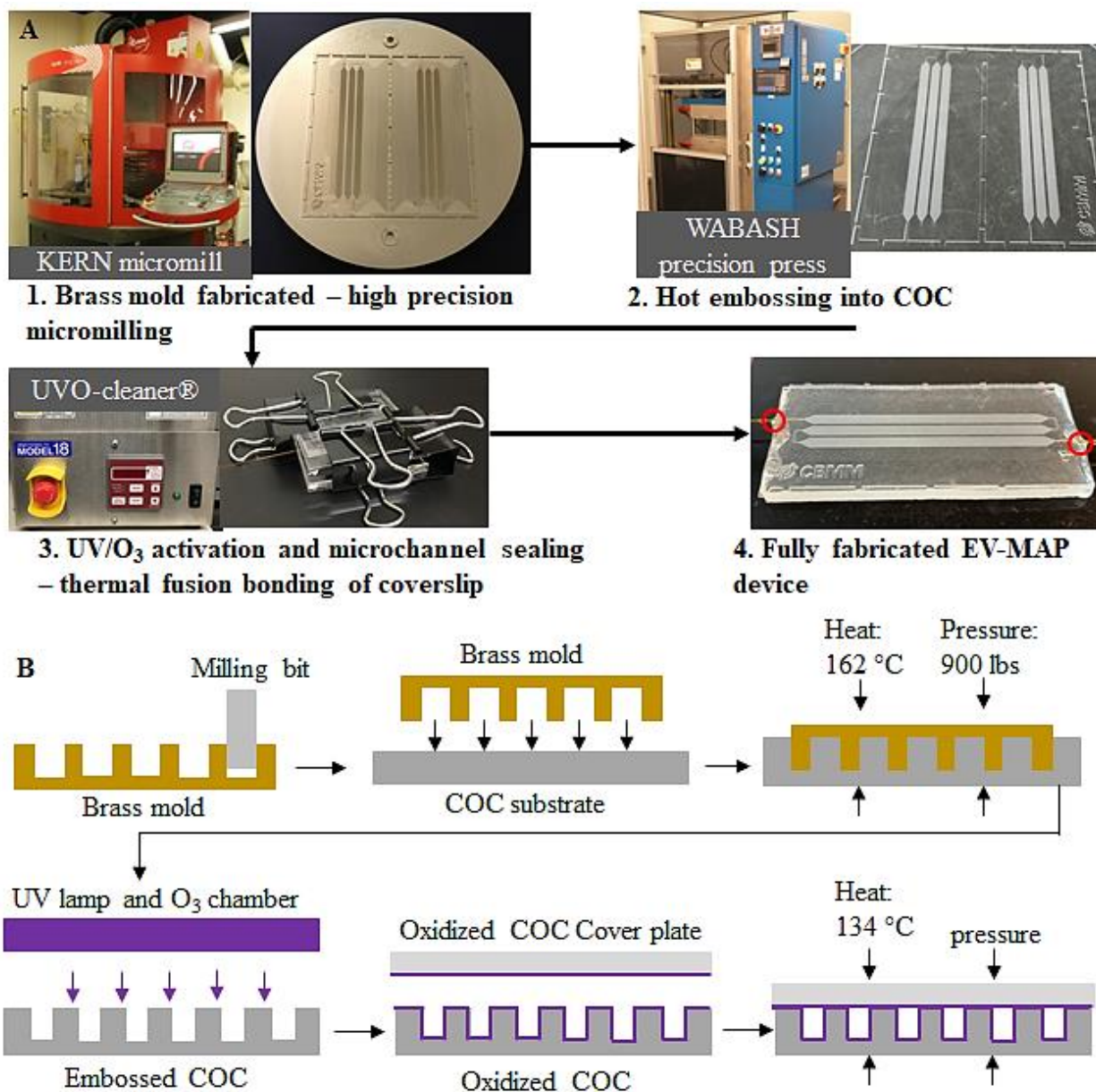
Figure 17. Fabrication procedure for the three-bed EV-MAP device.

(**A**) Process flow with pictures showing the EV-MAP device and equipment used at every fabrication step. The red circles indicate the epoxy capillary connections. (**B**) Diagram showing the process flow from brass mold fabrication using a high precision micromill to allow for high aspect ratios and micrometer dimensions, imprinting of the pattern from the mold to the COC plastic through hot-embossing for device replication, UV/O_3 irradiation treatment, and thermal fusion bonding to seal the microchannels to the cover plate.

The device channels were sealed by annealing a 250 µm COC cover plate to the device. A similar procedure involving 10% micro-90, IPA, and nanopure water cleaned the cover plates

before being placed in a drying oven. Both the cover plates and devices were UV/ozone irradiated for 13 min at 27 mW/cm^2 (measured at 254 nm wavelength) in a Model 18 UVO-Cleaner® (Jelight Company). Glass capillaries with a 150 µm ID (365 µm OD, Polymicro Technologies) were positioned at the outlet and inlet ports of the UV/O$_3$ modified device, with a cover plate placed over the top of the assembly (UV/O$_3$ modified side facing the channels). The assembly was secured between two glass plates clamped in position with alligator clips to apply adequate pressure to facilitate thermal fusion bonding (HeraTherm OGS60 General Protocol Oven, Gravity Convection, 2.3 Cu.Ft. 120V, Thermo Scientific) for 1 h at 134 °C. The capillary ports were then sealed with epoxy (Loctite® EA 9017, Henkel) after annealing to keep devices from leaking.

EV-MAP device design. The three-bed EV-MAP device contained three serially connected beds (**Figure 18A**) populated with circular micropillars (**Figure 18B**). The high precision micromill created a 4.6° draft angle in the holes of the brass master mold from the drilling bit, transferring this slope along the 92 µm height of the micropillars. This caused a gradient of pillar diameters from 110 µm at the top to 120 µm diameter at the bottom and with an approximate 10 µm pillar spacing (**Figure 18C**) along the pillar shaft. The small interpillar spacing relative to the pillar height created an aspect ratio of 10:1 for each pillar. **Table 6** lists all the device specifications.
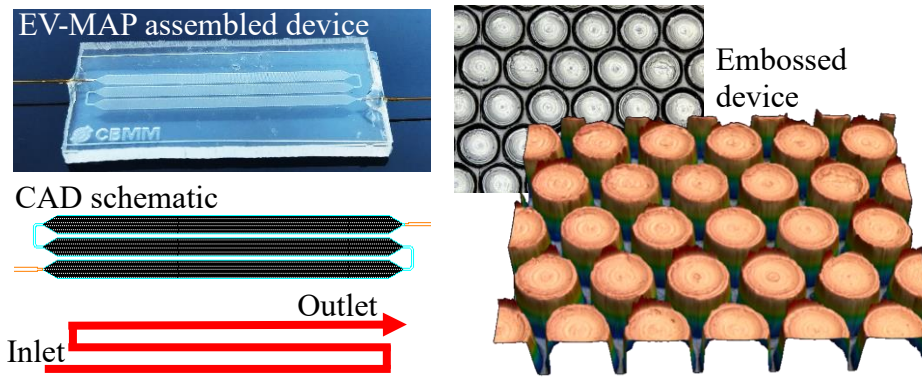
Figure 18. Computer aided drawings (CAD), microscopy images, and photo of the three-bed EV-MAP device. Image of the fully assembled device, CAD schematics illustrating the serial connection of three beds, each containing micropillars to form high aspect ratio microchannels as shown from Keyence laser scanning microscopy image (orange) and the light microscopy image of the device after embossing.

Table 6. List of device dimensions for the three-bed EV-MAP.

Dimension	Value
Pillar height	92 ± 3 μm
Pillar diameter	109 ± 3 μm
Inter-pillar spacing	10 - 20 μm
Draft angle	4.6°
Total bed length	122 mm
Number of pillars	15,202
Surface area	7 cm^2
Internal volume	7 μL

2.1.2 EV-MAP surface modification

Soper *et al.* has previously applied UV/O$_3$ irradiation to activate thermoplastic surfaces [194]. The UV exposure and oxidative stress simultaneously create O$_3$ molecules that break bonds to form free radicals, while also forming free radicals in the plastic that may fragment or crosslink polymer chains [195]. The free radicals may then react with other free radicals in the polymer to form carboxylic acid groups on the surface. Previous studies have investigated the use of UV/O$_3$

irradiation on COC, with results showing successful creation of carboxylic acid groups [195, 196].

Covalent coupling reactions were then used to chemically attached mAbs to the carboxylic acid surface groups. The covalent coupling reaction uses EDC (1-Ethyl-3-(3-dimethylaminopropyl)-carbodiimide) and NHS (N-hydroxysuccinimide) to react with the carboxylic acid groups (-COOH) to form a succinimide ester intermediate that subsequently reacts with primary amine groups found on the mAbs. EDC/NHS coupling has been used to immobilize mAbs to the surfaces of thermoplastic microfluidic devices in the past [197, 198], including devices fabricated in COC [98, 194]. The EDC/NHS coupling procedure used for the EV-MAP device was slightly modified from the protocol established by Witek *et al.* for CTC isolation [98], as acetonitrile (ACN) was the solvent used during the reaction instead of MES buffer because it is a dry organic solvent and would therefore minimize any hydrolysis that could occur. This modified procedure is shown in **Figure 19**.

Twenty mg/mL of EDC was combined with 2 mg/mL of NHS and dissolved in dry reagent-grade anhydrous ACN through vigorous vortexing. Then, this mixture was immediately injected into an assembled device and incubated at room temperature for 25 min. Ten µL of nuclease-free water displaced the ACN before injecting the mAb to mitigate precipitate formation due to mAb reconstitution in PBS buffer (0.68 mg/mL in PBS, pH = 7.4). The devices were incubated at room temperature for 2 h before being placed in a 4°C refrigerator overnight. If devices were not used the next day, they were stored for up to 1 month at 4°C in a Protein Stabilizing Cocktail (2X in PBS, Thermo Fischer).
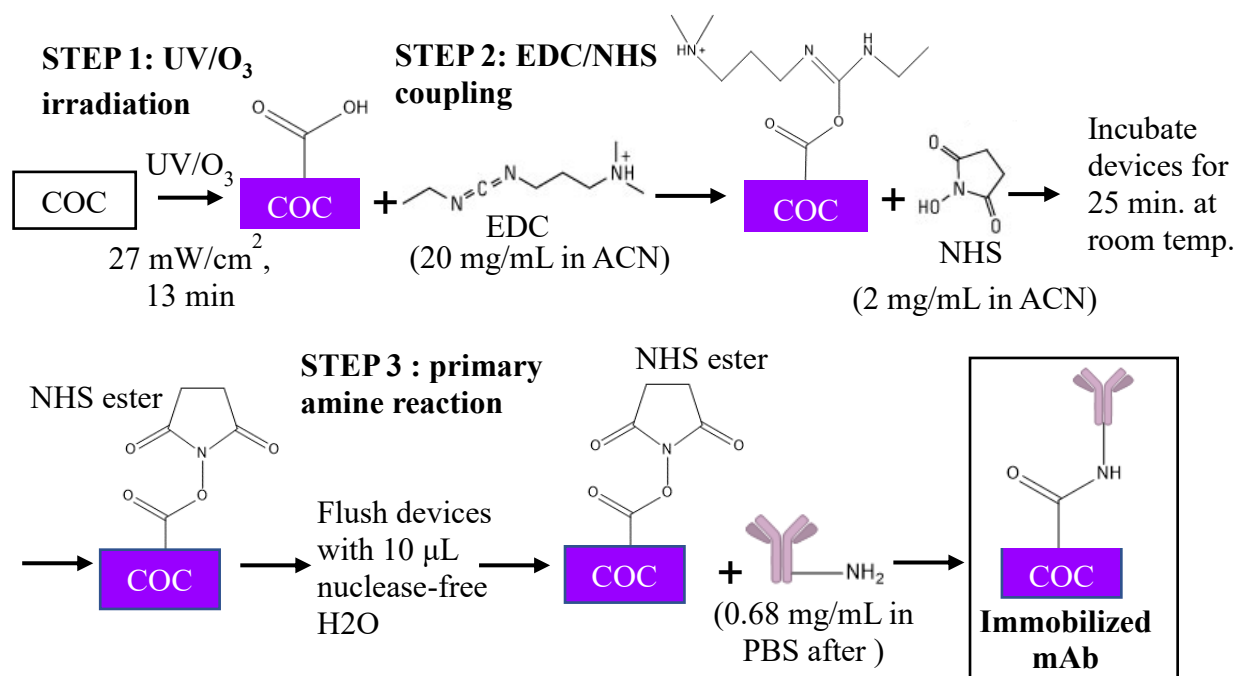
Figure 19. Process flow and reaction chemistry of the EV-MAP mAb conjugation reaction. After UV/O$_3$ irradiation of the devices, carboxylic acid groups are formed on the surfaces. These carboxylic acid groups (-COOH) serve as anchors for the EDC/NHS-mediated immobilization. Twenty mg/mL of EDC and 2 mg/mL of NHS were dissolved in ACN buffer and quickly infused into the EV-MAP devices. During the 25 min incubation period, the EDC forms an o-acylisourea through binding with the carboxylic acid group. This intermediate is quickly replaced by the NHS to form a more stable NHS ester. Devices are then quickly flushed with nuclease-free water then infused with mAb. These mAbs conjugate with the carboxylic acid groups through their primary amine group, attaching them to the COC device surface for capture of EVs expressing the antigen of interest.

The efficiency of the EDC/NHS coupling reaction was analyzed through parallel immobilization of a 5' -amino, 3' -Cy5 oligonucleotide linker (5' -NH2-C12-T$_8$CCCTTCCTCACTTCCCTTTUT$_9$-Cy5; HPLC-purified, 1 mM stock solution in nuclease free water and diluted to 10 µM with PBS; Integrated DNA Technologies) during each mAb immobilization procedure (**Figure 20A, B**). The oligonucleotide functionalized devices were washed with 0.1% sodium dodecyl sulfate (SDS, Life Technologies) (25 µL/min, 40 min) then displaced with ≥200 µL PBS (pH 7.2). The oligonucleotide-immobilized device was imaged with a 200M inverted microscope (Zeiss) using a 10X objective (0.3 NA, Plan NeoFluar), XBO

75 Xe arc lamp, single band Cy5 filter set (Omega Optical), Cascade 1K EMCCD (Photometrics), and MAC 5000 stage (Ludl Electronics Products). These images were then background subtracted and analyzed using a custom macro (**Appendix A1**) input into Image-J software. Comparison of the intensity values showed a significant difference between the EDC/NHS and ACN control ($p < 0.00001$ for 95% confidence under two-tailed t test; **Figure 20B**).
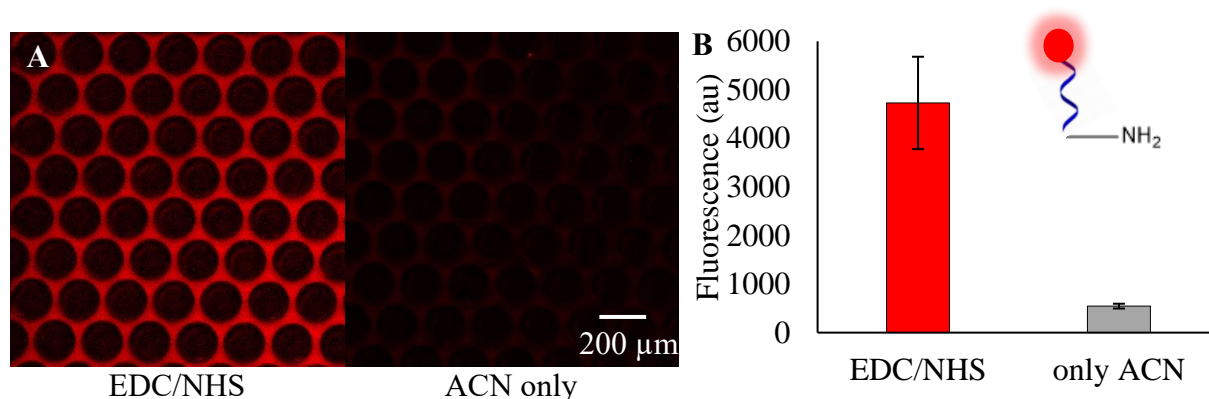
Figure 20. Immobilization efficiency of the EV-MAP EDC/NHS coupling reaction.
(**A**) Fluorescence microscopy images taken with a Cy5 filter on a 200M inverted Zeiss microscope after EDC/NHS-modulated immobilization of the 5'-NH$_2$ oligonucleotide fluorescent reporter used to verify successful EDC/NHS coupling for mAb immobilization. The positive control (image on the left) included EDC/NHS in ACN buffer, while the nonspecific control (image on the right) was treated identically but with only ACN buffer infused into the chip without the EDC or NHS reagents. Images are background subtracted, intensity scaled, and were imaged through a 10X objective. (**B**) Quantitative analysis of 9 images taken from either a single positive (EDC/NHS) and negative (ACN only) control device. Error bars correlate to these 9 images taken in 9 different locations on a single device. $P < 0.00001$ under a two-tailed t test.

Anti-EpCAM (clone 158210), anti-FAPα (clone 427819), and anti-CD81 (clone 454720) mAbs were used in these studies. Isotype controls were also employed for investigation of assay specificity using the anti-EpCAM isotype IgG$_{2A}$ (clone 20102) or the anti-CD81 isotype IgG$_{2b}$ (clone 20116). Devices were only modified with one type of mAb. All mAbs were secured from R&D Systems and derived from mice.

2.1.3 Sample preparation

Cell line media for EV-MAP characterization. MCF7, Hs578T, and SKBR3 cells were collected from ATCC, kept in liquid nitrogen, and cultured in 5% CO_2 at 37° C for ≤30 passages. Culture media consisted of MEM alpha (Gibco)/10% Fetal bovine serum (FBS, Performance, Gibco) augmented with 1 µL human insulin (Sigma)/mL MCF7 media, HydroClone™ DMEM high glucose (GE Life Sciences)/10% FBS for Hs578T cells, and McCoy's 5A (Corning)/10% FBS for SKBR3 cells. EVs secreted from FBS were removed by ultracentrifugation (100,000g, 18 h, 4° C) using an L8-80M ultracentrifuge (Type 45 Ti roto, 38 mm x 102 mm (70 mL) polycarbonate tubes; Beckman Coulter), and mechanical Harvard Trip balance (OHAUS). Tubes were sterilized with 10% hydrogen peroxide and cleaned with Virkon S (Dupont) when retrieved from the ultracentrifuge and carried to the culture hood. FBS was decanted, mixed thoroughly, aliquoted, and kept at -20° C. To extract EVs, cell lines were transferred to EV-depleted FBS-containing media and conditioned for one week, with the media decanted once cell lines reached 90% confluency. The cell lines were then centrifuged at 2000g for 10 min after decanting the media.

Plasma samples for EV-MAP characterization. Donor samples used in optimization studies of the EV-MAP assay were obtained from Bioreclamation IVT. Blood was collected from a donation center, freshly centrifuged to obtain plasma, immediately frozen, and shipped. The donors were tested for the presence of any infectious diseases such as HIV, but no other information about current health or health history was documented. Two samples came from female donors and two samples from male donors, with ages ranging from 46 to 55 years. The plasma samples were stored at -80° C until processed.

Healthy control samples were received from the University of Kansas Medical Center (KUMC). Blood was collected from women arriving at KUMC for routine mammograms, therefore ensuring no diagnosis or signs of breast cancer. Blood was stored in EDTA and immediately delivered, then centrifuged at 300g for 10 min, followed by two centrifugations at 2000g for 10 min with the plasma stored at -80° C until processed using the EV-MAP assay.

Breast cancer patient plasma samples were obtained from KUMC's Biospecimen Repository Core Facility (BRCF). All plasma samples were collected in 2017 and stored in liquid nitrogen until transported to the laboratory and stored at -80° C. Patient samples were also received from the University of Kansas Cancer Center's Indian Creek location. These samples were collected in the Spring of 2019, immediately centrifuged following the blood draw at 300g and twice at 2000g for 10 min to extract the plasma, and then stored at -80° C until processed using the EV-MAP device.

All patient samples were from women, with most ranging in age from 55-60 years old. Two patients were diagnosed with either ductal carcinoma in situ (DCIS) or invasive mammary carcinoma (IMC), with the rest diagnosed with invasive ductal carcinoma (IDC). Most samples were collected after some form of therapy was already administered. **Table A2** in the appendix summarizes both demographic and clinical information for all patients.

EV-MAP sample processing. Blocking buffers were filtered through a 0.22 µm PTFE syringe-fitting filter (Fisher Scientific) immediately before infusing 400 µL into the mAb-modified devices at 10 µL/min. All infusion steps were performed with a multi-channel New Era syringe pump using 1 mL syringes (BD). Devices were kept on ice during the blocking step. Plasma or conditioned media infusion occurred at room temperature with a volumetric flow rate of 2.1 µL/min, because this flow rate showed the highest recovery while still allowing time after

infusion for EV lysis within the same day to minimize TRNA degradation. The eluted sample volume was collected in microcentrifuge tubes and weighed to determine the true volume processed based on the measured fluid density. The devices were then placed on ice and rinsed with 400 µL of washing buffer at 10 µL/min. After the devices were washed, the EVs isolated on the surfaces were either released for EV enumeration, size characterization, and microscopy analysis, or directly lysed on-chip for EV mRNA expression profiling.

2.1.4 EV release from capture surface.

EVs were released from EV-MAP devices for nanoparticle tracking analysis (NTA) and transmission electron microscopy (TEM). Devices were manually infused with 60 µL of 0.2% proteinase K in PBS (or 0.05% trypsin/ 0.53 mM EDTA in certain cases), enclosed in a vacuum-sealed bag, and submersed in a water bath at 37°C for 30 min. The vacuum-sealed bag was then sonicated for 10 min at room temperature to mechanically disrupt any EVs physically adsorbed to the surface. Released EVs were eluted into 350 µL of PBS (10 µL/min), then stored at -80°C until performing NTA or TEM.

NTA. EV samples were heavily vortexed to homogenize each replicate, loaded into a 1 mL syringe (BD) and introduced into the flow cell of a NanoSight LM10 NTA instrument (Malvern Panalytical) equipped with either a 405 nm laser and NTA 3.2 software or a 488 nm laser and NTA 2.3 software. If the sample concentration fell outside the dynamic range of the instrument, the sample was diluted to 10-100 EVs per frame. A camera shutter of 1206, camera gain 366, 90-160 s acquisitions, and five averaged replicates were used to image the samples. Between images while the camera was turned off, the sample was manually advanced by ~25 µL to measure random portions of the sample for each replicate.

All processing used the Detection Threshold 5. After maintaining 5 replicates for a single sample, the flow cell was rinsed with 1 mL PBS then infused with air four times. The flushing procedure was validated by visually monitoring the number of nanoparticles observed in 300 µL PBS (~0-1 per 100 µL). Particle concentrations were normalized to the total sample volume processed through the devices.

TEM. TEM grid preparation procedures were adapted from Théry *et al.* [199]. Ten µL of sample was placed on copper grids (Carbon Type-B, 200-300 mesh, Ted Pella) and incubated for 20 min while covered with parafilm to keep them from drying out. Each grid was rinsed with 100 µL of water eight times for the duration of 2 min each. After washing the grids, the sample was stained with 50 µL uranyl acetate (0.4% w/v, pH 4, filtered through 0.22 µm). The grids were then blotted on filter paper to remove any unabsorbed staining reagent and placed in a grid holder until TEM was performed.

2.1.5 EV mRNA profilingEV or cell lysis for extraction of TRNA. EVs were lysed directly from EV-MAP devices by injecting 100 µL TRI Reagent® (Zymo Research), which was collected in microcentrifuge tubes. The devices were incubated at room temperature for 5 min and infused with another 100 µL of TRI Reagent®. Any remaining fluid in the devices was then displaced with air. In certain cases, TRNA was extracted directly from cells by resuspending the pellet in 300 µL of TRI Reagent® through vortexing after centrifuging cell culture media at 300g for 10 min.

TRNA purification and reverse transcription. TRNA was purified following the manufacturer's protocol for the Direct-zol Microprep kit (Zymo Research) and eluted in 6.5 - 8.5 µL of nuclease free water for EV-TRNA or 8 - 10 µL of nuclease free water for cell TRNA. Two µL of purified TRNA was subsequently analyzed with a 2200 TapeStation and high sensitivity

RNA tape, buffer, and ladder (Agilent Technologies) according to the manufacturer's procedure. Though the electrophoresis conditions for the high sensitivity tape are unknown, it is probably run on a 3% denaturing agarose gel at 5 V/cm and samples loaded with formaldehyde loading buffer including 0.4% bromophenol blue and xylene cyanol. Less than 1 µg of cell-derived TRNA or 2 µL of EV-TRNA was reverse transcribed into complementary DNA (cDNA) through the ProtoScript® II First Strand cDNA Synthesis Kit (New England Biolabs) using poly(dT) primers and the manufacturer's procedure. Negative controls during reverse transcription (RT) were created by replacing the enzyme mix with an equivalent volume of nuclease free water.

Droplet Digital PCR (ddPCR). After synthesizing cDNA, ddPCR was performed using the QX200™ Droplet Digital™ PCR System (BioRad). This procedure partitions a single PCR reaction into 20,000 water-oil emulsion droplets to increase the fluorescence signal generated by a DNA target molecule by decreasing the volume of each individual "reaction" or droplet to one nanoliter. This then allows for low quantities on the level of 4 copies to be accurately measured to result in absolute copy information.

A volume of 2.2 µL of cDNA from reverse transcription reaction was mixed with 11 µL QX200™ ddPCR™ EvaGreen® Supermix (BioRad), 2.2 µL of combined forward and reverse primers at 125 nM (primer design seen in **Table 7**), and 6.6 µL of nuclease free water for a final volume of 22 µL to ensure accurate pipetting of 20 µL into the PCR.

Reaction mixes were parsed into droplets using the instructions provided by the QX200™ Droplet Generator manufacturer (Bio-Rad), where the sample is randomly distributed based on a Poisson distribution so a single droplet either contains no template or one or more templates of DNA. The QX200™ Droplet Generator applies a vacuum to the wells filled with either oil or sample to draw the fluids into a flow-focusing junction and create monodisperse

droplets. The cDNA contained in the droplets was then amplified using a C1000 Touch™

Thermal Cycler with a 96-well Fast Reaction Module (Bio-Rad) under the following protocol:

95° C for 5 min, 40 cycles of: 95° C for 30 s, 50° C for 30 s, and 72° C for 1 min, 4° C for 5

min, and 90° C for 5 min. A final step of 4° C was used to cool the reaction mixture. After PCR

amplification, the 96-well plate was placed in the QX200 droplet reader (Bio-Rad), with the

fluorescence signals analyzed through QuantaSoft software (Bio-Rad). The resulting copy

concentrations (copies/µL) were then normalized to the concentration of TRNA input into the

reverse transcription reaction accounting for cDNA dilution factors when necessary.

Table 7. Primer designs for ddPCR amplification of cDNA.
These primers were specifically designed to amplify sequences close to the mRNA's poly(A) tail and span the
length of two exons, reducing the risk of amplifying genomic DNA through the intron. The gene panel chosen
includes epithelial genes (*EpCAM, CRT19*), mesenchymal genes (*VIM, FAPv2*), breast cancer stem cell markers
(*CD24, CD44*), a common EV tetraspanin *CD81*, and angiogenic cytokine *IL8*.

Gene/cDNA	Forward 5'-3'	Reverse 5'-3'	Product size (bp)
EpCAM	TTTTAAGAAATTCAGTTTAAAATGTT	ACTGATTTGTGATTGAAAGC	104
CRT19	CCCTTGGACCATAAATTTTTA	CTTCTGCTGTCCTTTGG	108
CD24	TTGCTCTTTCAGCCATT	GTTTGTGTATTTACGCTTTG	96
CD44	TCGAAGAAGTACAGATATTTATTAT	ATTAAACCCTGGATCAGTC	107
Vim	TTTCCAAAGATTTATTGAAGC	AATCTTGTGCTAGAATACTTT	112
FAP v2	TAGCACTTGAACTTCTGA	AAGGGAGTCATGCATTT	87
CD81	GGAGGGAACAAGGTGAG	TGTAGGTGGCGTGTATG	210
IL-8	AAGTTTCAACCAGCAAGAA	TGATACTCCCAGTCTTGTC	131

The software program uses the fraction of positive droplets, p, and the probability that a

certain amount of copies will be present in a droplet determined by a Poisson distribution, p, to

calculate the amount of copies per droplet of end product using the equation:

$$copies\ per\ droplet = -\ln(1 - p) \qquad (Eq.\ 1)$$

With the number of droplets generated known through the detection of the Eva Green dye which only fluoresces if it attaches to double-stranded DNA (dsDNA) product. The absolute amount of target product can then be obtained, with the graph in **Figure 21** applying a Poisson distribution based on the number of positive droplets to result in copies/µL. The dynamic range of the instrument according to the Bio-Rad QX200 ddPCR manual is from 4 to 100,000 total copies detected in the 20 µL reaction.
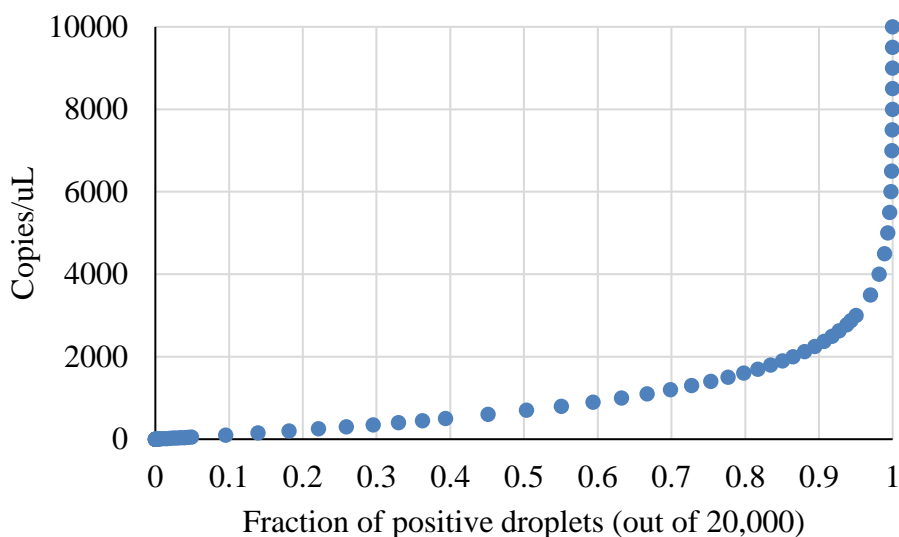
Figure 21. Copy concentrations calculated by the QuantaSoft software (Bio-Rad).
ddPCR resulting copy concentrations are calculated by the software program by measuring the fraction of positive droplets through fluorescence detection of the product-annealed Eva Green dye. The software then applies Poisson statistics based on this fraction of positive droplets, as the cDNA target molecules are parsed into droplets based on a Poisson distribution. The fraction of positive droplets is calculated based on a maximum of 20,000 droplets produced by the QX200 Droplet ™ Generator (Bio-Rad). The dynamic range of the QX200™ Bio-Rad ddPCR is from 0.2 copies/µL to 5,000 copies/µL according to the manufacturer's user manual.

Copy results were then normalized back to the mass of total RNA (TRNA) input into the reverse transcription (RT) reaction (2 µL of TRNA), considering any dilutions made to the cDNA before adding to the ddPCR reaction as well as the dilution inherent of taking 2.2 µL of cDNA out of the 20 µL cDNA reaction volume through the following equation:

$$\frac{copies}{ng\ TRNA} = \frac{\frac{copies}{\mu L}*20\ \mu L\ (reaction\ volume)*dilution\ of\ RT\ product\ added}{\frac{ng}{\mu L}*input\ volume\ of\ TRNA\ into\ RT} \qquad \text{(Eq. 2)}$$

Any heat map plots were then either scaled based off of the highest normalized copy value found in a single heat map, or each individual column in the heatmap was scaled to the highest expressed gene resulting within the sample creating a ratio from 0 to 100%.

2.2 Results and Discussion

2.2.1 EV-MAP device fabrication and replication fidelity

Future applications such as translation into commercialization or use in large clinical trials were considered when choosing a fabrication procedure for the EV-MAP device. The hot embossing of thermoplastic provided these capabilities by facilitating high throughput device manufacturing critical to any large-scale implementation. Further, the thermoplastic substrate is low cost and easy to handle making it an attractive material for such applications, and also working as a viable material for future industrial manufacturing through injection molding[196]. COC was chosen because it is known to create relatively higher uniform carboxylic acid coverage after UV/O$_3$ irradiation than other thermoplastic materials such as poly (methyl methacrylate) (PMMA), therefore facilitating high mAb surface load onto the EV-MAP device following UV/O$_3$ activation [195].

To assess the fidelity provided through the fabrication procedure to the original device design (see **Figure 18B**), profilometry was performed on the mold master and replicated devices after hot embossing with a Keyence VK-X 3D laser scanning confocal microscope equipped with a 10X objective. Example images obtained for the mold master and embossed device are shown in **Figures 22A, B**. Pillar diameters, spacing (top and bottom), and pillar heights were measured for assessing accurate pattern transfer. The Keyence could not image through the cover plates or plastic bottom of the device after annealing because the microscope uses light scatter to

generate the topography of the surface. When light hits another medium such as a cover plate before reaching the structures, the path bends both on its way through and out of the device and would create an inaccurate profile of the geometry. Instead, devices were imaged at 9 locations after annealing the cover plate to the embossed device via a Nikon Optiphot 2 Trinocular microscope with a 10X objective (0.30 Ph1), Nikon 12V 100W Halogen Lamp, and 5MP USB3.0 Real-Time Live Video Microscope Digital Camera (AmScope) using the AmScope 3.7 software (**Figure 22A**). Final images after annealing were analyzed using a custom macro (**Appendix A3**) created for ImageJ software to measure the interpillar spacing and pillar diameters. However, pillar height could not be assessed using this method.

Each stage in the fabrication procedure showed high reproducibility from the mold to the final assembled device (**Table 8**). Only one spacing value could be measured using the images obtained from the Nikon microscope for annealed devices. Therefore, the top and bottom spacings were averaged together to determine an overall spacing from the mold and embossed devices. Both the pillar diameters and spacing showed no significant difference throughout the fabrication procedure (**Table 8**), with $p > 0.05$ for 95% confidence between all data sets from a two-tailed t test. Hot embossing also had little effect on the pillar height; showing no significant difference with respect to the height measured from the mold master ($p > 0.05$ for 95% confidence using two-tailed t test). Maintaining the designed architecture of the EV-MAP device

was critical for maximizing EV recovery determined through simulations which helped optimize these device dimensions (discussed below).
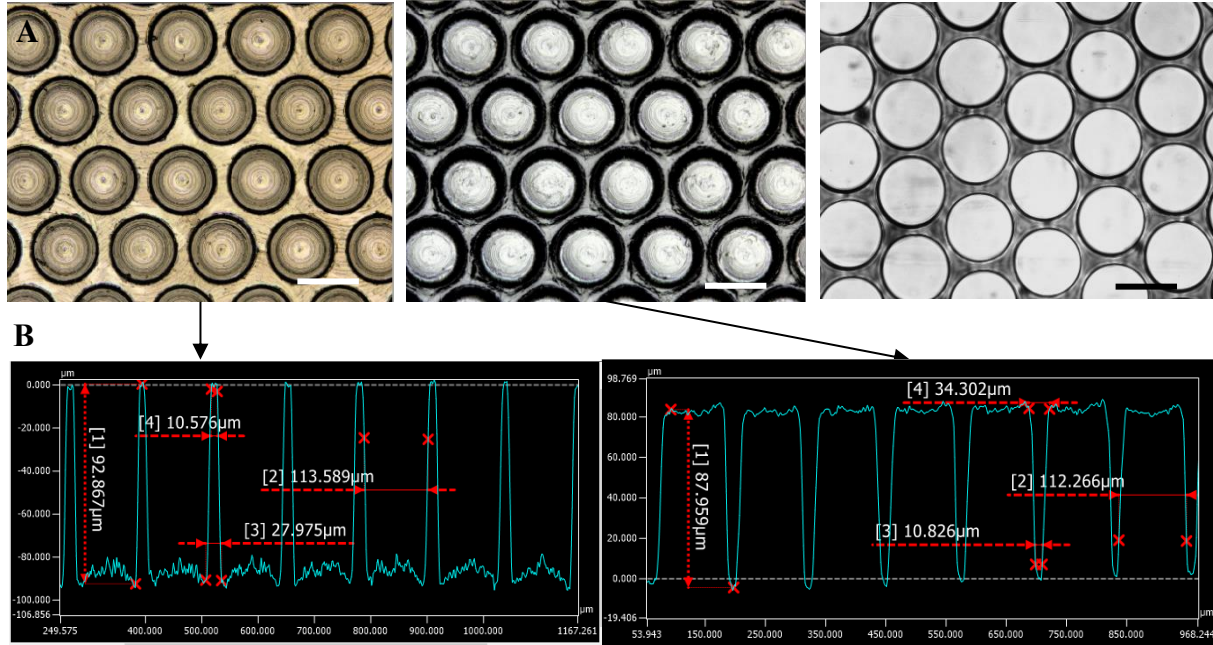
Figure 22. Fidelity assessment of the EV-MAP fabrication procedure.
(**A**) Representative images of master mold (left), embossed device before annealing (middle), and annealed device (right). Scale bar is 100 µm. (**B**) Example images of profilometry analysis performed through Multifile Analyzer software (Keyence), showing high reproducibility of dimensions between the mold and embossed device.

Table 8. Average pillar diameter and spacing of the mold and 4 devices before and after annealing.
Pillar height for annealed devices could not be measured because Keyence could not image over the coverslip or plastic bottom of the device due to the bending of the light scattering created by the surfaces. Therefore, only pillar diameter and spacing were analyzed using a custom ImageJ macro after procuring images from a Nikon Optiphot 2 Trinocular microscope. Statistical comparison of all dimensions between each step showed no significant difference ($p > 0.05$ for 95% confidence using a two-tailed t test across all data sets).

	Pillar diameter(µm)	Pillar spacing	Pillar height
Master mold	113.7 ± 1.5	23.2 ± 1.8	88.6 ± 1.4
Before annealing	112.9 ± 1.5	23 ± 2.5	88.1 ± 3
After annealing	112.3 ± 1	22 ± 2	-

2.2.1 EV-MAP recovery simulation through Monte Carlo modeling

The design of the EV-MAP was predicated on the diffusion of EVs to the microchannel walls populated with mAb. Collaborators in Dr. Soper's group designed the EV-MAP device by testing various geometries and device architectures through simulations to model the diffusive transport of an EV when hydrodynamic Poiseuille flow, diffusional dynamics, and EV-mAb binding kinetics are applied to determine the optimum device dimensions for maximum EV recovery. While COMSOL can simulate both hydrodynamic and mAb binding physics, its estimation of EV recovery required modeling diffusion through the entire bed length of 122 mm, and with this large geometry it made the simulations numerically intractable. Therefore, Monte Carlo methods were used.

Monte Carlo simulations model the probability of many different outcomes made possible due to the random nature of the variables involved. The simulations randomly selected variable values from a realistic input range to result in the most extreme or most conservative outcomes along with every possibility in between. Many trials were performed until the average results converged to a single outcome. This repeated random sampling and probabilistic view of end results make the Monte Carlo method well-suited for simulating systems with multiple degrees of freedom, making it a viable choice for modeling particle interactions in fluids.
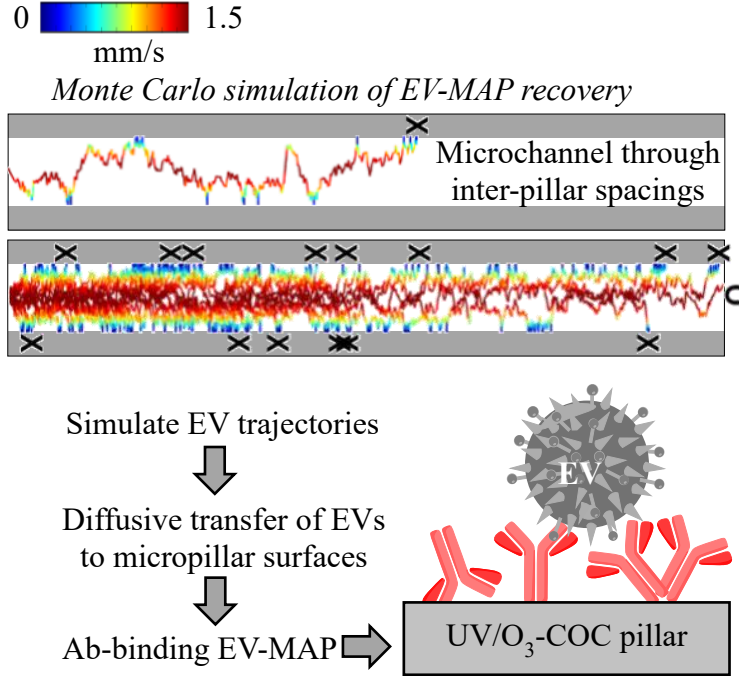
Figure 23. Example of Monte Carlo EV recovery simulation and schematic of incorporated physical dynamics. Monte Carlo simulations were used to theoretically assess the recovery of EVs from different device architectures as well as flow rates. The recovery of EVs depends on two things: the diffusive transfer of an EV to an mAb-coated micropillar surface and the probability that that EV will successfully bind to the mAb at the surface. (**A**) Example EV-MAP Monte Carlo simulation. Each line within the microchannel is associated with the path of a single EV (not to scale), where red is associated with a high velocity (1.5 mm/s) and blue is a low velocity (0 mm/s). An "X" indicates successful EV-mAb binding while "O" denotes loss of the EV through the channel. In this simulation, the channel measured 10 µm in width, with each 100 nm EV moving at V_{ave} = 1 mm/s. The 100 nm EV has a diffusion coefficient of 5 µm/s^2. The EVs traveled through an effective bed length of 35 mm, corrected for the circular pillar geometry ($\pi/2$). In this simulation, 14 EVs were successfully captured while 1 EV escaped through the channel corresponding to a 93% recovery. (**B**) Flow chart of the Monte Carlo model for EV-MAP. First, the simulation randomly sends an EV through the microchannel based on a Gaussian distribution to model diffusion dynamics and tracks their position. If an EV diffuses toward a micropillar surface, the mAb-binding kinetics determine if the EV will successfully bind. If not, the EV is continually moved through the channel. Acknowledgements to Dr. Matt Jackson of the Soper group.

The EV-MAP Monte Carlo model tracked the convective and diffusive motion of a single EV through a "straight" channel (corrected for the circular pillar geometry). The pressure-driven flow through a microchannel produces a Poiseuille flow characterized by a parabolic profile,

with EVs close to the wall experiencing a velocity close to 0 mm/s due to the no-slip condition

generated by Poiseuille flow in a microchannel (**Figure 23**) while EVs in the midline of the

channel experience a maximum velocity, or 1.5 V_{ave} (1.5 mm/s in simulation shown in **Figure

23**). Additionally, the probability of EV-mAb binding upon interaction with a modified surface is

also incorporated into the EV-MAP Monte Carlo model as not every interaction of an EV with a

channel wall will result in successful EV-mAb binding. EVs are either recovered (X in **Figure

23**) or lost (O in **Figure 23**), with the results averaged over thousands of randomly moving EVs

until converging to an average EV recovery. In the simulation shown in **Figure 23**, a 93%

recovery was achieved through the successful capture of 14 out of 15 EVs. **Figure 23** provides a

flow chart of how the EV-MAP Monte Carlo simulates an EV through the microchannel, with

the simulation first propagating EVs through the channel dependent upon both the convection

and diffusion dynamics. Then, once an EV comes into contact with a mAb-decorated surface,

mAb-binding kinetics are included in the simulation to assess whether the antigen and mAb will

successfully complex and result in the isolation of an EV.

Theory of diffusion dynamics in the Monte Carlo simulations. The dynamics employed in the

Monte Carlo model originate from the driving forces affecting EV affinity-selection. Affinity-

selection dynamics depend on two events: (1) The delivery of the EV to the mAb-immobilized

EV-MAP surface; and (2) successful binding of the mAb to the EV. Therefore, both the fluid

dynamics and chemical physics were critical in designing the EV-MAP micropillar beds. The

chemical physics incorporated in affinity-selection have previously been outlined for CTCs [98,

200] as well as diffusional models for the affinity-selection of membrane proteins [201].

However, the diffusional model used for EV-MAP simulations includes some advancements.

The delivery of EVs to the mAb-immobilized EV-MAP surfaces depends on the ability of the EV to diffuse through the plasma matrix. Hydrodynamic pumping of the EV through the device causes it to diffuse laterally and longitudinally according to Fick's Second Law of diffusion that is applied in non-steady state diffusional scenarios when the concentration of the diffusing species is a function of both time and position. Applying this law to EVs then states that for a small time increment, Δt, the probability that an EV will diffuse a distance x_D from its original position is given by a Gaussian distribution, $P(x)$:

$$P(x) = \frac{1}{\sigma\sqrt{2\pi}} e^{-\frac{x_D^2}{2\sigma^2}} \qquad (Eq.3)$$

The standard deviation of this Gaussian distribution is given by $= \sqrt{2D\Delta t}$. In accordance with Fick's second law, smaller EVs are more likely to diffuse farther over a certain time Δt due to their higher diffusion coefficient (D).

The pressure driving the fluid through the device causes the EVs to experience Poiseuille flow. In an EV-MAP microchannel with a width of W, an EV's forward velocity at a position x from the middle of the channel is approximated by:

$$V(x) = 1.5 \, V_{ave}\left(1 - \left(\frac{x}{W/2}\right)^2\right) \qquad (Eq. 4)$$

The average velocity (V_{ave}) is calculated by dividing the volumetric flow rate by the bed's cross-section. This parabolic flow profile creates a dependence on the time available for EV diffusion based on the lateral position of the EV within the channel. When an EV travels closer to a device surface, the EV forward motion slows due to the no-slip condition experienced near a microchannel wall, allowing more time for diffusion to occur. Therefore, if one EV takes a random path leading closer to the surface, it will experience a different residence time than another EV following a separate path. This variability affects EV recovery based on differing EV

71

paths and thus required many simulations of individual EVs moving in random trajectories until the results converged to an average. Incorporating the diffusive probability and Poiseuille flow-based theoretical particle velocity into the Monte Carlo model allowed testing of various bed lengths (L), inter-pillar spacing (W), and average flow velocities (V_{ave}) to optimize the design of EV-MAP for high recovery, high throughput, and high surface area to maximize EV load.

The Monte Carlo model simulated EV diffusion by changing the lateral position (X dimension) and longitudinal position (Y dimension) over finite time steps (Δt) as shown:

$$x(t) = x(t - \Delta t) + rand(P(\sigma(D, \Delta t))) \qquad \text{(Eq. 5a)}$$

$$y(t) = y(t - \Delta t) + V\big(x(t - \Delta t)\big) + rand(P(\sigma(D, \Delta t))) \qquad \text{(Eq. 5b)}$$

The EV's lateral x position changed with lateral diffusion over Δt by $rand(P(\sigma(D, \Delta t)))$, which is determined through a pseudo-random number generator that propagates the EV laterally based on a Gaussian $P(x)$ distribution with standard deviation σ due to Fick's law. The longitudinal motion is simulated in the same manner with the additional effect of Poiseuille flow included through the $V\big(x(t - \Delta t)\big)$ term.

mAb-binding dynamics in Monte Carlo simulations of EV-MAP recovery. Though the Monte Carlo model implementing both hydrodynamic flow and diffusion dynamics may simulate an EV interacting with an EV-MAP mAb-coated surface, it is not guaranteed the EV will successfully bind to the mAb. Often, multiple encounters are necessary to recover a single EV. To incorporate mAb-binding dynamics into the simulation, the Chang-Hammer model [202] was applied to describe the likelihood of surface-confined mAbs binding to passing antigens found on an EV membrane. The model approximated the amount of EVs that will bind to the surface by including: (1) mAb-antigen binding kinetics; (2) the motion of the antigen (in this case EV) and the associated residence time in proximity to the surface-restricted mAb; and (3)

the rolling distance of the EV along the surface. The Chang-Hammer model has been previously simplified [200].

When considering the rolling distance of the EV, the forward rate constant k_o defining the encounter of antigens with a surface-confined mAb is written as:

$$k_o = 2a_i V_{eff} \qquad \text{(Eq. 6)}$$

The mAb-antigen interaction radius is 2 nm (a_i) in this case[203]. V_{eff} refers to the velocity of the antigen relative to the surface, resulting in 0.47 times the rolling EV's velocity due to the opposing rotational motion of the EV surface continuing to traverse the EV forward. When an antigen encounters a surface-confined mAb, the probability that they will complex (P) depends on both the mAb's binding kinetics, k_{in}, and the duration of the encounter, $\tau = 8a_i/3\pi V_{eff}$:

$$P = \frac{k_{in}}{k_{in}+1/\tau} \qquad \text{(Eq. 7)}$$

k_{in} is based on the Ab's specific kinetics and thereby treated as a constant not affected by the motion of the antigen. However, the duration of the interaction is dependent upon the interaction radius and effective velocity. An increase in EV linear velocity causes the encounter duration to decrease creating less time for the mAb and antigen to complex and consequently reducing binding probability. Therefore, the antigen's forward rate constant (k_o) and the binding probability (P) are inversely related to one another in yielding an effective forward rate constant, k_f is:

$$k_f = k_o P \qquad \text{(Eq. 8)}$$

This k_f represents the probability that the reaction will occur. Lastly, because EV-MAP is concerned with adhesion of an EV, which could harbor one or several surface antigens, both the forward rate constant, k_f, and the antigen surface density C_∞ determine the overall adhesion rate constant (k_{ad}) of the EV to the surface:

73

$$k_{ad} = k_f C_\infty \qquad \text{(Eq. 9)}$$

In summary, k_{ad} accounts for the EV's antigen expression and velocity of those antigens, based

on how often the antigens encounter mAbs and how likely a binding event is given the duration

of antigen-mAb interaction and the mAb's binding kinetics. This resulting rate of EV adhesion

relates to an experimental system when considering an EV moving along a mAb-coated surface

at a linear velocity (V) for some distance (L). In this relevant scenario, the percent of EVs that

will bind is determined through:

$$\%_{bound} = 1 - 1/e^{\frac{k_{ad}L}{V}} \qquad \text{(Eq. 10)}$$

It is apparent from Eq. 10 that minimizing the linear velocity and maximizing the length

at which the EV interacts with the surface will improve EV recovery. EVs have a high diffusion

coefficient due to their relatively small size, with the dynamics of an EV rolling along a

micropillar surface described by a Peclet number <1 due to the negligible convection

experienced at the channel side walls because of the no-slip condition in Poiseuille flow. The

motion of the EV at this location is therefore almost entirely dependent on the diffusion, which is

challenging to externally control as it is a random process. Therefore, manipulating the lateral

diffusion and length of EV-micropillar interaction proves challenging. Furthermore, because of

the no-slip condition limiting the surface flow velocities to approximately zero, decreasing the

bulk flow rate or flow velocity will provide little effect to the linear velocity in Eq. 10. Based on

these limitations, it is most practical to manipulate the chances with which the EV has to interact

with the surface than to manipulate each moment of interaction. Therefore, decreasing inter-

pillar spacing or increasing bed length would allow for more time and shorter diffusional

distances to maximize the amount of interactions a single EV could have with the Ab-coated

surface in hopes that one interaction would create a probability high enough to result in successful binding.

Implementation of physical dynamics into Monte Carlo model. The fluid dynamics explained above were incorporated into Monte Carlo simulations for modeling EV recovery. The curving flow path along a bed with length L_{bed} was approximated as a straight microchannel with a width W equal to the interpillar spacing and length $L = L_{bed}C$. C is a correction factor to elongate the flow path due to the pillar's circular geometry when constraining it to a straight channel, ($C = \pi/2 \approx 1.57$) [201]. EVs started at 11 possible positions at the beginning of the pseudo-channel, and their positions through the channel were propagated by Eqs. 5. If an EV encountered the channel surface ($x = \pm W/2$), the EV moved forward a certain distance dictated by multiplying the EV's forward velocity $V(x)$ (Eq.4) with the simulation's time step Δt. This rolling distance was then used to calculate the probability of binding from Eqs. 6-10, with this probability turned into an actionable decision (either bound or not bound) by using a pseudo-random number generator under a uniform distribution between 0 and 1. If the random number proved less than or equal to Eq. 10's binding probability, the EV was captured on the device. For example, if the interaction event correlated to a 10% binding probability, then 10% of the pseudo random numbers could result in successful complexing making any number less than or equal to 0.1 count as a successful binding event. If this did not occur, the EV was further moved through the channel via Eqs. 5.

Each EV's path was considered a binary event as either recovered or lost, with thousands of EVs tracked until the simulated recovery converged. This convergence was met only if: (1) A <0.01% change in the average recovery was observed when additional EVs were tracked through a single simulation; (2) a <10% standard deviation occurred for five repetitive simulations run

under the same channel architecture; and (3) a difference of <1% was observed from the average solution of five simulations after halving the Δt increment, otherwise the simulations would be repeated after halving Δt again (**Figure 24**). The decreasing of time steps was important to track the EV realistically through slight differences in particle path caused by Brownian motion. As can be seen from **Figure 24**, a large time step drastically effects recovery results with an 80% recovery achieved by 2 ms between EV motion tracks vs. a <60% recovery resulting from a 0.16 ms time step. Furthermore, the more variable distribution observed with less EVs tracked through the channel highlights the need for more EVs to be simulated in order to create highly reproducible EV recoveries for fixed microchannel conditions.
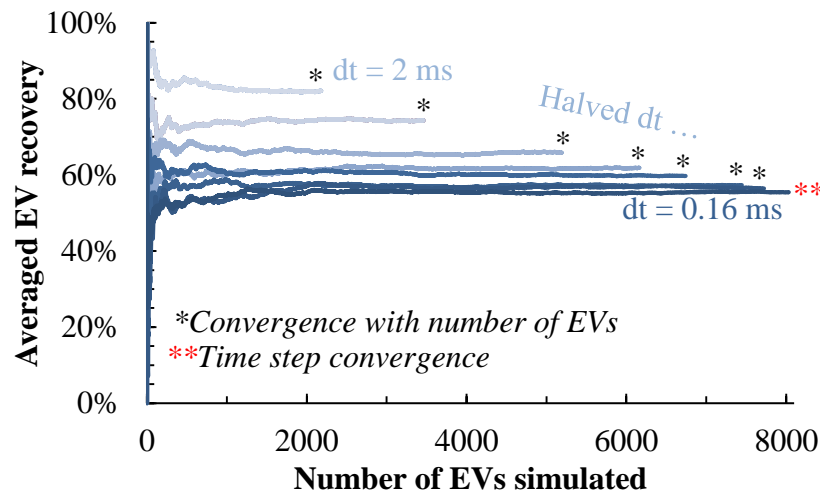

Figure 24. Example showing convergence of simulations to an average EV recovery. EVs are continuously sent through the microchannel in a single simulation, with the addition of more EVs only stopping once the average recovery converges to <0.01% difference than the average recovery resulting before the addition of another EV(*). After converging based on the number of EVs, a time step convergence criterion is applied where Δt is halved until the averaged recovery of five simulations converges to <1% error change (**), with these simulations run under the same channel geometry and flow conditions. This criterion was important in accurately tracking small position changes of the EV caused by Brownian motion. A third convergence criterion which is not shown above required the standard deviation of five sequential simulations performed with the same parameters and conditions to be <10%. The results shown were simulated for a 100 nm EV with diffusion coefficient, D = 5 μm^2/s, starting in the center of the channel, with effective bed length accounting for circular pillar geometry L = 35 mm and W = 10 μm, and infused at an average velocity of 1 mm/s. Acknowledgements to Dr. Joshua Matt Jackson of the Soper research group.

The dynamics applied in the EV-MAP Monte Carlo simulations were validated through subsequent addition of various forces affecting EV-Ab binding. Initially, all recovery effects were removed and EVs allowed to move freely in solution only propagated through random Brownian motion with no wall constraints. In this scenario, Fick's Second Law (Eq. 1) is valid and the results from the Monte Carlo simulation match well with a Gaussian distribution produced from Eq. 3 (**Figure 25**). Wall constraints were then introduced into the model along with convective flow driven hydrodynamically, only negating the mAb-binding dynamics so that any surface interaction led to EV recovery. In this simulation, 64% of EVs were recovered showing a high variability in spatial distribution even when only considering the lateral direction (represented by blue bars in **Figure 25**). This is because Fick's law is rendered invalid when the EV concentration is no longer constant due to the addition of favorable EV-affinity selection to the channel surfaces (represented by -W/2 and W/2 in **Figure 25**). All subsequent simulations used EV sizes, diffusional coefficients, and surface densities found in **Table 9** for estimating EV-MAP recovery *in silico*.
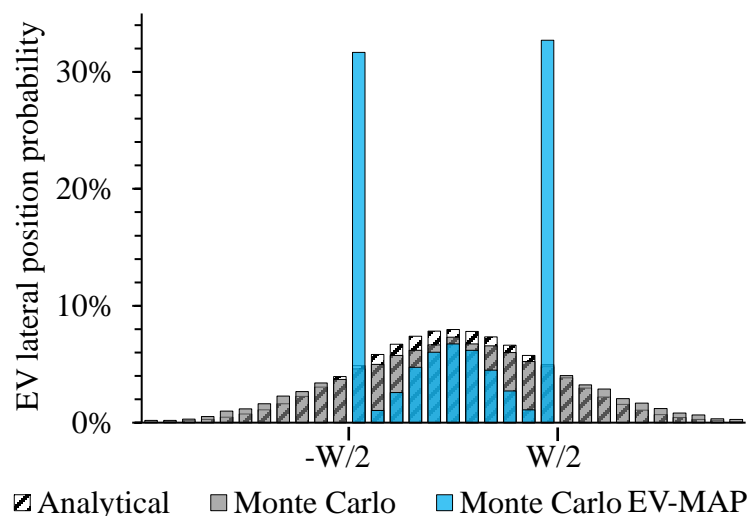
Figure 25. Validation of Monte Carlo model with sequential addition of physical dynamics principles.

EVs were diffused laterally amidst Poiseuille flow, with the lateral position tracked based on the channel's width (W). The x axis of the graph correlates to the lateral position of an EV when reaching the end of the channel. The y axis then shows the probability that EVs from the simulation will end in these lateral positions, with -W/2 and W/2 referring to the walls of the channel and therefore showing the recovered EVs. Simulations disregarding affinity-binding dynamics, wall constraints, and Poiseuille flow thereby only considering an EV's natural diffusion path (grey bars) agreed with the analytical solution to Fick's Second Law (hashed bars). However, when constraints of the microchannel and Poiseuille flow were applied (blue bars), the EV spatial distribution is no longer Gaussian. These conditions allow for the affinity capture of EVs to the channel walls, creating the large increase of EVs positions at -W/2 and W/2. The spatial distribution even changes drastically within the channel's width. This is due to the invalidity of Fick's law as EV concentration fluctuates. These results were computed for a D = 5 μm^2/s, effective length (incorporating circular correction factor) L = 4 mm, W = 10 μm, V_{ave} = 1 mm/s. Chang-Hammer dynamics were not applied, making all EV-mAb interactions successful. Acknowledgements to Dr. Matt Jackson of the Soper research group.

The Ab-binding Chang-Hammer dynamics (with parameters used for Monte Carlo simulations shown in **Table 9**) were then applied to the Monte Carlo simulation to include a probability with every EV that came into contact with a mAb producing a substantially lower recovery (16%) for a simulated small 10 µm inter-pillar spacing but short effective bed length of 4 mm (taking into account the correction factor for circular pillar geometry) and average velocity of 1 mm/s. The shorter bed length decreased the overall time available for lateral diffusion

therefore contributing to the low recovery. This significant decrease in recovery highlights the importance of including mAb-binding probability in the EV-MAP model, otherwise unrealistically high recoveries could result due to the incorrect assumption that all mAb-EV interaction events end in successful EV binding.

Table 9. Parameters used for Chang-Hammer dynamics (Eqs. 6-10) in Monte Carlo three bed EV-MAP simulations.

Property	Value	Reference
EV diameter	100 nm	-
Viscosity	8.9×10^{-4} Pa·s	-
Diffusion coefficient (D)	5 μm^2/s	-
Minimum EpCAM surface density (C_∞)	12.31 μm^{-2}	[204]
Anti-EpCAM binding kinetics (k_{in})	2.5 $M^{-1}s^{-1}$	[205]
Ab-antigen encounter radius (a_i)	2 nm	[202, 203]

After validating the model, EV-MAP recoveries under various inter-pillar spacings and volumetric flow rates (**Figure 26**) were assessed to determine the optimum device architecture and experimental conditions. 80% recovery was observed at a flow rate of 2.1 µL/min, with this high recovery being the reason it was chosen as the infusion flow rate for the samples used in this study as well as the practicality of allowing the sample processing to be performed in a single day. Interestingly, the simulated recoveries at various flow rates did not depend on the inter-pillar spacing because increased diffusional distances were counteracted by decreased linear velocities to create a constant flow rate. This was important as the fabricated devices had a gradient of pillar spacing between 10 to 20 µm due to the draft angle caused by the master mold milling procedure.

Predicted recovery for EV-MAP prototype
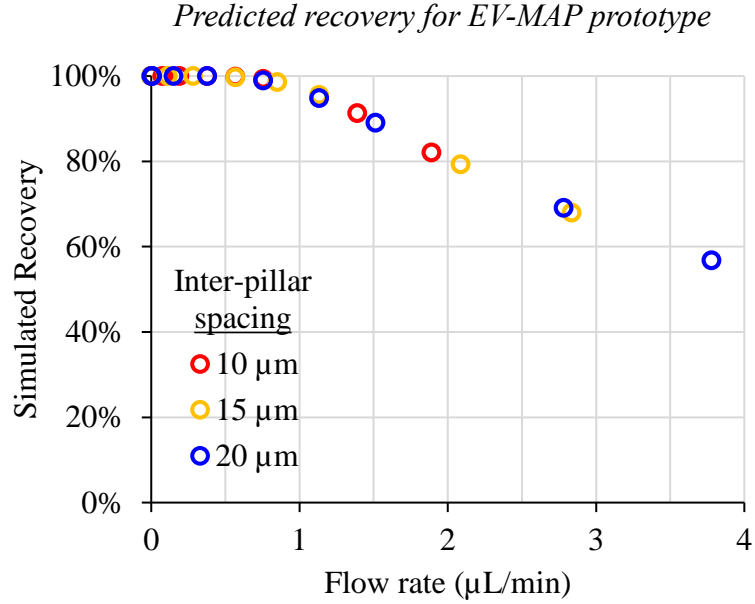
Figure 26. EV recovery results from the three-bed EV-MAP Monte Carlo simulations.

Various interpillar spacings (10,15, and 20 μm) and volumetric flow rates were tested through the Monte Carlo model to optimize the device design by maximizing recovery. All simulations were run using the full bed length of 122 mm, corrected for the circular geometry of the micropillars ($\pi/2$). 100 nm EVs with a diffusion coefficient of 5 µm/s^2 traveled through the device. Acknowledgements to Dr. Joshua Matt Jackson of the Soper research group.

Evaluation of Shear stresses in EV-MAP devices. It was important to investigate the shear stresses placed upon EVs within the EV-MAP device to ensure the biological particles would not be lysed or damaged, as well the shear forces not release the EVs from the surface to which they were bound. COMSOL Multiphysics simulations derived the shear stress profiles (**Figure 27**) from the parameters outlined in **Table 10**, with results showing a shear stress of 3.1 dynes/cm^2 at the pillar walls under the highest linear velocity of 3.7 mm/s, with this shear stress proving much lower than the adhesion force of an EV to the surface which amounts to 150,000 dynes/cm^2 (See Section 2.2.2) thereby ensuring the flow rate alone would not shear EVs from the surface.

**3D velocity cross-sections**　　　　　　　　　　　　　　　　　**Shear stress**
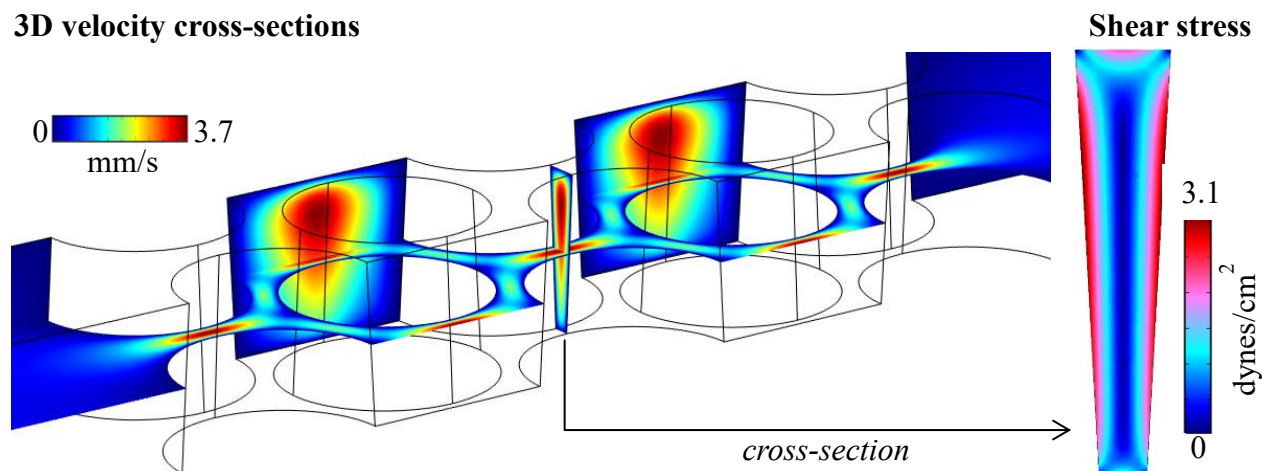
Figure 27. Evaluation of Shear stress applied between two micropillars.

3-dimensional velocity cross-section and shear stress profiles between two adjacent micropillars resulting from COMSOL Multiphysics simulations. Symmetry constraints were employed along two sides of the simulation to achieve high element quality by reducing the number of elements required (**Table 10**) to decrease computational cost. Acknowledgements to Dr. Matt Jackson of the Soper Research group.

Table 10. Parameters for COMSOL simulations of laminar flow dynamics to assess EV-MAP shear stresses. 3-dimensional laminar flow dynamics were applied to the EV-MAP prototype to simulate shear stresses imparted on the EVs in a microfluidic channel. The parameters for geometry were empirically derived through confocal, laser-scanning profilometry measurements of the EV-MAP device.

Parameter	Value
Physics	Laminar flow, stationary
Viscosity	0.0345 Pa s
Density	1.055 g/mL
Inlet	2.1 µL/min (0.21 mm/s)
Outlet	0 Pa
Pillar height	90 µm
Pillar diameter	110-120 µm
Inter-pillar spacing	10-20 µm
Draft angle	4.6°
Program	COMSOL 5.2a
Number of elements	11,528,872
Average element quality	0.6754
Solver	GMRES
Tolerance	10^{-3}

2.2.2 Depletion of EVs from FBS in culture media: Depletion efficiency and protein analysis.

FBS-derived EVs create significant background to overcome when analyzing cell-specific EVs shed in culture media. To decrease this background signal, ultracentrifugation at 100,000g removed bovine-derived EVs from FBS [206]. A single ultracentrifugation step for 6 h pelleted EVs from 60 mL of stock FBS, with two sequential ultracentrifugation passes of 3 h performed on the respective supernatants to detect and quantify any remaining EVs after initial depletion. The TRNA size profile and concentrations from the residual EV pellets were then compared to the TRNA extracted from the pellet after initial 6 h ultracentrifugation of the stock FBS to determine depletion efficiency. All TRNA fractions maintained similar size distributions ranging from 200 – 4000 nt as visible through HS RNA Tape (**Figure 28A**), with the depletion of EVs visualized through TEM images after 6 h ultracentrifugation on the supernatant (designated by black arrow in **Figure 28B**). The TRNA extracted decreased from 390 ng in 60 mL of stock FBS to 17 ng per 60 mL in EV-depleted stock FBS (**Table 11**). A 96% depletion efficiency was achieved after 6 h of ultracentrifugation.

For the duration of this study, all cell lines were cultured with diluted 10% EV-depleted FBS creating a background of 2.8 pg TRNA/mL of media. These depletion results coincided well with the literature [206]. However, when employing extended ultracentrifugation (18-22 h, 100,000g) for EV depletion, a sedimentation gradient of proteins was observed. Additional depletion of proteins along with EVs could decrease the growth of cells within the culture media. Therefore, the protein gradient was analyzed for total protein content through protein quantification of 10 mL fractions from the 60 mL of FBS after ultracentrifugation using the

EZQ™ Protein Quantification Kit (Invitrogen). The protein size distribution in each fraction was also assessed using a non-reducing SDS-PAGE with Coomassie R250 staining.
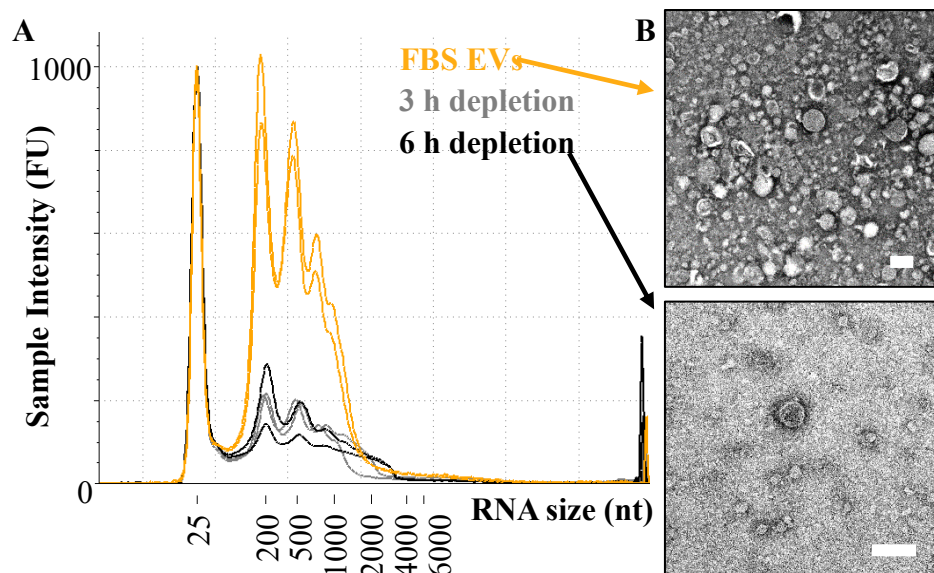

Figure 28. TRNA size distribution and TEM images of residual EVs after 6 h ultracentrifugation of FBS. Stock FBS was ultracentrifuged at 100,000g for 6 h (yellow lines) with the resulting pellet lysed for TRNA extraction. The supernatant or EV-depleted FBS was then sequentially ultracentrifuged for two 3 h steps, with the TRNA extracted from the pellet after 3 h (grey lines) and 6 h (black lines). All procedures were run in duplicate. (**A**) TRNA size distribution and relative abundance. TRNA was analyzed using HS RNA tape, with the marker band denoted at 25 nt. Residual EV TRNA was still present in undiluted FBS after 3 h and 6 h of ultracentrifugation. (**B**) TEM images of EVs from the initial 6 h ultracentrifugation performed on stock FBS and residual EVs remaining in the EV-depleted supernatant after another 6 h ultracentrifugation, showing a reduction in EVs. Scale bars are 200 nm.

Table 11. TRNA yield from ultracentrifuged stock FBS and the residual EVs.
TRNA mass resulting from the samples shown in **Figure** 28, with 60 mL of stock FBS and subsequent EV-depleted supernatants after 3 and 6 h ultracentrifugation steps analyzed. TRNA concentration was measured using the HS RNA Tape, then multiplied by the total TRNA elution volume to result in ng of TRNA from 60 mL FBS. The mass shown only includes TRNA <2,000 nt.

TRNA source	ng TRNA per 60 mL	TRNA size range
FBS EVs (6 h, 100,000 g)	390.1 ±14.1	<2,000 nt
Residual FBS EVs (3h, 100,000 g)	17.7 ±3.9	<2,000 nt
Residual FBS EVs (6h, 100,000 g)	16.8 ±1.5	<2,000 nt

For protein size characterization, the samples were loaded into the 10% polyacrylamide gel (Mini-PROTEAN® TGX™ Precast Protein Gel, Bio-Rad) with Laemmli buffer (Bio-Rad), heated to 95 ° C for 5 min, then run through the gel at 200 V in Tris/Glycine/SDS buffer (Bio-Rad). The gels were prefixed with 10% acetic acid for 30 min, stained with 3 g/L Coommassie R250 in 10% acetic acid for 1 h, with the stain removed in 7.5% acetic acid (4 h in orbital shaker). Images of the gel were taken with a Kodak Gel Logic 200 system. 5 µg bovine serum albumin (BSA) was used as a protein sizing control in the gels.
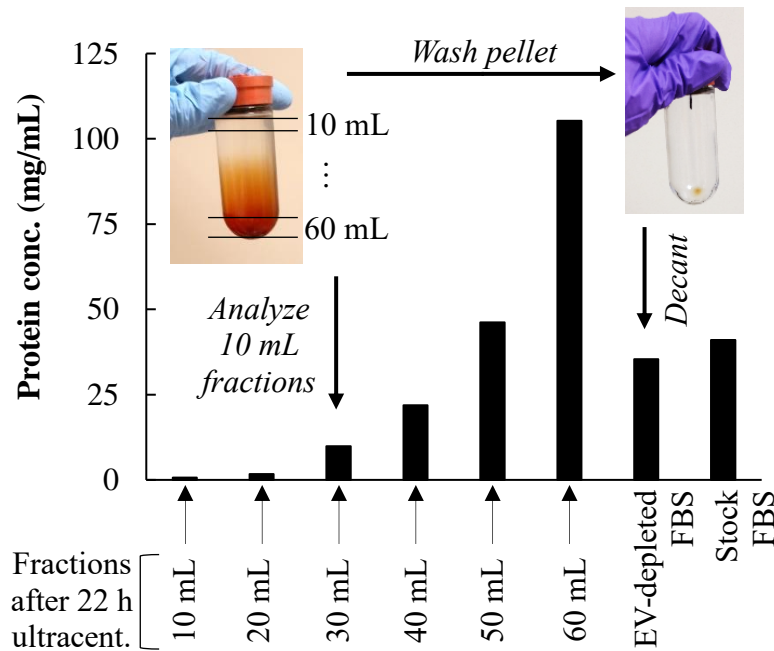
Figure 29. Analysis of protein content after extended (22 h) ultracentrifugation of stock FBS
Protein content analyzed from 10 mL fractions of 60 mL of stock FBS after extended ultracentrifugation for 22 h at 100,000g showed a gradient of proteins (top left picture) suggesting higher density proteins may sediment toward the bottom of the flask. Protein was quantified using the EZQ™ quantification kit (Invitrogen) which uses protein blotting onto a paper support and measures fluorescence intensity to compare unknown samples to a standard calibration curve of ovalbumin. Protein content of both the 100% stock FBS and final EV-depleted FBS after mixing and decanting the supernatant are also shown in the graph to highlight the preservation of most proteins through this decanting method.
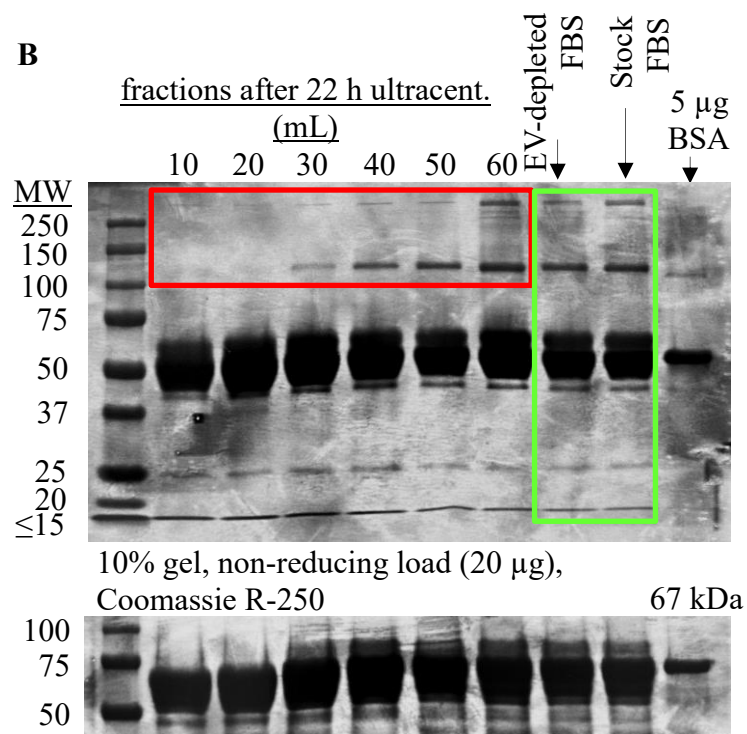
**Figure 30**. Fractional analysis of protein sizes after extended (18-22 h) ultracentrifugation of stock FBS. The fractions from **Figure 29** were also analyzed through SDS-PAGE with Coomassie R250 staining to assess the size distribution of proteins found in all fractions of the ultracentrifuged 60 mL stock FBS. The red box outlines an increasing concentration of higher molecular weight proteins toward the bottom of the flask (in fractions 30-60, respectively) while the green box shows the preservation of these higher molecular weight proteins through mixing and decanting the supernatant after 18-22 h of ultracentrifugation. When the gel was run under non-reducing conditions, the band differed from the known molecular weight of BSA. Therefore, the samples and control were reduced with 5% 2-mercaptoethanol (Bio-Rad) before running on a second gel. This gel showed the BSA control with appropriate protein sizing and is provided here under the original gel.

Analysis of the protein content showed an increased protein concentration closer to the bottom of the centrifugation tube (**Figure 29**) or in the 60 mL fraction. Through both SDS-PAGE (**Figure 30**) and protein content analysis it was proven that indeed proteins sedimented into the pellet after prolonged ultracentrifugation, with these proteins having high molecular weights (**Figure 30**). However, decanting and mixing of the supernatant after ultracentrifugation preserved 91% of the total protein content found in the FBS stock (**Figure 29**) and maintained the higher molecular weight proteins within the EV-depleted FBS (**Figure 30**). Therefore, this

step was included in EV-depletion of FBS for cell culture using an 18 h ultracentrifugation step to maintain the required protein content for optimum cell growth.

2.2.4 Effects of differential ultracentrifugation on the heterogeneity of EV populations.

Differential ultracentrifugation serves as the gold standard for EV isolation, though limitations are associated with the procedure [207, 208]. Differential ultracentrifugation often results in lower EV yields due to loss of EVs either through premature sedimentation from EV aggregation or EVs remaining in the supernatant [209-211]. To investigate the EV populations recovered through differential ultracentrifugation as well as potential loss of EVs, EVs were harvested from 60 mL of MCF7 and Hs578T breast cancer cell media conditioned in 10% EV-depleted FBS through the differential ultracentrifugation protocol outlined in Théry *et al.* [149] (protocol also outlined in the Benchtop isolation section of Chapter 2. Introduction): 300g and 2,000g to remove cells, debris; and apoptotic bodies 10,000g to deplete vesicles >150 nm; and 100,000g for pelleting the remaining EVs, then washing with PBS (pH = 7.2). Pellets formed after 10,000g centrifugation and 100,000g ultracentrifugation were lysed with the TRNA extracted, purified, and subsequently analyzed using HS RNA Tape (Agilent Technologies).

The TRNA size distribution (between 200-1000 nt with a majority of TRNA between 200-500 nt, **Figure 31**) was consistent with TRNA sizes often found in EVs [133]. Three to four µg of TRNA was isolated from 10^6 cells to compare the contrasting cellular TRNA profile showing high abundance of 28S/18S rRNA visible (**Figure 31**) to the absence of such rRNA in the EV TRNA fraction**.** TRNA was observed in the 10,000g fractions (~60 pg/mL of medium) (**Table 11**)**,** suggesting the loss of larger EVs such as microvesicles to this initial 10,000g step. However, this TRNA concentration is small in comparison to the TRNA yield from EVs pelleted

at 100,000g, collecting 880 pg/mL MCF7 media and 545 pg/mL Hs578T media, respectively (**Table 11**).
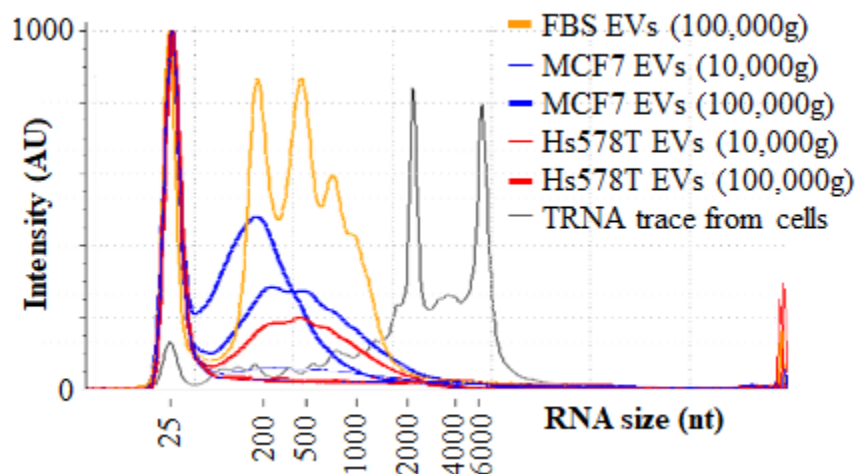

Figure 31. TRNA sizing and abundance from EV pellets collected during differential ultracentrifugation. TRNA size distribution of EVs isolated from 60 mL of MCF7 or Hs578T conditioned media through differential ultracentrifugation (protocol outlined in Théry *et al.* [145] and discussed above in the text). EV pellets after 10,000g and 100,000g steps were lysed for EV TRNA, with TRNA extracted and the trace shown from cells for comparison. The EV TRNA showed no 18s or 28s peaks as opposed to the 18s and 28s peaks clearly visible in the cell TRNA . Further, the FBS EV TRNA trace from ultracentrifugation showed a much higher level of TRNA compared to the conditioned media EVs. RNA was assessed using HS RNA Tape. The peak at 25 nt represents the marker band. 10,000g pellets are shown by the light-weight lines toward the bottom of the graph, correlating to little TRNA content compared to the 100,000g fractions.

Table 12. TRNA concentrations from cell line EV pellets collected during differential ultracentrifugation. TRNA concentrations for the samples shown in **Figure 31**. The blank media correlates to the FBS EV fraction above, showing the background TRNA content.

TRNA source	Spin speed (×g)	pg TRNA per mL
Blank media	100,000	28.3 ±3.33
MCF-7	10,000	58.3 ±25
	100,000	880 ±31.7
Hs578T	10,000	60 ±28.3
	100,000	545
MCF-7 lysate	10^6 cells	66,667
Hs578T lysate	10^6 cells	61,667

TEM images were taken of the 100,000g pelleted fractions to qualitatively characterize the EV subpopulations isolated (**Figure 32**)**,** by observing the morphology and manually measuring the diameter of each EV observed in the images to discern the relative size distribution for both the 100,000g pellets and the corresponding supernatants. A similar EV size range for MCF7 (25-83 nm) and Hs578T (20-80 nm) EVs was observed. However, the median size for MCF7 EVs shifted slightly higher to 51 nm vs. 37 nm for Hs578T. Analysis of the ultracentrifugation supernatant after 100,000g pelleting showed the presence of EVs <30 nm that were not isolated by ultracentrifugation (**Figure 32**, white bars), suggesting that a subpopulation of smaller EVs were lost during the ultracentrifugation step.

These EVs may remain in the supernatant due to a difference in density causing them to sediment slower than other higher density EVs. An EV's density depends on their cargo which varies greatly among each individual EV based on the cell of origin. This loss of EVs to the supernatant has been proven before by a group who performed western blotting on the supernatant incurred after differential ultracentrifugation to analyze the presence of EVs. They found 40% of total vesicular proteins detected through EV markers to reside in the supernatant, even after 200,000g ultracentrifugation [209]. Overall, both microvesicles and even small exosomes were found to be lost during differential ultracentrifugation, highlighting a need for improved isolation methods.
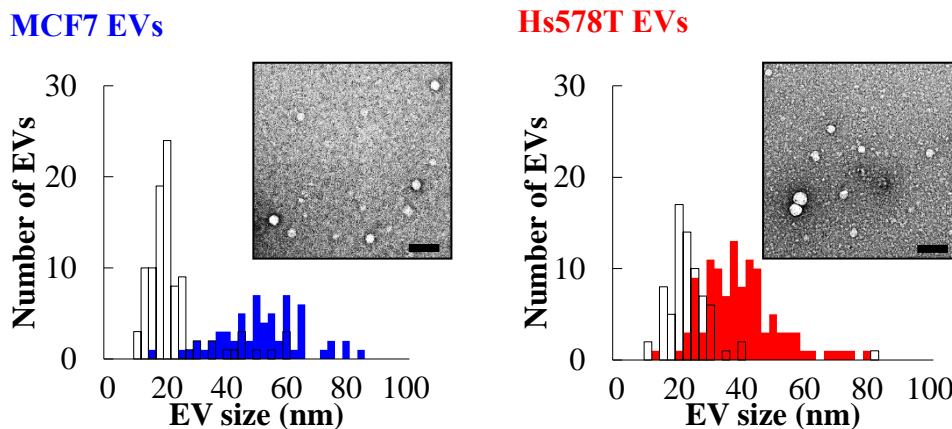
Figure 32. Size of cell line EVs from 100,000g pellets and supernatants after differential ultracentrifugation. TEM imaging of EV fractions from MCF7 and Hs578T conditioned media after differential ultracentrifugation (protocol described above in the text) and resuspension of EV pellet in PBS. The size distribution was determined through manual measurements of the EVs found in several TEM images, with example TEM images shown. White bars show the size distribution of EVs still present in the supernatant after differential ultracentrifugation as the supernatant was also subjected to TEM imaging. Scale bars set at 100 nm.

2.2.5 EV-MAP assay optimization

Proteolytic digestion for release of EVs from EV-MAP surfaces. NTA and TEM are two of the most common analytical tools used for quantifying EVs and qualitatively verifying their presence based on morphology, respectively. Methods for releasing EVs from microfluidic devices for downstream processing must not damage the EVs while also providing efficient cleavage of bonds holding the EVs to the surface. Due to the small size of EVs and high strength of the mAb-antigen bonds as well as the covalent attachment of the mAb to the microfluidic surface, manipulation of fluid shear forces cannot effectively remove EVs from the surface [95]. A single mAb-antigen bond (1.2 x 10^{-5} dynes [212]) securing a 100 nm EV would require 150,000 dynes/cm^2 for physical removal from the surface. As shown previously through the shear stress COMSOL simulations (see **Figure 27**), a flow velocity of 2.1 µL/min only delivers 3.1 dynes/cm^2 to the pillar surface. Therefore, chemically disrupting the mAb-antigen complex or

degrading the bond attaching the mAb to the surface of the microfluidic served as the most practical approach for EV release after affinity selection.

One common strategy for Ab-antigen cleavage utilizes a proteolytic enzyme to digest the bonds forming the complex. Trypsin is a common proteolytic enzyme that has shown high efficiency for releasing CTCs from mAb-modified microfluidic devices [95]. Though it has been used frequently in CTC microfluidic removal, trypsin has yet to be applied for mAb-antigen digestion of EVs. Trypsin only digests lysine and arginine residues, proving sufficient for CTCs ranging in size from 12-25 μm [95], as the fluid force within the microfluidic aids in the cell removal negating the need for every Ab bond to be cleaved. However, with EVs ranging from 10 to 400 times smaller in size, complete digestion of all residues binding the Ab to the antigen is critical.

Proteinase K has been employed for efficient digestion due to its more stringent cleavage of all types of peptide bonds [162, 213]. The use of this stringent enzyme is predicated on the enhanced stability of EVs and their resistance to protease digestion. However, it is important to note that any use of a proteolytic enzyme will concurrently digest membrane proteins, which may be of interest to analyze in certain downstream applications such as EV protein quantification. Herein, the integrity of EVs was assessed after proteolytic digestion and an additional sonication step used to mechanically loosen any EVs still stuck to the surface.
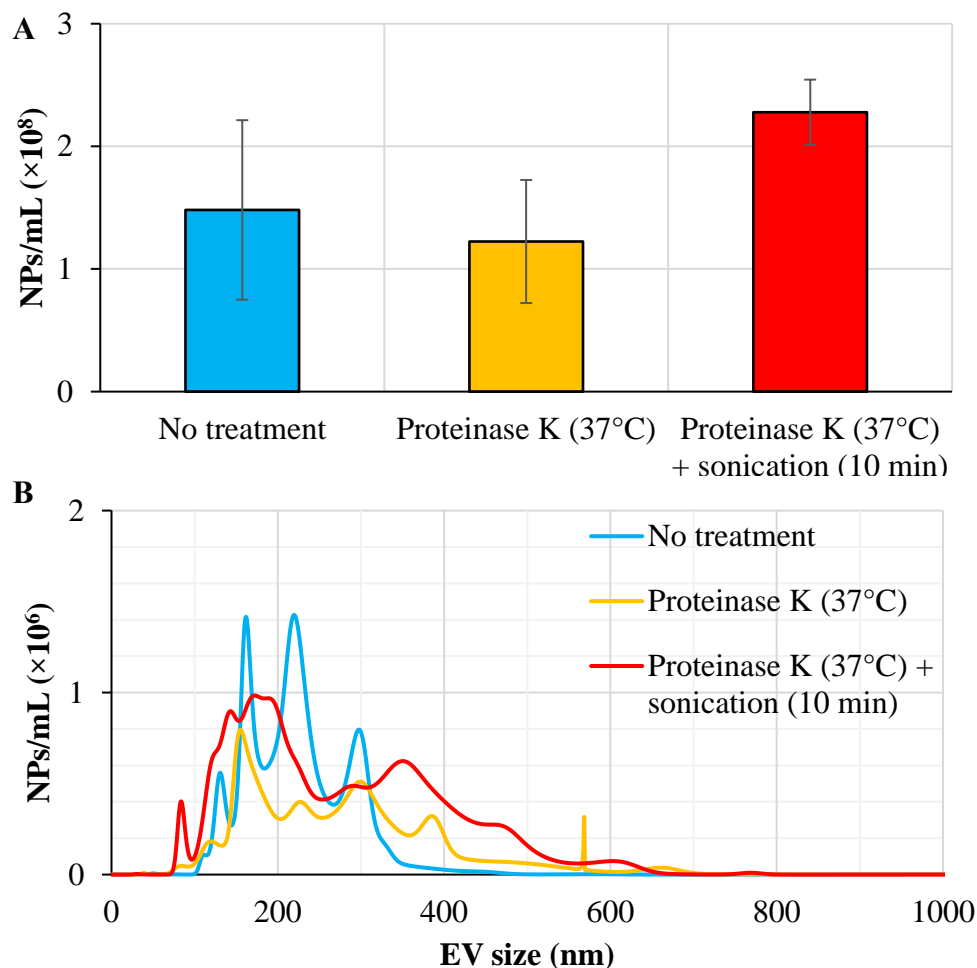
Figure 33. Investigation of SKBR3 EV integrity after proteolytic release and sonication.
(**A**) Concentration and (**B**) size distribution results from NTA data for SKBR3 EVs harvested by differential ultracentrifugation then subjected to either 30 min 0.2% proteinase K digestion alone or a combination of 0.2% proteinase K digestion and 10 min sonication. A sample of EVs was left untreated as a control to investigate the effects of the release procedure on the integrity of EVs. Error bars represent 5 separate NTA measurements of a single sample with $p > 0.05$ between the treatments and control (unpaired, two-tailed t test).

EVs were harvested from the breast cancer cell line SKBR3 through differential ultracentrifugation. The SKBR3 EVs were digested with 0.2% w/v proteinase K (from 100 mg/mL dissolved in 50% glycerol with PBS) at 37 °C for 30 min followed by 10 min of sonication. Three conditions were tested: (1) EVs with no treatment (PBS control); (2) proteinase K digestion; and (3) a combination of proteinase K treatment with sonication. The samples were taken for NTA to discern any concentration or sizing differences observed between the samples

(**Figure 33A, B**). No condition resulted in any significant change from the control (p = 0.5367 and p = 0.0705 from an unpaired, two-tailed t test) when comparing to proteinase K treatment with or without sonication, respectively. The two proteinase K treatment samples showed a widening in EV size distribution (**Figure 33B**), ranging from ~100 – 500 nm as opposed to the shorter 100 – 250 nm range observed in the PBS control. However, the average size still converges around 200 – 250 nm regardless of the presence of proteinase K treatment. Furthermore, the proteinase K treatment or sonication does not seem to cause EV shrinkage because the size range does not expand toward the lower end of the spectrum. Overall, the proteinase K proved to maintain EV integrity by not lysing EVs shown by no drastic decrease in the concentration achieved. The treatment also showed little difference in the structure of EVs, still maintaining the same ~ 250 nm average. Proteinase K therefore may be used for release of EVs from surface capture reagents while keeping their membranes intact.

To determine the efficiency of the proteinase K treatment, EVs were released from EV-MAP devices (n = 12) through sequential steps after infusing 500 µL donor plasma. The first step comprised of a PBS control that was subjected to 30 min incubation at 37°C. The samples were then proteolytically digested using 0.05% trypsin in 0.53 mM EDTA. Trypsin was included as a well-established release method for mAb-antigen cleavage of biological particles. Next, proteinase K was used to digest mAb-antigen complexes at a concentration of 0.2% w/v in glycerol and PBS. A second proteinase K step released any remaining EVs to provide a reference point for efficiency calculations. All steps included 10 min sonication after identical incubation times and temperatures, with EVs released in PBS for NTA (**Figure 34A**). To determine the

release efficiency, EV aliquots were referenced to the steps both before and after through the

following equation:

$$\frac{EVs\ released\ in\ step}{EVs\ on\ chip} = \frac{EVs\ released\ in\ step}{EVs\ released\ in\ step+subsequent\ steps} \qquad \text{(Eq. 10)}$$
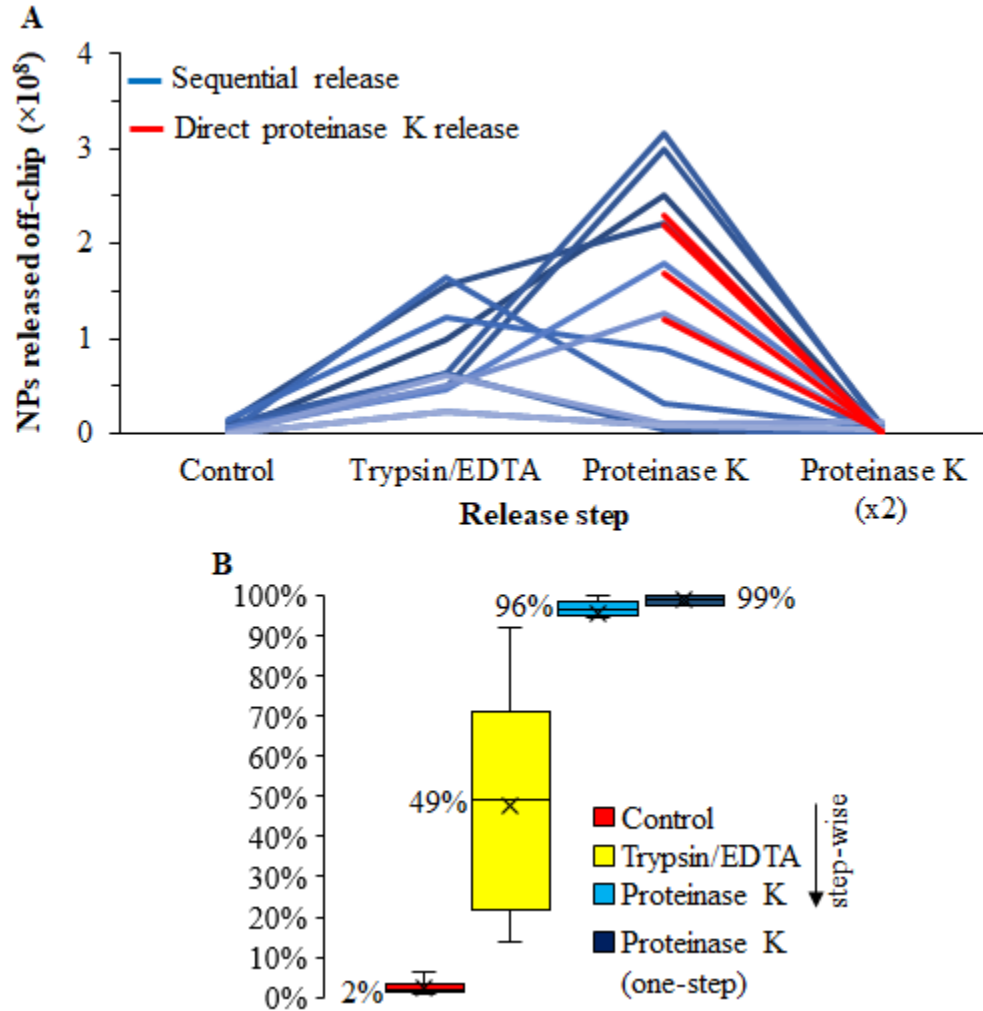
Figure 34. Release efficiency determined by NTA concentration after sequential steps of proteolytic digestion. (**A**) NTA concentration results of nanoparticles (NPs) released off-chip after sequential steps (shown blue, N = 12) using PBS, 0.5% trypsin with 0.53 mM EDTA, 0.2% proteinase K in PBS, and a second proteinase K digestion to serve as a final reference step for measuring release efficiency. A 10 min sonication step followed every sequential proteolytic digestion by 30 min incubation at 37 °C, including the initial PBS control incubation. The red lines represent NTA measured NPs released using a single proteinase K digestion step followed by a second proteinase K digestion as a reference for release efficiency (N = 4). (**B**) Box plots showing release efficiency based on the NP data shown in (**A**) and calculated using Eq. 10. A release efficiency of 99 ± 1% was achieved from a single proteinase K digestion (30 min, 37 °C) followed by 10 min sonication (dark navy blue box).

Few EVs were released from the initial PBS control; an average of 49% of EVs were released by subsequent trypsin digestion (**Figure 34B**) with an associated high variation between the samples (±27%). For proteinase K, 96% of EVs were released. To ensure proteinase K digestion on its own could produce the same high release efficiency, 4 samples were processed with a single proteinase K digestion step followed by a secondary proteinase K treatment to serve as a reference point for calculating release efficiency. The release efficiency associated with proteinase K digestion was highly reproducible at a resultant 99 ±1% (n = 4) from a single step (**Figure 34B**). The lower release efficiency observed through trypsin digestion could be attributed to the digestive selectivity of the proteolytic enzyme and not effectively cleaving all potential mAb-antigen associations.

The high efficiency observed for proteinase K digestion is impressive due to the high strength of the affinity complex confining the EVs to the surfaces. Because extremely high forces are required to break even one bond, this data suggests that proteinase K can cleave all mAb-antigen bonds even at a relatively low concentration. Proteinase K digestion with a subsequent sonication step was found to efficiently release EVs from the EV-MAP surfaces (99 ± 1%) and maintain the integrity of the EVs for NTA and TEM analysis. Therefore, the described protocol was used for all subsequent release procedures from EV-MAP.

Minimizing non-specific interactions through blocking and washing buffers. Lower flow rates improve recovery of EVs using mAb-decorated capture surfaces (as seen in **Figure 26**) because they increase the residence time thereby giving EVs more time to diffuse to the device surfaces. However, the lower flow rates also can render mechanical fluidic disruption unable to remove any nonspecifically bound EVs or other biological particles such as proteins or membrane aggregates from the device. Chemical passivation of the surfaces through a blocking

buffer could mitigate these limitations by keeping nonspecific entities from binding, while stringent washing after sample infusion could remove nonspecific particles previously bound.

Two blocking buffers, 1% BSA and 1% BSA supplemented with 1% PVP-40 (polyvinylpyrrolidone, 40 kDa) were investigated in their ability to minimize non-specific binding. BSA passivates the surface by binding to any sites unoccupied by antibodies or any sites where the antibody is conjugated with the Fab region or antigen-binding region facing toward the surface, thereby preventing nonspecific particles from binding [214]. BSA is commonly used as a blocking agent in immunostaining, western blotting, or ELISA. PVP-40 is a hydrophilic polymer-based blocking agent used in western blotting [215] as well as RNA blotting as part of Denhardt's blocking solution for membrane-based hybridization. It's superhydrophilicity allows for blocking of hydrophobic interactions. The same buffer used in blocking the surface or 0.2% Tween 20® was implemented to wash the EV-MAP devices after affinity selection. Tween 20® is a nonionic surfactant routinely used in western blotting and immunostaining procedures to wash away weak particle-surface interactions.

To test the efficiency of these blocking and washing buffers, 500 µL of donor plasma was infused into anti-EpCAM and anti-IgG2A isotype decorated devices. These donor samples came from Bioreclamation and were only tested for the presence of infectious diseases. These samples were only used in assay optimization as they do not necessarily reflect healthy individuals as no other medical information is known. The affinity-purified EVs were proteolytically released via 0.2% proteinase K for NTA. The nanoparticle concentrations were then compared from the two mAb fractions, with the isotype serving as a nonspecific control. Many microfluidic devices have used isotypes during development to optimize affinity-capture of EVs [119, 163, 193, 216]. To determine the number of specifically bound particles, it was assumed that the anti-EpCAM

devices would include both specifically isolated EVs and nonspecific particles, with the nonspecific EVs quantitated based on the EV concentration measured from the isotype control devices. The number of specific EVs was then defined as:

$$Specifically\ bound\ EVs = EV_{EpCAM} - EV_{isotype} \qquad \text{(Eq. 11)}$$

When assessing the NTA results, high levels of nonspecific nanoparticles (NPs) were found in the isotype control blocked and washed with only 1% BSA (**Figure 35**). To determine whether the non-specific binding was due to electrostatic interactions, the salt concentration of the washing buffer was increased to 1 M. However, a high background of nonspecific NPs was still observed (**Figure 35**). The high non-specific binding present when using a high-salt wash suggested the non-specific interactions to be hydrophobic in nature as opposed to electrostatic.
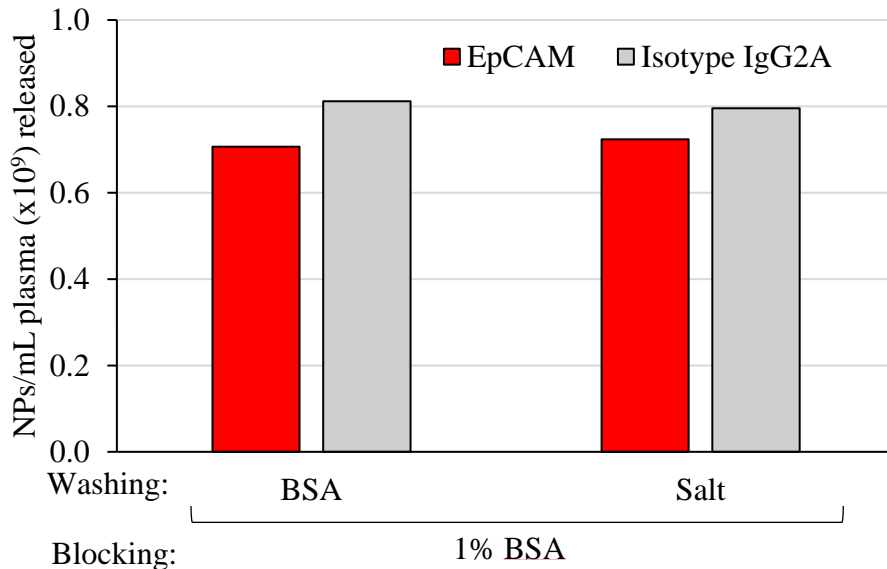
Figure 35. Effect of high salt or 1% BSA wash on nonspecific binding measured through NTA NP concentration. NTA NP concentration for either an anti-EpCAM or IgG2$_A$ isotype immobilized device washed with either a high salt buffer (1 M) or the same buffer used to block the devices (in this case 1% BSA in PBS). EVs were released off the devices through proteolytic digestion with 0.2% proteinase K and 10 min sonication. Five-hundred µL of donor plasma was processed. These devices were processed within the same experiment and show both BSA alone and high salt as a washing step result in high levels of nonspecific binding, as large EV concentrations occurred in both Isotype fractions.
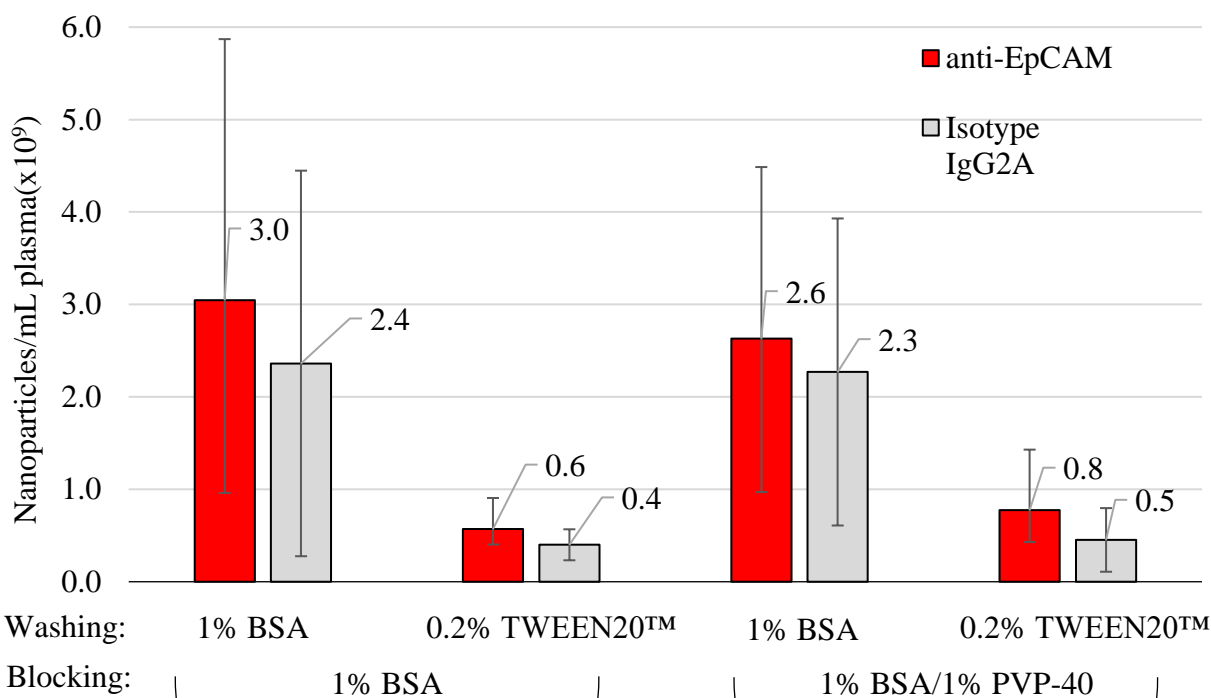
Figure 36. NTA NP concentration measurements for various blocking and washing combinations of EV-MAP. Five-hundred µL of four donor plasma samples were processed through the EV-MAP assay to compare the level of nonspecific binding, determined through the isotype control (IgG2$_A$), to the NP concentrations resulting from specific anti-EpCAM isolation. Different combinations including blocking buffers of either 1% BSA in PBS or 1% BSA/1% PVP-40 in PBS and the same buffer as a washing agent or 0.2% Tween 20® in TBS were tested for each donor sample processed through EV-MAP. Data labels are included to show the number of specific NPs that could be calculated from the number of nonspecific NPs based on **Eq. 11**. The blocking and washing combination of 1% BSA and 0.2% Tween 20® produced the lowest nonspecific background of EVs. However, the combination of 1% BSA/1% PVP-40 and 0.2% Tween 20® resulted in low nonspecific binding and increased the number of specific NPs.

We next incorporated 0.2% Tween 20® into the washing buffer, which drastically decreased the nanoparticle concentrations **(Figure 36)** by washing away nonspecific particles after initial binding to the surface. However, only 2×10^9 NPs/mL were specifically bound. It was hypothesized that the nonspecific fraction was competing for binding sites to the mAbs, shifting the focus toward optimizing the blocking buffer to improve passivation of the antibody surfaces to increase the yield of specific EVs captured. Addition of PVP-40 to the blocking buffer with a

subsequent 0.2% Tween 20® washing step increased the concentration of specific nanoparticles up to 3×10^9 NPs/mL of plasma (**Figure 36**). Therefore, the blocking and washing buffer combination of 1% PVP-40/1% BSA in PBS and 0.2% Tween 20® in TBS was found to both decrease the nonspecific binding while increasing the specific EV yield when compared to other buffer combinations. This optimum combination was then used for all subsequent EV-MAP assays.
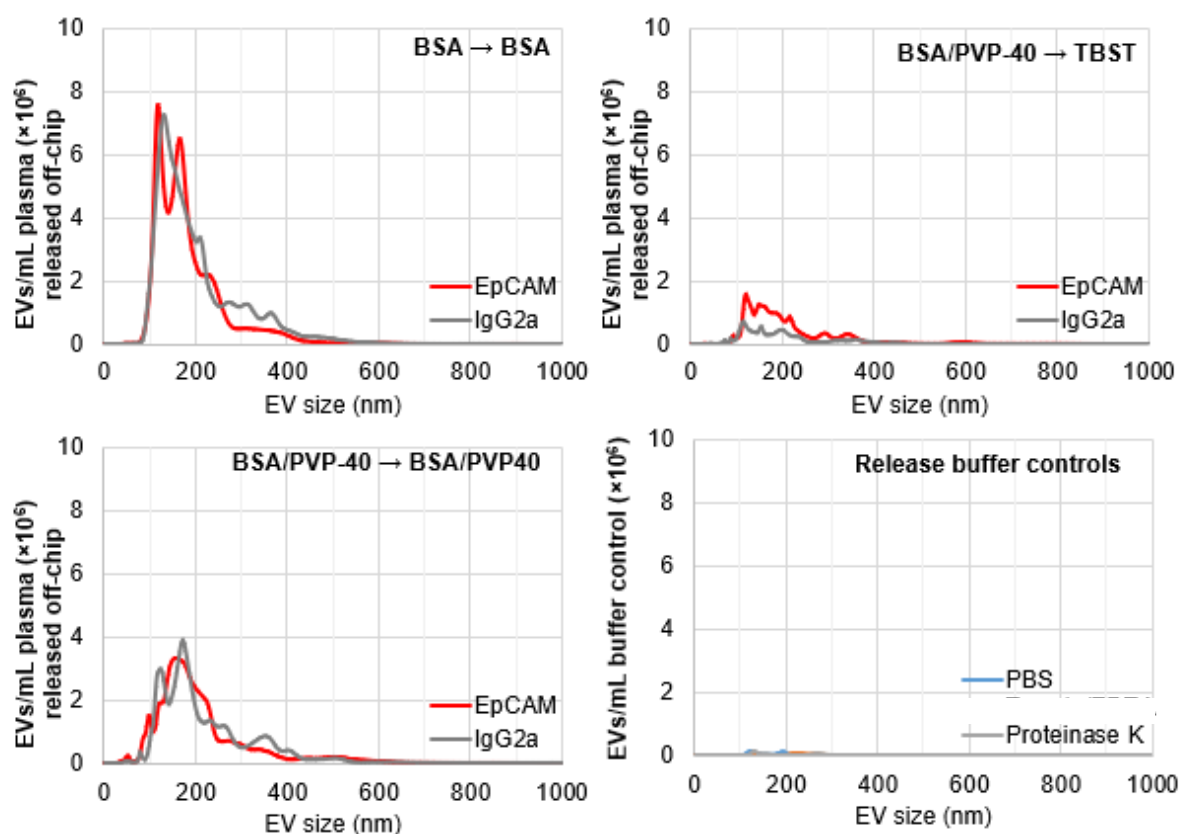
Figure 37. Size distribution of EVs processed through EV-MAP by various blocking and washing combinations. NTA-derived NP size distributions of anti-EpCAM and isotype EV fractions isolated from 500 µL of a donor plasma processed through EV-MAP using various blocking and washing combinations. A shift in NP size is apparent with the decrease of nonspecific NPs. The bulk NP population first consisting mainly of particles from 150-200 nm spread to a more heterogeneous distribution with improved blocking and washing buffer schemes. Minimal particles were present in the background of PBS and proteinase K (bottom right graph).TBST refers to 0.2% Tween 20® in tris-buffer saline (TBS)

NTA also provided size distribution measurements, showing a shift in the NP size when various blocking and washing combinations were employed (**Figure 37**). Initially, with high levels of non-specific binding still present, a population mainly centered around 150-200nm was observed. This peak decreased with the decrease of non-specific EVs, better separating the heterogeneous mixture of EVs ranging up to ~400 nm in size. Through this observation it is suggested that most nonspecific particles are around 150-200 nm, with the heterogeneity of the specific population confounded due to this background.

2.2.5 EV-MAP validation through breast cancer cell lines

Validation of EV isolation from breast cancer cell lines through TEM and quantification using NTA. Two breast cancer cell lines were cultured in EV-depleted FBS: MCF7 cells representing an epithelial phenotype – EpCAM(+)/FAPα(-) – and mesenchymal-like Hs578T cells – EpCAM(low)/FAPα(+) [98]. These cell lines provided a controlled sample for verifying the isolation of EVs from clinically significant sources consisting of either epithelial cancer cells or mesenchymal cells. In the body, epithelial cells may transition into a mesenchymal phenotype and in the process lose expression of cell adhesion proteins and gain mesenchymal characteristics such as expression of proteins involved in cell motility and degradation of extracellular matrices[53]. Because of this phenotypic change, mesenchymal cells show increased ability to invade surrounding local tissue and could even promote metastasis.

To isolate EVs from the conditioned cell media, EV-MAP devices were either modified with anti-EpCAM or anti-FAPα mAb to selectively capture EVs of either mesenchymal or epithelial origin. Several studies have targeted the epithelial cell adhesion molecule (EpCAM) as a method of isolating epithelial-derived EVs, particularly in cancer patient samples [121, 185, 186]. EpCAM is an outer membrane protein found on epithelial cells that assists in cell-to-cell

adhesion. In breast cancer, where 90% of cases originate in epithelial tissue [217], the anti-EpCAM mAb serves as a suitable method of isolating disease-specific EVs. EpCAM has successfully been employed for isolating CTCs from whole blood, having been incorporated as a target molecule in the FDA approved CTC CellSearch System assay™.

It is now known that the sole selection of EpCAM-containing biomarkers can underrepresent the full landscape of cell types resident within a tumor, or in this case EV types. Cells undergoing the epithelial-to-mesenchymal transition (EMT) lose characteristics of an epithelial phenotype and gain mesenchymal features including the notably lower expression of EpCAM [98]. One study showed the selection of mesenchymal-associated fibroblast activation protein alpha (FAPα) circulating tumor cells (CTCs) to be an orthogonal marker compared to EpCAM selection by observing 90% of the selected CTC cells to show no co-expression of these antigens. FAPα is a protein found on the membrane of reactive stromal fibroblasts, particularly in epithelial cancers, and promotes tumor growth and metastasis [218]. The addition of FAPα selection has resulted in a clinical sensitivity of 100% for several metastatic cancer types [98]. To ensure the selective capture of all EVs originating from breast cancer cells, both anti-FAPα and anti-EpCAM mAbs were used in this study as the selection mAbs.

Isotypes were also used to interrogate the level of non-specific binding in the EV-MAP from a controlled sample (e.g. media). These isotypes have the same structure and come from the same class and subclass as a specific antibody but differ in their variable (Fab) region, ensuring that they do not bind to the antigen of interest. Isotypes have previously been used as a method of assessing the specificity of microfluidic EV isolation assays [121, 190, 191].

For EV isolation, 500 μL of conditioned culture media was processed through either an anti-EpCAM, anti-FAPα, or IgG_{2A} isotype immobilized EV-MAP device. IgG_{2A} should show

nonspecific binding artifacts in the assay as the Fab region is not specific to any antigens found in humans. Affinity-selected EVs were released from the capture surface via digestion with 0.2% proteinase K for an incubation time of 30 min at 37° C and subsequent 10 min sonication. Released EVs were then quantified for size and concentration using NTA (**Figure 38A, B**). The released fractions were also analyzed by TEM (**Figure 39**) to assess the morphology of particles detected by NTA.

The size of isolated EVs ranged from 30 – 300 nm with the average size in all fractions ~125 nm (**Figure 38A**). The NTA results from the EV-MAP processed MCF7 media showed more than twice the number of nanoparticles captured on the anti-EpCAM selecting device, with equivalent concentrations between the anti-FAPα and nonspecific IgG$_{2A}$ control (**Figure 38B**). This trend aligns well with the cell line's epithelial phenotype creating an EpCAM(+) and FAPα(-) expression for the MCF7 cell line [219]. NTA detected slightly more nanoparticles on the anti-EpCAM fraction from the Hs578T conditioned media and relatively none above the nonspecific background in the anti-FAPα fraction. EVs were expected to be captured in both the anti-FAPα and anti-EpCAM fractions as this cell line is known to express both antigens. The low number of EVs captured in the anti-FAPα fraction could be attributed to the expression of isoforms of the FAP protein [220]. Ten different mRNA transcripts are known to produce FAP isoforms from alternative splicing (http://www.ncbi. nlm.nih.gov/IEB/Research/Acembly/av.cgi? Db=human&c=Gene&1=FAP). One known isoforms is 27 kD [220] and resides inside the cytosol and therefore if expressed, could not complex with the mAbs on the surface of the device. Further investigation into FAP isoforms is required to understand their subcellular location and expression within various cell lines.
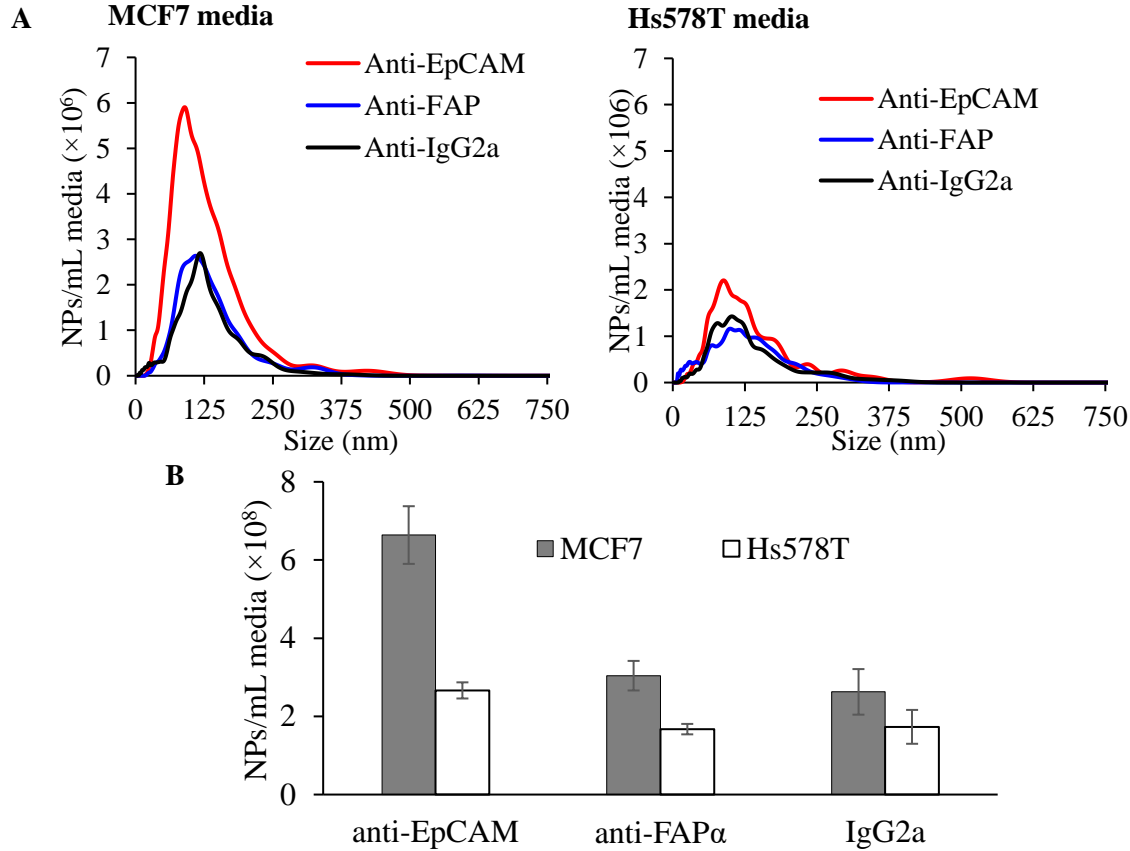
Figure 38. Size and concentration of EVs isolated by EV-MAP from MCF7 and Hs578T cell lines. Size distribution and concentration of EVs isolated from MCF7 and Hs578T conditioned media using EV-MAP. Five-hundred µL of conditioned media was processed through anti-EpCAM, anti-FAPα, and IgG2$_A$ isotype immobilized devices. EVs were released through 0.2% proteinase K digestion and subsequent 10 min sonication. (**A**) The line graphs illustrate the size distribution within the release fractions as measured by NTA. (**B**) The bar graph shows the average concentration of particles found in each isolated fraction through NTA from 5 replicate measurements. Error bars represent standard deviations from these 5 measurements.

When analyzing the TEM images, EVs were observed with the traditional "cup-shape" morphology (**Figure 39**). Almost no particles were present in the TEM images from the isotype fractions. This suggests that the 2×10^8 nanoparticles/mL concentration observed through NTA was inherent background associated with the NTA detection method. Furthermore, the observation of EVs in the anti-FAPα fraction from the Hs578T cell line media through TEM suggests that the concentration was too low to discern from this NTA background.
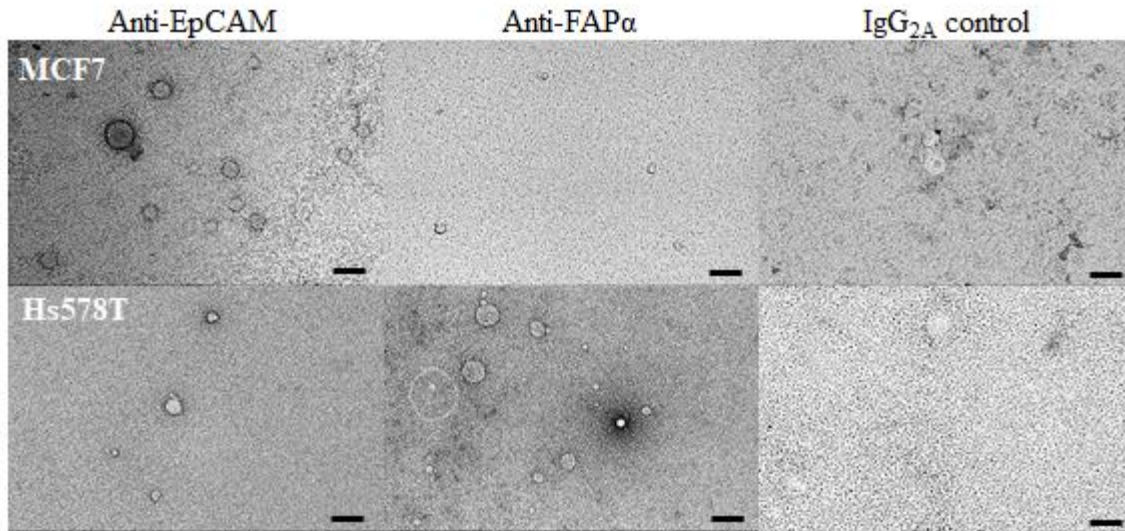
Figure 39. TEM images of EVs isolated by EV-MAP from Hs578T and MCF7 cell lines.
TEM images of EpCAM(+) and FAPα(+) EVs as well as images of the isotype fractions isolated from 500 µL of Hs578T or MCF7 conditioned media processed through anti-EpCAM, anti-FAPα, and IgG2$_A$ isotype immobilized EV-MAP devices and released using proteolytic digestion with 0.2% proteinase K. Scale bars are 500 nm.

NTA is based on the concept of Brownian motion and laser light scattering from particles. This pattern is recorded and allows the NTA software to track the particle's distance traveled to determine the diffusion coefficient (eq. 12) which is then applied in the Einstein-Stokes equation (eq. 13), resulting in a particle size:

$$D = \frac{(x,y,z)^2}{6t} \qquad \text{(Eq. 12)}$$

$$D = \frac{4k_bT}{3\pi\eta d} \qquad \text{(Eq. 13)}$$

The diffusion coefficient D incorporates both the distance a particle moves in the x, y, and z directions and the time t required to move that distance. The diameter d of the particle is then back calculated from the known diffusion coefficient D, Boltzmann constant k_b, temperature T, and viscosity η. Most NTA instruments can detect any particle ≥70nm [221], meaning the procedure counts anything above 70 nm moving in the solution irrespective of whether it is an

EV when determining concentration. Studies have shown that when particles are ≥400nm is size, they are often counted multiple times by NTA[221-223] and thereby overestimate the overall concentration potentially by over 1 billion NPS/mL[221]. Further, because NTA only tracks particles based on light scatter it cannot discern EVs from other particles present in samples such as proteins, protein aggregates, etc. Arraud *et al.* compared EV concentrations from NTA to a custom method of immunogold labeling through the presence of Annexin V known to reside in the membrane of all EVs, then centrifuging the EVs onto TEM grids for manual counting of particles [163]. A large disparity was found, from ~52,000 EVs/µL detected in healthy plasma from cryo-TEM gold nanoparticle labeling compared to 10^9 EVs/µL of plasma reported from NTA results within the literature [164].

EV mRNA profiling from EV-MAP isolated Breast cancer cell line EVs. Conducting mRNA expression profiling on breast cancer patient samples identifies the molecular subtype of the disease, enabling physicians to stratify patients based on the associated predicted prognosis and treatment response. FDA approved commercial tests exist such as the Prosigna® or Oncotype Dx® for analyzing mRNA from breast cancer tissue, with this material currently obtained from a solid tissue sample and often comes from the same tissue sample used first for immunohistochemistry and morphological as well as nuclear assessment of cells. Pathologists therefore may not have enough sample remaining to perform mRNA analysis. Even if they procure enough mRNA for the assays, the sample only comes from a single biopsy of the tumor, potentially misrepresenting the heterogeneity of the disease. EVs may create an alternative source for mRNA because their cell of origin, such as a cancer cell, can transfer mRNA [133] into the EVs. A simple blood draw would then be required to obtain sample as opposed to an

invasive biopsy. However, it is first important to assess whether EVs package mRNA from their cell of origin by comparing EV and cell mRNA expression profiles.

EV mRNA expression profiling was performed on Hs578T and MCF7 EVs isolated using EV-MAP. Five-hundred µL of Hs578T cell media was processed through EV-MAP devices conjugated with either anti-EpCAM or anti-FAPα mAbs. The captured EVs were lysed on-chip for TRNA extraction and purification. In procuring cell mRNA, media either cultured in EV-depleted FBS or regular FBS was centrifuged at 300g for 10 min to pellet the cells for direct lysis and the TRNA extracted using the same RNA purification kit. TRNA aliquots of 2 µL were reverse transcribed using poly(dT) primers to generate cDNA only from mRNA for downstream ddPCR.

ddPCR has been used to assess the miRNA content [224, 225] or mRNA expression [132, 162, 225] in various EV populations. Digital PCR (dPCR) employs absolute quantification by partitioning template DNA or cDNA into tens of thousands of nanoliter-sized replicate reactions, where some contain the target of interest and others do not. This distribution of target template into small confined volumes increases the fluorescence signal generated from the PCR reactions, allowing for sensitive analysis of a single copy of target template in one of the many "reactions" or droplets. These reactions are then subjected to end-point PCR and results analyzed through fluorescence signal only emitted from reaction droplets containing one or more copies of the cDNA, correlating with a positive outcome. The fraction of positive reactions is then interpreted using Poisson statistics [226]. The use of Poisson statistics takes into account that a single reaction could have multiple copies of target sequence, with a higher number of positive reactions increasing this probability [226]. ddPCR specifically partitions the template from one reaction volume into aqueous droplets composed of a water-oil emulsion, decreasing the time

needed for reaction set-up thereby increasing throughput. The relationship between the fraction of positive droplets and the resulting copies/µL detected when applying the Poisson distribution was previously shown in **Figure 21** from the ddPCR section under Methods (see Eq. 1).

Quantitative PCR (qPCR) or real-time PCR is commonly used for analyzing extracellular RNA [125, 162, 224, 227-230], but has disadvantages compared to ddPCR. Unlike ddPCR, qPCR does not provide absolute quantification of copies and rather determines the rate of target amplification based on a cycle threshold (Ct) value in comparison to a standard calibration curve that will result in relative expression of the target. These calibration curves may increase the variation in assay results between different laboratories particularly if different materials are chosen for standards. Internal variance may also occur due to potential changes within the calibration curve over time [231]. Optimization of all primer pairs used is also important to ensure amplification efficiency is consistent, with poor optimization contributing to low reproducibility of results by creating inaccurate Ct values [232].

ddPCR is not dependent on the amplification or reaction efficiency because it measures the expression of target molecules at the end of all PCR cycles. For this reason, the procedure also requires no calibration curves, decreasing the external and internal variance[233] compared to qPCR. ddPCR is also associated with an increased ability to analyze low-abundance targets because it partitions the targets into small nanoliter-sized volumes for subsequent PCR within the confined space, increasing the positive signal generated. Both the lower limit of quantification and the lower variance are important when assessing often low disease-associated gene expressions relative to the background which is why ddPCR was chosen in this study.

Table 13. Proteins encoded by genes chosen for the EV-MAP mRNA expression panel along with their function. List of genes included in gene panel for analysis of breast cancer cell line mRNA expression. Each has a brief description of the function and protein encoded, with all genes split amongst categories based on the cell type with which they are most highly or selectively expressed. All descriptions were reproduced from https://www.ncbi.nlm.nih.gov/gene.

cell origins of high expression	gene	function of encoded protein
epithelial phenotype	EpCAM	Transmembrane glycoprotein expressed in epithelia to facilitate Ca^{2+}-independent cell-to-cell adhesion and involved in proliferation, cell migration, and differentiation.
	CK19	Type I cytokeratin responsible for maintaining structural integrity of epithelial cells.
mesenchymal phenotype	FAPα	Membrane gelatinase apart of the serine protease family expressed in reactive stromal fibroblasts and facilitates extracellular matrix degradation to increase cell motility and allow them to move through surrounding tissue.
	VIM	Type III intermediate filament protein making up a large portion of the cytoskeleton in mesenchymal cells to maintain cell structure.
	IL8	Protein of the chemokine family often secreted by neutrophils to help guide these cells to the infection, also found to promote angiogenesis.
all EVs	CD81	Protein from the tetraspanin family found on the cell surface to facilitate signal transduction for regulating cell development, activation, growth, and motility.
breast cancer stem cell phenotype	CD24	Sialoglycoprotein expressed on granulocytes and B cells to mediate growth and differentiation signals.
	CD44	Transmembrane glycoprotein facilitating cell-cell interactions, adhesion, and migration. Used in many cellular functions such as lymphocyte activation, hematopoiesis, and tumor metastasis.

The gene panel chosen for EV-mRNA expression profiling included an assortment of epithelial and mesenchymal-associated genes to differentiate between the two cell lines based on phenotypic orthogonality (**Table 13**). This panel contained epithelial cell adhesion molecule (*EpCAM*), cytokeratin 19 (*CK19*), fibroblast activation protein α (*FAPα*), vimentin (*VIM*), and interleukin 8 (*IL8*). The panel also included well-established breast cancer stem cell markers *CD44* and *CD24*, as they distinctly indicate the originating cell line and may predict the risk of distant metastasis [234]. Hs578T cells express *CD44* and low expression of *CD24* (CD44(+)/CD24(low)), with this cell line presenting a mesenchymal phenotype known to

facilitate tumor progression or potentially metastasis. This cell line highly correlates with the claudin-low subtype based on gene expression profiling [235], fitting with the mesenchymal-like phenotypic nature of this subtype. MCF7 cells show expression of both CD44 and CD24 (CD44(+)/CD24(+)), and the cell line shows gene expression profiling most similar to the luminal B breast cancer subtype[235]. Expression of the tetraspanin *CD81* was also examined as it is a general EV marker.

The mRNA expression profiles were determined by normalizing the copy results from ddPCR to the mass of total RNA (TRNA) input into the reverse transcription (RT) reaction (see Eq. 2 in ddPCR section of Methods). The dilution of the RT product refers to any initial dilution of the cDNA sample before putting into the PCR reaction as well as the $1/10^{th}$ dilution inherent when taking 2.2 µL of cDNA from a 20 µL RT reaction. As an example, if 2.2 µL is directly taken from the 20 µL RT reaction then the dilution factor for this cDNA would be ~9 (20 µL RT reaction/2.2 µL cDNA taken out). Furthermore, because this is normalized to the TRNA mass input into RT, the TRNA concentration provided by HS RNA Tape analysis was multiplied by the 2 µL TRNA volume added to the RT reaction.

The anti-EpCAM and anti-FAPα EV mRNA fractions from the MCF7 cell line both showed high expression of the epithelial-associated gene *CK19*, correlating well with the high expression also observed in the MCF7 cells (**Figure 40A**). However, mesenchymal signatures are also present in both fractions through expression of *IL8* and *FAPα*. This suggests that EVs may preferentially package these low-expressed mRNA transcripts compared to their cells of origin. Other studies have shown discrepancy between breast cancer cells and their secreted EV's gene expression[134, 236], with one finding only a 5% concordance between mRNA transcripts overexpressed in tumor cells versus EVs[134] It is interesting that any FAPα(+) EVs were

isolated from the MCF7 epithelial phenotype cell line, as this cell line does not express FAPα[237]. However, as stated previously, alternative splices of the FAP gene exist [220] and few of them have been extensively studied. Little research has been conducted to assess the expression of each splice variant in the MCF7 cell line, so it is unknown whether a splice variant encoding a different FAP isoform could be expressed. Lastly, the MCF7 EVs showed lower expression of the pan-EV protein CD81 when compared to the MCF7 cells. This low expression of CD81 in breast cancer EVs was also observed in another study performing differential ultracentrifugation on EVs and assessing the pellet protein contents [238]. Therefore, it is important to note that CD81 is not highly expressed in all EVs irrespective of their cell origin.

Overall, several differences in expression profiles between the MCF7 cells and MCF7 EVs were observed. Discrepancy between host cell and EV mRNA expressions has previously been observed in studies using microarray analysis, where certain transcripts were highly expressed in EVs compared to the low or even lack of expression observed in the cell of origin [115, 134]. Therefore, it is not impossible for EVs to differ in expression of certain genes from their cell of origin.

Hs578T EVs isolated using the anti-EpCAM and anti-FAPα immobilized devices showed low expression of epithelial-associated genes (*EpCAM* and *CK19*) (**Figure 40B**), as was expected due to the mesenchymal phenotype of the cell line which also correlated with the mRNA expression pattern observed from Hs578T cell mRNA (**Figure 40B**). An increase in copies/ng of mRNA was observed across all genes within the panel for the anti-FAPα fraction compared to the anti-EpCAM EV fraction, correlating to the FAPα(+)/EpCAM(low) expression characteristic of the Hs578T cell.
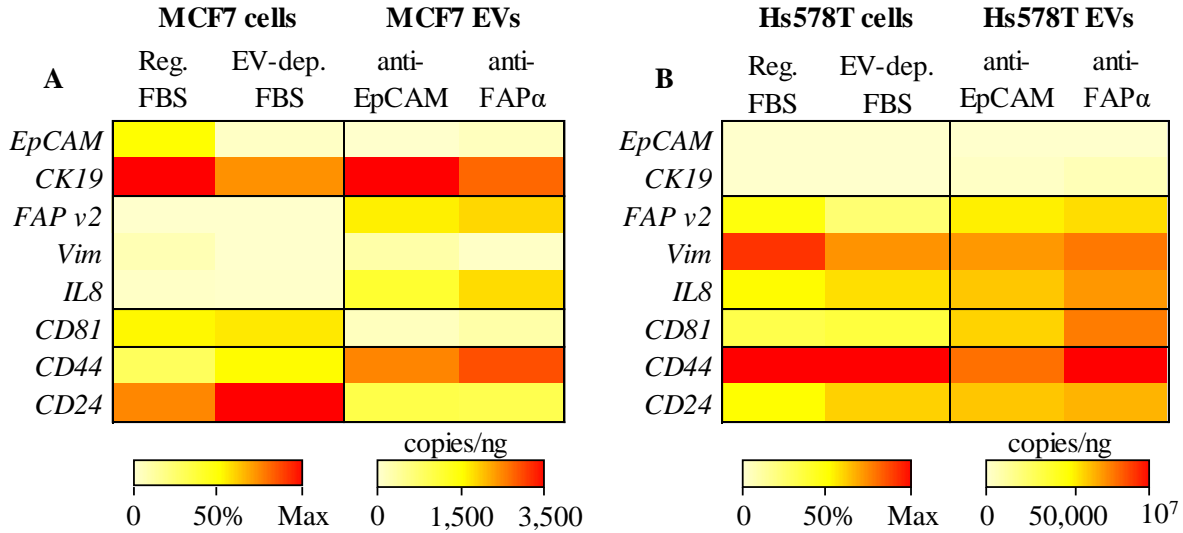
Figure 40. mRNA expression profiling of EVs isolated by EV-MAP from MCF7 and Hs578T conditioned media. mRNA expression profiling of (**A**) MCF7 and (**B**) Hs578T EVs isolated from conditioned media by the three-bed EV-MAP device immobilized with either anti-EpCAM or FAPα antibody for comparison with the mRNA expression from their cells of origin. EVs isolated on the device were lysed on-chip to extract and purify TRNA, where 2 µL of the 6.5 µL elution volume was used for RT-ddPCR. Cells were centrifuged at 300g for 10 min and then directly lysed for TRNA extraction, with 1 µg added for RT then subsequent ddPCR. The expression profiles of the selectively captured EVs were set to the same scale based on the highest number of copies observed and normalized to the TRNA mass input into the RT reaction, accounting for subsequent dilutions (Eq. 2). The cell mRNA expression from either culture media grown in regular FBS or conditioned with EV-depleted FBS were scaled to the highest normalized copy number for each respective sample.

To accurately compare the EV gene expression profile to that of cells, it was important to determine how the loss of bovine EVs could affect the gene expression of cells, especially with previous studies finding human cancer cell lines transitioned into EV-depleted FBS to decrease in their growth due to the lack of bovine EV-uptake [206, 239]. The profile of the mRNA from the Hs578T cells cultured in EV-depleted FBS showed little difference when compared to the profile from cells cultured in regular FBS (**Figure 40B**), with both mRNA fractions still exhibiting the expected mesenchymal-like phenotype with high expression of mesenchymal associated genes such as *VIM*, *FAPα*, and *IL8* and low expression of epithelial associated genes *EpCAM* and *CK19*. The MCF7 cells cultured in EV-depleted FBS and cells cultured in regular

FBS both showed the expected epithelial phenotypic expression profile with low expression of mesenchymal-associated *VIM, FAPα,* and *IL8* genes. The MCF7 cells cultured in EV-depleted FBS showed markedly higher expression of *CD24* compared to the cells cultured in regular FBS. However, the MCF7 cell line is known to express both *CD24* and *CD44* (*CD24(+)/CD44(+)*) so this change in expression still aligns with the expected gene profile. This similarity in mRNA profiles provides evidence that EV depletion of the FBS does not mask or alter the expression profiles from what is expected for either the epithelial or mesenchymal cell phenotype.

Evaluation of EV-MAP specificity using donor plasma samples. After optimizing the blocking and washing buffers to minimize nonspecific binding, it was important to assess the specificity of the EV-MAP assay resulting from processing a complex sample such as plasma. To do this, mRNA expression profiles were compared between the specific capture of EVs and nonspecific background represented by EV mRNA isolated from the isotype EV-MAP devices. Furthermore, the specific EV-MAP isolation procedure using anti-EpCAM and anti-FAPα antibodies was also compared to the bulk isolation of all EV populations represented through using a pan-EV antibody anti-CD81.

In order to assess the specificity of the EV-MAP assay, 500 µL of pooled donor samples were infused into two sets of devices that were anti-EpCAM, anti-FAPα, anti-CD81, and IgG$_{2B}$ mAb functionalized. Many microfluidic affinity-based EV isolation platforms focus on the capture of all EVs, targeting pan-EV markers such as tetraspanins CD81, CD63, or CD9 [190-192]. The isolation of all EVs may confound mRNA expression differences that could otherwise prove clinically valuable, similar to the loss of expression of disease-associated genes previously seen [162]. Therefore, anti-CD81 was used to investigate the result of isolating bulk EVs

compared to the specific epithelial or mesenchymal EV approach used in the EV-MAP assay.

IgG$_{2B}$ is the isotype to anti-CD81 and therefore used to assess the assay specificity.
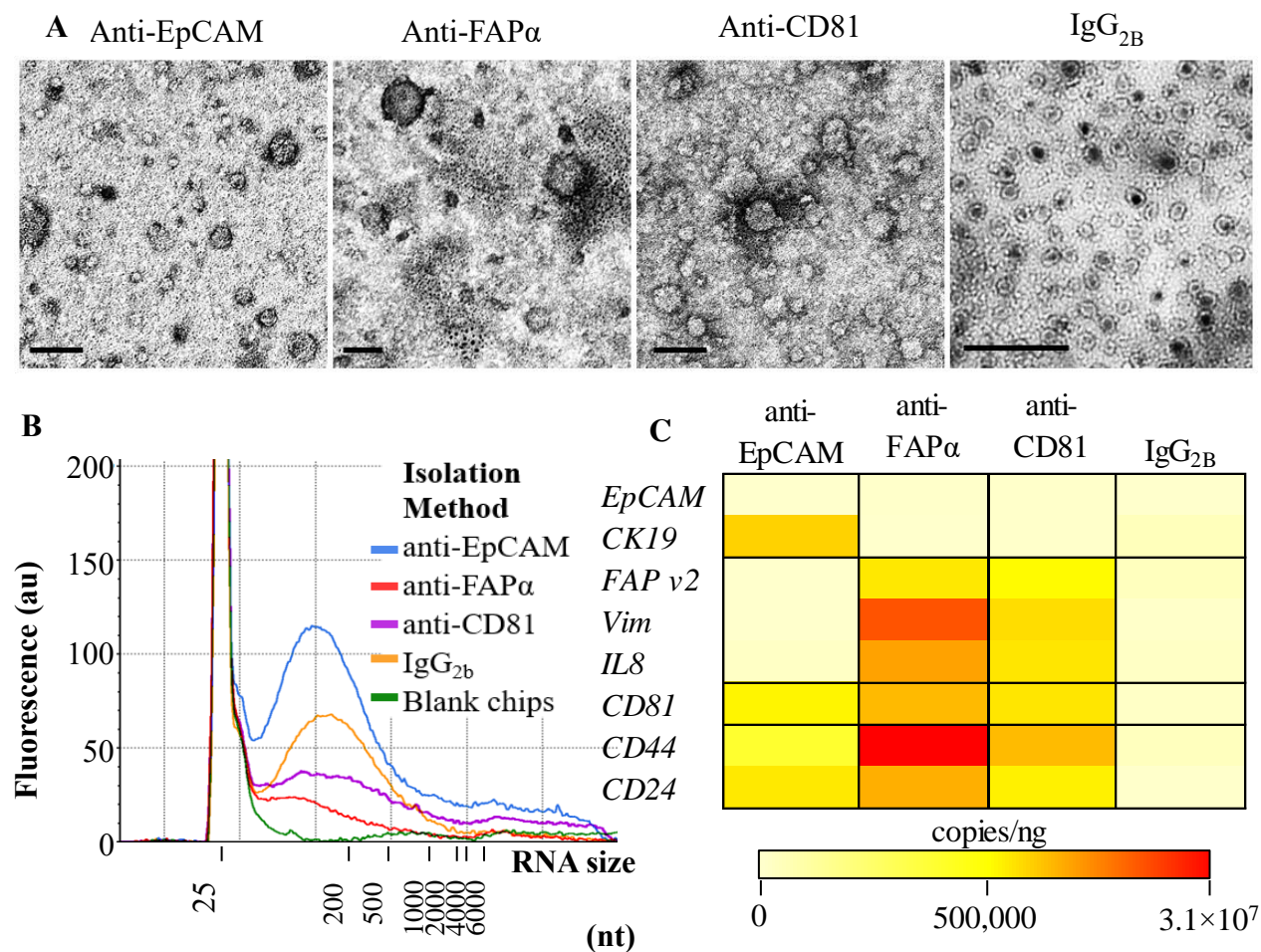

Figure 41. Specificity of the EV-MAP assay through expression of target genes from a donor plasma sample. Five-hundred µL of a pooled donor sample was processed through either anti-EpCAM, anti-FAPα, anti-CD81, or IgG$_{2b}$ immobilized devices. (**A**) Isolated EVs from one set of devices were released by 0.2% proteinase K digestion for TEM imaging. The characteristic cup-shape morphology of EVs was observed in all fractions, including the isotype. All scale bars are 100 nm. (**B**) A separate set of EV-MAP devices was processed in parallel using the same pooled donor sample for EV lysis on-chip and TRNA purification. TRNA was pooled from three devices immobilized with the same mAb to increase TRNA yield closer to the HS RNA Tape quantification range (500 pg/µL). All fractions contained TRNA with sizing similar to that found in EVs. (**C**) Two µL of the TRNA was then added to an RT reaction, with 2.2 µL of the cDNA product input into-ddPCR for mRNA expression profiling. The total copy results were normalized to the ng of TRNA input into RT (Eq. 2 in ddPCR section of 2.2), accounting for any initial cDNA sample dilutions as well as the dilution of the TRNA into the total 20 µL RT reaction. The isotype fraction resulted in negligible copies of the genes targeted in the EV-MAP panel, creating a specificity of $99 \pm 1\%$.

EV-MAP devices were all blocked with 1% BSA/1% PVP-40 and washed with 0.2% Tween 20®. After the washing step, one set of devices was treated with proteinase K for release of EVs for TEM imaging (**Figure 41A**) while another set of devices was subjected to TRNA purification (**Figure 41B**) and subsequent RT-ddPCR analysis (**Figure 41C**). TRNA from three EV-MAP devices were pooled together for RT-ddPCR and HS RNA Tape analysis.

TEM images of the isotype fraction did show the presence of EVs. The majority of EVs observed from the isotype fraction were small exhibiting a diameter <30 nm (**Figure 41A**). The presence of EVs in the isotype fraction was verified by the existence of TRNA (**Figure 41B**). All TRNA traces were indicative of EVs as the majority of the sizes ranged from 200 to 500 nt.

The non-specific EVs captured in the isotype fraction contained negligible copies/ng for the target genes in the panel, therefore showing the assay results in a high specificity of $99 \pm 1\%$ when analyzing these target genes. This is important because it shows that the expression of disease-associated genes and differences of gene expression between different disease-associated EV populations such as epithelial or mesenchymal-derived EVs are not masked and easily delineated through EV-MAP. This suggests that EV-MAP could provide clinically relevant mRNA expression information that could prove beneficial in the breast cancer clinical pathway which already uses transcriptome analysis in disease diagnosis.

When comparing the bulk isolation of EVs to the specific isolation of epithelial and mesenchymal derived EVs, the anti-CD81 bulk fraction masked the epithelial phenotype observed from the EpCAM(+) EVs through negligible expression of *CK19*. The anti-CD81 fraction instead only presented a mesenchymal-like gene profile as was also seen from the anti-FAPα fraction. Furthermore, expression differences between genes within the anti-CD81 fraction were less pronounced in comparison to the specific isolation of FAPα EVs. Both the masking of

the epithelial phenotypic profile seen from the specific anti-EpCAM isolated EVs and the

confounding of expression differences between the genes found in the anti-CD81 fraction

suggest that the capture of all EVs may confound disease-associated mRNA expression and

expression differences which aligns with a previous study assessing bulk EV isolation through

differential ultracentrifugation[162].

2.2.6 EV-MAP processing of diseased and healthy control samples. Healthy control samples

and breast cancer patient samples were received from KUMC. Women coming in for routine

mammograms and known to have no current diagnosis of cancer were provided as healthy

controls. The breast cancer samples were either banked in the KUMC Biorepository (collected in

2017) or extracted from patients at the Indian Creek clinic at KUMC (collected in 2019). A

distribution of both receptor status, stage, and even disease diagnosis was found within the

patient cohort (**Table A1**). Most patients had received some form of treatment prior to the blood

draw and were older than 55 years of age.

Five-hundred μL of these samples were processed through the anti-EpCAM and anti-

FAPα EV-MAP devices, using the optimized blocking and washing buffer compositions of 1%

PVP-40/1% BSA in PBS and 0.2% Tween 20® in TBS, respectively. After processing, EVs

were lysed off-chip for TRNA purification and subsequent RT-ddPCR analysis to compare gene

expression profiles. Three healthy controls and ten patient samples were processed.

None of the healthy controls or patient samples resulted in a TRNA concentration

detectable by HS RNA Tape (limit of detection = 100 pg/μL). All EV TRNA samples were

input into RT (2 μL of TRNA) for ddPCR analysis. To conserve expensive ddPCR resources,

patient and healthy control cDNA was first assessed through a smaller screening panel of genes.

CK19, VIM, and *CD81* were chosen because together they characterized both the epithelial and

mesenchymal phenotype of interest as well as a general EV marker. Low copy numbers using

ddPCR were observed (Example copy numbers shown in **Table 14 and Figure 42**) with a few

genes in some samples not showing copy levels above the negative RT background or showing

copy levels below the limit-of-detection of ddPCR (**Figure 42**) (limit-of-detection empirically

determined as 4 copies [240]).

Table 14. ddPCR total copies from one healthy and one breast cancer patient sample processed through EV-MAP. Example of ddPCR raw total copy counts from 20 µL PCR reactions from a healthy and patient sample using the shortened gene panel, with negative RT results subtracted. The limit of detection for ddPCR is 4 total copies. P5 patient information is provided in **Table A2** of the appendix.

	H2		P5	
	Anti-EpCAM	Anti-FAPα	Anti-EpCAM	Anti-FAPα
CK19	0	0	3.4	0
VIM	3.4	1.6	5	0
CD81	0	0	4.8	3

	Anti-EpCAM	Anti-FAPα
EpCAM	3.2	3.4
CK19	3.4	0
FAPv2	7.2	4.4
VIM	5	0
IL8	1.8	1.6
CD81	4.8	3
CD24	0.8	0
CD44	4.6	0

raw copies in 20 µL reaction

0   50%   max
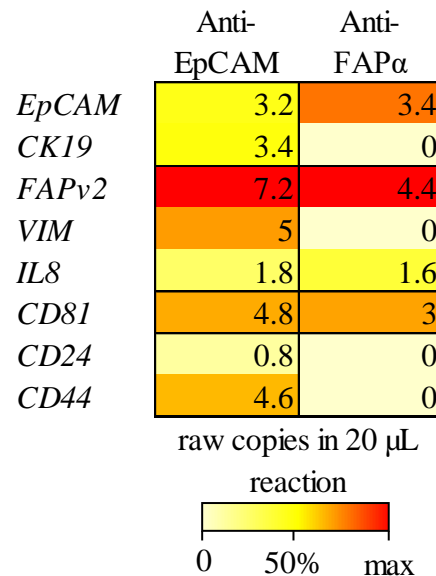
Figure 42. Full target gene panel from patient 5 (shown in **Table 14**).
Each column is scaled only to their own highest copy number. The copy numbers in the heat map refer to the total raw copies found in the 20 µL ddPCR reactions for each gene, with negative RT results subtracted. Several genes are shown below the limit of detection of droplet (>4 total copies).

Researchers have rarely performed transcriptome analysis of EVs compared to the breadth of studies analyzing the EV proteome. Several reasons exist as to why researchers have shied away from analyzing EV mRNA. Firstly, as discussed in Chapter 1, only up to 10% of EV TRNA is associated with any RNA species other than rRNA fragments, with only 0.25% of TRNA found to be mRNA when RNA sequencing was performed for glioma stem cell derived EVs[148]. Furthermore, most mRNA found in EVs is fragmented[133] and therefore may not properly amplify product after cDNA synthesis. Instead, most EV isolation research has focused on comparing the concentration of EVs between healthy and breast cancer patient samples [229, 241], particularly in developing microfluidic EV isolation platforms for clinical applications [128, 129, 242]. Only analyzing the quantity of EVs lacks clinical applicability compared to mRNA analysis because the FDA would need to approve the use of such a novel biomarker in addition to the new technology, requiring extensive clinical trials.

However, streamlining the new technology with a diagnostic test already used for a disease could automatically show clinical relevance. As an example, EV transcriptome analysis from immunoaffinity isolated EVs was chosen as the target of interest in this study because tests implementing mRNA expression analysis are already incorporated into clinical care for breast cancer management through FDA approved tests such as the Prosigna® or Oncotype DX® aforementioned in the molecular analysis section of Chapter 1.

Chapter 3. Summary and future directions

An extracellular vesicle microfluidic affinity purification (EV-MAP) device consisting of three beds serially connected and populated with micropillars was developed. Through Monte Carlo simulations incorporating convection, diffusional dynamics, and Ab-binding kinetics, the EV-MAP device theoretically achieved 80% recovery of EVs at the flow rate of 2.1 µL/min used in this study. For off-line EV analysis using TEM and NTA, a release procedure using 0.2% proteinase K and 10 min sonication was developed which proved to maintain the integrity of the EVs through no evidence of lysis and produce a release efficiency of 99 ±1%. Optimization of the EV-MAP assay for EV isolation required investigating the best blocking and washing buffer combination to mitigate nonspecific binding. A blocking buffer composition of 1% BSA/1% PVP-40 in PBS and washing buffer of 0.2% Tween 20® produced the lowest number of nonspecific NPs as assessed through an isotype immobilized device. It also increased the number of specific particles captured by $1x10^8$/mL when analyzed through NTA compared to other reagent combinations.

RT-ddPCR was performed on TRNA extracted from EVs isolated through the EV-MAP device to analyze mRNA expression profiles. EVs from Hs578T culture media conditioned in EV-depleted FBS showed similar mRNA profiles to that resulting from their cells of origin, suggesting that EVs could serve as an alternative or supplementary source of mRNA for breast cancer diagnosis currently implementing gene expression profiling for patient stratification and treatment decision-making. MCF7 EVs showed discordance from the MCF7 cell mRNA expression resulting in a combination of an epithelial and mesenchymal phenotype, suggesting that these mesenchymal genes may be preferentially packaged into MCF7 EVs compared to their cell of origin. The EV-MAP assay resulted in 99 ± 1% specificity to the target genes assessed through mRNA profiling of EVs from donor plasma by showing negligible gene copies resulting

from the isotype EV fraction. After optimizing the EV-MAP assay, healthy controls and patient samples were processed for mRNA expression profiling using RT-ddPCR. Extremely low copy numbers from both healthy control and disease plasma EVs were observed, with some genes either not showing above the negative RT background or not observed above the limit of detection for ddPCR (4 total copies or 0.2 copies/µL), suggesting that EVs may carry low masses of mRNA for the genes used in this study.

Studies have been conducted to characterize the TRNA populations packaged into EVs. Wei *et al.* characterized both small and long RNA species through RNA sequencing of EVs derived from glioma stem cells, and found ~10% of TRNA from EVs was non-rRNA, with mRNA accounting for only 0.25% of the EV TRNA population [148]. Further, based on NTA results and TRNA mass, it was observed that 4.45 ag of TRNA is packaged into each EV. Taking these mass considerations into account, the mass input and output through the EV-MAP assay was calculated using certain assumptions supported by the literature (**Figure 43**).

Through NTA results after EV release from the EV-MAP device(see **Figure 38**), an average of ~2×10^8 EVs were isolated from 500 µL of cell media. Assuming each EV contains 4.45 ag of TRNA and empirically determining the efficiency of the Direct-zol Microprep Kit (Zymo) to be 41%, only 356 pg of TRNA could be secured from 1 EV-MAP device. When considering the TRNA is eluted in 6.5 µL, this will result in a TRNA concentration of ~55 pg/µL. As noted above, the percentage of mRNA from TRNA found in an EV is 0.25%, which means that roughly 1 pg of mRNA will result from the EV-MAP assay. This is then diluted when added to the PCR cocktail, indicating *100,000 mRNA molecules may be extracted from 2×10^8*

EVs by assuming the average mRNA packaged into EVs is 500 nt, supported by the size distribution observed from EV TRNA extracted in this study (see **Figure 31**).
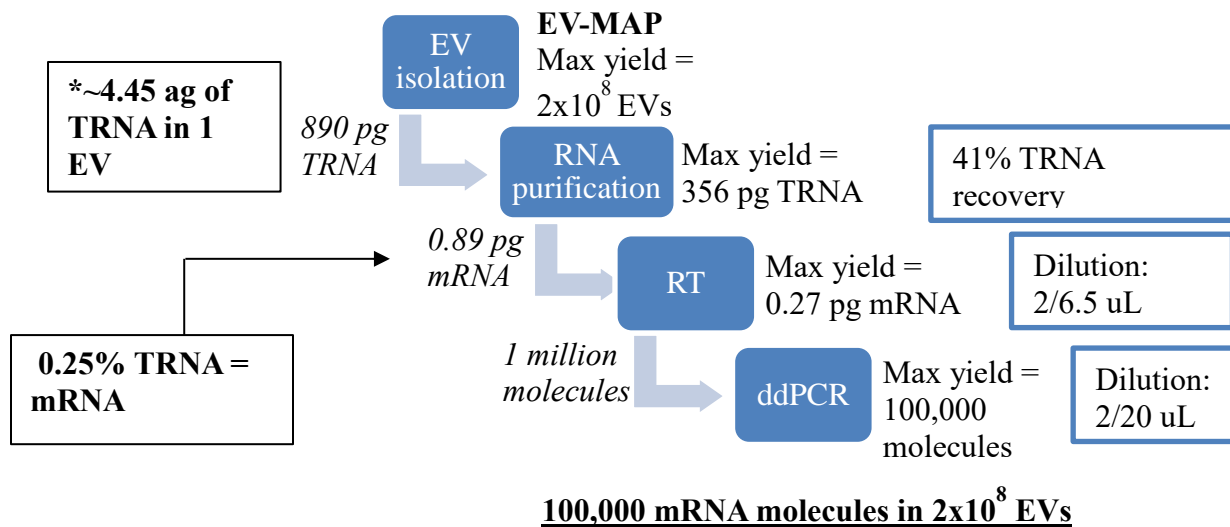

Figure 43. Flow chart depicting the mass yield from each step in the three-bed EV-MAP assay. Mass inputs and outputs through every step of the EV-MAP assay are calculated based on experimental results for the average number of EVs isolated through NTA (see **Figure 38**). From the number of EVs, the number of mRNA molecules can be calculated based upon the assumption that all mRNA is reverse transcribed into cDNA with 100% efficiency and an experimental study which found a single EV to hold ~ 4.5 ag of TRNA, with only 0.25% of EV TRNA amounting to mRNA[147]. These calculations were performed assuming the average mRNA molecule packaged into EVs is ~500 nt (see **Figure 31**). Finally, it is assumed that each ribonucleotide is ~ 330 g/mol. These calculations result in ~ 100,000 mRNA molecules from 2×10^8 EVs. The TRNA recovery using the Directzol Microprep kit (Zymo) was empirically determined to be 41%.

Relative expression results procured through RNA sequencing were procured from the Gene Expression Omnibus database for MCF7 cells and applied to the number of total mRNA molecules calculated from 10^8 EVs (**Table 15**). This relative expression data was also used to determine the relative expression of target genes used in the EV-MAP assay for a single cell. In both contexts, there are some genes that are expressed at low levels and potentially show as silent with current expression profiling technology. However, the significant difference in

number of particles (one cell vs. over 10 million EVs) with little change in gene expression further highlights the mass limitations experienced in analyzing mRNA packaged into EVs.

Table 15. mRNA expression of the target genes used for EV-MAP compared to the expression from a single cell. Using MCF7 cell line mRNA sequencing data procured from the open access Gene Expression Omnibus (GEO) database, relative expressions of genes from $2x10^8$ EVs were calculated. The ~ 100,000 mRNA molecules procured through EV-MAP are not evenly distributed among every gene, with some genes having such a low expression they could not be detected through conventional expression profiling methods such as ddPCR. Further, when comparing the amount of gene copies from $2x10^8$ EVs to the gene copies resulting from a single cell using the same RNA sequencing data, the low mass limitations of mRNA in EVs becomes apparent as even one cell produces higher expression. The estimated average number of mRNA molecules for a single cell was 360,000, according to Quiagen (https://www.qiagen.com/cn/resources/faq?id=06a192c2-e72d-42e8-9b40-3171e1eb4cb8&lang=en&Print=1).

Gene	Copy Number in 3-bed device	Copy Number in a _Single Cell_
EpCAM	22.5	159
CK19	154	1,086
FAP	0.028	0.199
VIM	0.21	1.47
IL8	0.025	0.174
CD81	9.81	69.2
CD24	92.6	653
CD44	7.75	54.7

One method of increasing the mRNA mass yield in the EV-MAP assay is to increase the amount of EVs captured. Another version of the EV-MAP device contains 7 beds connected in parallel for high-throughput processing and a ~ 6-fold increase in surface area to increase EV capacity compared to our existing 3-bed device (**Figure 44**). This correlates to >500,000 mRNA molecules as opposed to the 100,000 isolated from EV-MAP (**Table 16**). The device has a

surface area of 38.57 cm^2 with the same interpillar spacing of 10 µm designed for the EV-MAP

3-bed device (**Table 16**).

3-bed EV-MAP

7-bed EV-MAP (Biofluidica)
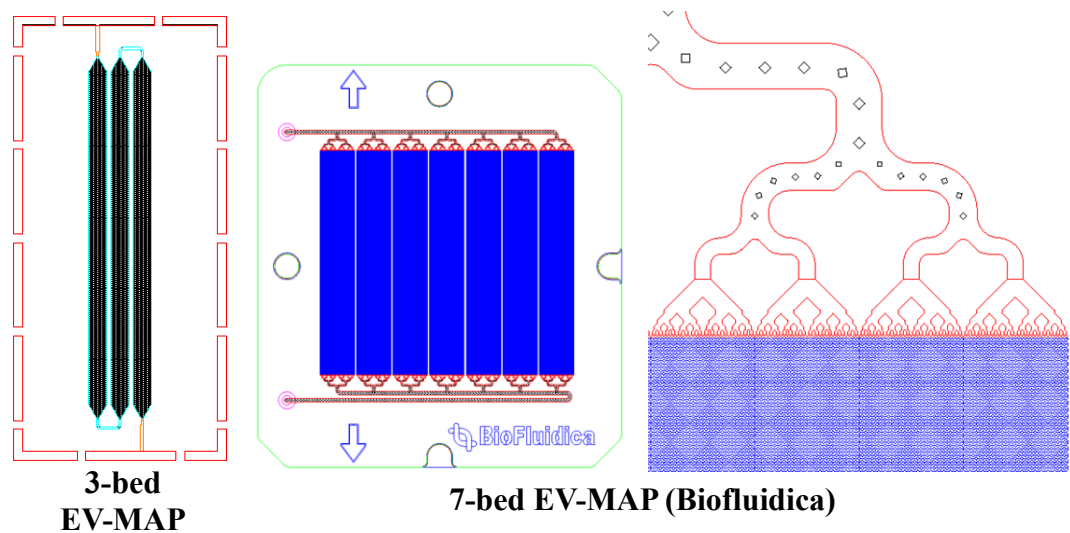
Figure 44. CAD schematics for the three-bed and seven-bed EV-MAP devices.
CAD schematics for the three-bed and seven-bed version of the EV-MAP device. Both contain beds populated with micropillars. However, the beds in the three-bed device are serially connected while the seven-bed device has them in parallel to increase the throughput. The fluid is split evenly between all seven beds.

Table 16. Design parameters for the 3-bed and 7-bed EV-MAP devices.
The 7-bed design of the EV-MAP device also consists of micropillar arrays with 10 um spacing in between. However, the surface area is greatly increased by a factor of ~6, similarly increasing the EV load capacity.

	EV-MAP (3-Bed)	EV-MAP (7-bed)
Surface Area (cm^2)	6.8	38.57
Number of pillars	15,202	1,475,712
Pillar dimensions	110 x 100 µm	10 x 10 x 50 µm
Pillar spacing	10 µm	
Average EV load	2×10^8	11.2×10^8
mRNA molecule yield	100,000	560,000

Another method to increase copy number is through amplification of mRNA post-processing. Whole transcriptome amplification (WTA) is a method of increasing cDNA by amplifying all mRNA molecules containing a poly-adenylated tail and can be performed on sample inputs as low as 100 fg. **Figure 45** shows a general outline of the WTA procedure. Firstly, WTA synthesizes cDNA from mRNA using anchored poly(dT) primers to anneal at the 3' poly-A tail. Terminal deoxynucleotidyl transferase (TdT) then adds dATPs to the 3' end of the cDNA. Exonuclease I treatment often precedes this step to degrade any competing ssDNA primers. A denaturation step separates the original mRNA template from the cDNA, allowing for a new batch of poly(dT) primers to anneal and extend the polyadenylated cDNA during PCR.
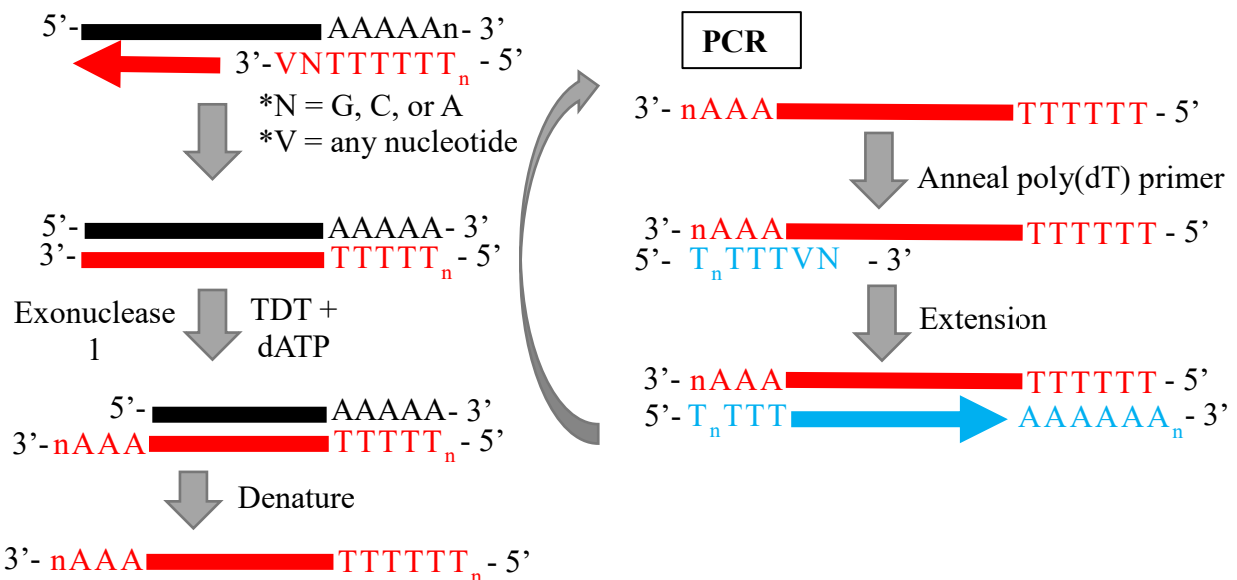

Figure 45. General steps for WTA procedure.
Lower case n = number of either tyrosine or adenine added onto the molecule, with subscript n's taking on a value based on the primer length used in the reactions. Black bar denotes mRNA, red denotes cDNA, and blue denotes PCR product. First, anchored poly(dT) primers anneal at the poly-A tail of mRNA to synthesize cDNA. Next, addition of Exonuclease I degrades remaining ssDNA primers that could anneal to the dATPs which are added to the 3' end of the cDNA products through TdT so the sequence of both ends of the cDNA is known. The mRNA template is denatured from the cDNA to create a ssDNA template for PCR which uses another round of poly(dT) primers. Overall, this procedure then takes all starting mRNA with a poly-A tail and amplifies it to increase the Yield of transcripts of low expression before traditional PCR using specific primers.

WTA was performed on mRNA to compare the copy results to standard cDNA synthesis (using Protoscript II, NEB). A combined TRNA mass of 17.1 µg from SKBR3 and MCF7 cells was purified to extract mRNA using the Dynabeads™ mRNA DIRECT™ purification kit (Invitrogen). Standard protocol was implemented with a few modifications, namely the inclusion of extra washing steps to ensure complete removal of remaining lithium dodecyl sulfate (LiDS) surfactant, known as a strong inhibitor for enzymatic reactions. Five-hundred pg of purified mRNA (recovered 173 ng mRNA in total or ~1% of TRNA) served as the starting material for both WTA that was carried out using the CellAmp™ Whole Transcriptome Amplification Kit Ver.2 (Takara) standard protocol and traditional cDNA synthesis or RT using the same kit previously mentioned for this study. Products were then submitted to ddPCR after diluting the RT or WTA material 30 times.

As suspected, the mRNA processed with WTA showed much higher copy numbers compared to cDNA synthesis alone (**Figure 46A**). More importantly, WTA did not bias the gene expression profile, showing the same expected epithelial genes to be highly expressed compared to mesenchymal phenotypic genes (**Figure 46B**). Copies from ddPCR were analyzed without normalizing to the input RNA as the same input masses were used for both procedures. In conclusion, WTA may increase input mass of target molecules otherwise present in low levels in EVs before performing ddPCR analysis.
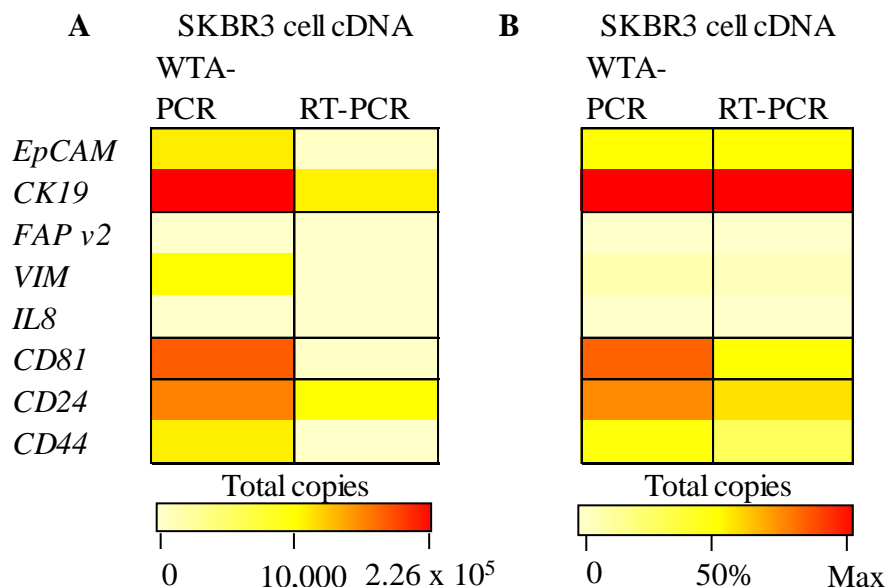
Figure 46. mRNA expression profiling of PCR products from WTA or cDNA from traditional RT. Each procedure started with 500pg of combined MCF7 and SKBR3 cell mRNA. Both procedures used Poly(dT) primers to synthesize cDNA from the poly-A tail of the mRNA. However, the WTA procedure also amplifies all cDNA synthesized from mRNA prior to the ddPCR. **(A)** Comparison of total copies produced after ddPCR of either the WTA or RT product, highlighting the higher expressions resulting from WTA vs. traditional RT. The color scale bar is based on the gene of highest expression within the entire panel. **(B)** Total copy data from both procedures analyzed separately to distinguish any differences in the expression profiles. WTA does not significantly affect the gene expression profiles, with expected epithelial genes still highly abundant and mesenchymal genes relatively silent. Each column is scaled to each procedure's gene of highest expression thereby producing a percentage.

Future work should also include the translation of EV-MAP into currently FDA-approved gene expression profiling tests. The gene panel chosen for this study was designed based on orthogonal markers distinguishing mesenchymal and epithelial phenotypes, as the antibodies implemented captured these two distinct expression profiles and previous studies had used these genes to assess CTC molecular profiles from breast cancer patients, finding clinical significance in assessing both for treatment response or monitoring treatment[98]. The selection and expression of EVs based on phenotype was also chosen because the breast cancer intrinsic

subtypes may be differentiated using these same phenotypes, with claudin-low showing a mesenchymal phenotype and Luminal A or B associated with a luminal epithelial phenotype.

However, these genes are not included in the FDA-approved Prosigna® and Oncotype Dx® test. Therefore, it would be critical to isolate EV TRNA using EV-MAP for mRNA expression profiling of the genes used in these tests. The Prosigna® assay uses the PAM50 gene panel and five reference genes, while the Oncotype Dx® tests only 16 genes specifically associated with proliferation and the invasive nature of cells [243], most of which are included in the PAM50 panel, and 5 reference genes.

To discuss one of the assays in further detail, the Prosigna® assay provides gene expression results through the relative abundance of mRNA transcripts. Fluorescent reporter probes and capture probes are hybridized to the TRNA. These captured transcripts are immobilized on a cartridge surface for clear detection of the barcode distinct to each reporter probe by nanoString nCounter technology. Prosigna® requires at least 12.5 ng/µL of TRNA from formalin fixed parrafin embedded tumor tissue to successfully perform the assay, thereby making the increase of EV mRNA yield either through the seven-bed EV-MAP device or through WTA critical as an initial future step.

Bibliography

1.   Bray, F., et al., *Global cancer statistics 2018: GLOBOCAN estimates of incidence and mortality worldwide for 36 cancers in 185 countries.* CA: a cancer journal for clinicians, 2018. **68**(6): p. 394-424.
2.   Murphy, S.L., et al., *Mortality in the United States, 2017.* 2018.
3.   Siegel, R.L., K.D. Miller, and A. Jemal, *Cancer statistics, 2019.* CA: a cancer journal for clinicians, 2019.
4.   *Cancer Classification*. SEER Training Modules 2018 [cited 2018 December 3]; Available from: https://training.seer.cancer.gov/disease/categories/classification.html.
5.   *Breast Cancer Facts and Figures 2017-2018*. 2017, American Cancer Society, Inc.: Atlanta.
6.   DeSantis, C.E., et al., *Breast cancer statistics, 2017, racial disparity in mortality by state.* CA: a cancer journal for clinicians, 2017. **67**(6): p. 439-448.
7.   *Types of Breast Cancer | Different Breast Cancer Types*. 2019 [cited 2019 6 Jan]; Available from: https://www.cancer.org/cancer/breast-cancer/understanding-a-breast-cancer-diagnosis/types-of-breast-cancer.html.
8.   Boyd, N.F., et al., *Mammographic density and the risk and detection of breast cancer.* New England Journal of Medicine, 2007. **356**(3): p. 227-236.
9.   Pisano, E.D., et al., *Diagnostic accuracy of digital versus film mammography: exploratory analysis of selected population subgroups in DMIST.* Radiology, 2008. **246**(2): p. 376-383.
10.   Kuchenbaecker, K.B., et al., *Risks of breast, ovarian, and contralateral breast cancer for BRCA1 and BRCA2 mutation carriers.* Jama, 2017. **317**(23): p. 2402-2416.
11.   Siu, A.L., *Screening for breast cancer: US Preventive Services Task Force recommendation statement.* Annals of internal medicine, 2016. **164**(4): p. 279-296.
12.   Oeffinger, K.C., et al., *Breast cancer screening for women at average risk: 2015 guideline update from the American Cancer Society.* Jama, 2015. **314**(15): p. 1599-1614.
13.   Lee, C.H., et al., *Breast cancer screening with imaging: recommendations from the Society of Breast Imaging and the ACR on the use of mammography, breast MRI, breast ultrasound, and other technologies for the detection of clinically occult breast cancer.* Journal of the American college of radiology, 2010. **7**(1): p. 18-27.
14.   Lehman, C.D., et al., *National performance benchmarks for modern screening digital mammography: update from the Breast Cancer Surveillance Consortium.* Radiology, 2016. **283**(1): p. 49-58.
15.   (BCSC), B.C.S.C. *Performance measures for 1,838,372 screening mammography examinations from 2004 to 2008 by age -- based on BCSC data through 2009*. June 2016 [cited 2019 18 Feb]; Available from: http://www.bcsc-research.org/statistics/performance/screening/2009/perf_age.html.
16.   Berg, W., et al., *Frequently asked questions about mammography and the USPSTF recommendations: a guide for practitioners.* Reston: Society of Breast Imaging, 2009.
17.   Sree, S.V., et al., *Breast imaging: a survey.* World journal of clinical oncology, 2011. **2**(4): p. 171.
18.   Kolb, T.M., J. Lichy, and J.H. Newhouse, *Comparison of the performance of screening mammography, physical examination, and breast US and evaluation of factors that*

influence them: an analysis of 27,825 patient evaluations. Radiology, 2002. **225**(1): p. 165-175.

19.   Scheel, J.R., et al., *Screening ultrasound as an adjunct to mammography in women with mammographically dense breasts.* American journal of obstetrics and gynecology, 2015. **212**(1): p. 9-17.

20.   Berg, W.A., et al., *Detection of breast cancer with addition of annual screening ultrasound or a single screening MRI to mammography in women with elevated breast cancer risk.* Jama, 2012. **307**(13): p. 1394-1404.

21.   Giger, M.L., et al., *Automated breast ultrasound in breast cancer screening of women with dense breasts: reader study of mammography-negative and mammography-positive cancers.* American Journal of Roentgenology, 2016. **206**(6): p. 1341-1350.

22.   Tagliafico, A.S., et al., *Adjunct screening with tomosynthesis or ultrasound in women with mammography-negative dense breasts: interim report of a prospective comparative trial.* J Clin Oncol, 2016. **34**(16): p. 1882-1888.

23.   Kriege, M., et al., *Efficacy of MRI and mammography for breast-cancer screening in women with a familial or genetic predisposition.* New England Journal of Medicine, 2004. **351**(5): p. 427-437.

24.   Kuhl, C.K., et al., *Mammography, breast ultrasound, and magnetic resonance imaging for surveillance of women at high familial risk for breast cancer.* Journal of clinical oncology, 2005. **23**(33): p. 8469-8476.

25.   Hagen, A.I., et al., *Sensitivity of MRI versus conventional screening in the diagnosis of BRCA-associated breast cancer in a national prospective series.* The breast, 2007. **16**(4): p. 367-374.

26.   Warner, E., et al., *Surveillance of BRCA1 and BRCA2 mutation carriers with magnetic resonance imaging, ultrasound, mammography, and clinical breast examination.* Jama, 2004. **292**(11): p. 1317-1325.

27.   Elmore, J.G., et al., *Screening for breast cancer.* Jama, 2005. **293**(10): p. 1245-1256.

28.   Kuhl, C.K., et al., *Breast MR imaging screening in 192 women proved or suspected to be carriers of a breast cancer susceptibility gene: preliminary results.* Radiology, 2000. **215**(1): p. 267-279.

29.   Tilanus-Linthorst, M.M., et al., *First experiences in screening women at high risk for breast cancer with MR imaging.* Breast cancer research and treatment, 2000. **63**(1): p. 53-60.

30.   Morris, E.A., et al., *MRI of occult breast carcinoma in a high-risk population.* American Journal of Roentgenology, 2003. **181**(3): p. 619-626.

31.   Podo, F., et al., *The Italian multi-centre project on evaluation of MRI and other imaging modalities in early detection of breast cancer in subjects at high genetic risk.* Journal of experimental & clinical cancer research: CR, 2002. **21**(3 Suppl): p. 115-124.

32.   Lo, G., et al., *Evaluation of the utility of screening mammography for high-risk women undergoing screening breast MR imaging.* Radiology, 2017. **285**(1): p. 36-43.

33.   Kuhl, C., et al., *Prospective multicenter cohort study to refine management recommendations for women at elevated familial risk of breast cancer: the EVA trial.* J Clin Oncol, 2010. **28**(9): p. 1450-1457.

34.   van Zelst, J.C., et al., *Surveillance of women with the BRCA 1 or BRCA 2 mutation by using biannual automated breast US, MR imaging, and mammography.* Radiology, 2017. **285**(2): p. 376-388.

35. Riedl, C.C., et al., *Triple-modality screening trial for familial breast cancer underlines the importance of magnetic resonance imaging and questions the role of mammography and ultrasound regardless of patient mutation status, age, and breast density.* Journal of Clinical Oncology, 2015. **33**(10): p. 1128.

36. Bevers, T.B., et al., *Breast Cancer Screening and Diagnosis, Version 3.2018, NCCN Clinical Practice Guidelines in Oncology.* Journal of the National Comprehensive Cancer Network, 2018. **16**(11): p. 1362-1389.

37. Flobbe, K., et al., *The additional diagnostic value of ultrasonography in the diagnosis of breast cancer.* Archives of internal medicine, 2003. **163**(10): p. 1194-1199.

38. Duijm, L., et al., *Sensitivity, specificity and predictive values of breast imaging in the detection of cancer.* British journal of cancer, 1997. **76**(3): p. 377.

39. Bahl, M., et al., *Evaluation of pathologic nipple discharge: what is the added diagnostic value of MRI?* Annals of surgical oncology, 2015. **22**(3): p. 435-441.

40. Morrogh, M., et al., *MRI identifies otherwise occult disease in select patients with Paget disease of the nipple.* Journal of the American College of Surgeons, 2008. **206**(2): p. 316-321.

41. Renz, D.M., et al., *Inflammatory breast carcinoma in magnetic resonance imaging: a comparison with locally advanced breast cancer.* Academic radiology, 2008. **15**(2): p. 209-221.

42. Giuliano, A.E., et al., *Breast cancer—major changes in the American Joint Committee on Cancer eighth edition cancer staging manual.* CA: a cancer journal for clinicians, 2017. **67**(4): p. 290-303.

43. Lyman, G.H., et al., *Sentinel lymph node biopsy for patients with early-stage breast cancer: American Society of Clinical Oncology clinical practice guideline update.* Journal of Clinical Oncology, 2016.

44. Gradishar, W.J., et al., *Invasive breast cancer version 1.2016, NCCN clinical practice guidelines in oncology.* Journal of the National Comprehensive Cancer Network, 2016. **14**(3): p. 324-354.

45. Louie, R.J., et al., *Complete blood counts, liver function tests, and chest x-rays as routine screening in early-stage breast cancer: value added or just cost?* Breast cancer research and treatment, 2015. **154**(1): p. 99-103.

46. Amin, M.B., et al., *AJCC Cancer Staging Manual.* eighth ed. 2017: Springer International Publishing. 1032.

47. Lang, J.E., et al., *Molecular markers for breast cancer diagnosis, prognosis and targeted therapy.* Journal of surgical oncology, 2015. **111**(1): p. 81-90.

48. Perou, C.M., et al., *Molecular portraits of human breast tumours.* nature, 2000. **406**(6797): p. 747.

49. Sørlie, T., et al., *Gene expression patterns of breast carcinomas distinguish tumor subclasses with clinical implications.* Proceedings of the National Academy of Sciences, 2001. **98**(19): p. 10869-10874.

50. Herschkowitz, J.I., et al., *Identification of conserved gene expression features between murine mammary carcinoma models and human breast tumors.* Genome biology, 2007. **8**(5): p. R76.

51. Hyun, K.-A., et al., *Epithelial-to-mesenchymal transition leads to loss of EpCAM and different physical properties in circulating tumor cells from metastatic breast cancer.* Oncotarget, 2016. **7**(17): p. 24677.

52.   Kalluri, R. and R.A. Weinberg, *The basics of epithelial-mesenchymal transition.* The Journal of clinical investigation, 2009. **119**(6): p. 1420-1428.
53.   Liu, F., et al., *Fibroblast activation protein overexpression and clinical implications in solid tumors: a meta-analysis.* PloS one, 2015. **10**(3): p. e0116683.
54.   Weinberg, R., *The biology of cancer*. 2013: Garland science. 796.
55.   Prat, A. and C.M. Perou, *Deconstructing the molecular portraits of breast cancer.* Molecular oncology, 2011. **5**(1): p. 5-23.
56.   Dai, X., et al., *Breast cancer intrinsic subtype classification, clinical use and future trends.* American journal of cancer research, 2015. **5**(10): p. 2929.
57.   Parker, J.S., et al., *Supervised risk predictor of breast cancer based on intrinsic subtypes.* Journal of clinical oncology, 2009. **27**(8): p. 1160.
58.   Prat, A., et al., *Phenotypic and molecular characterization of the claudin-low intrinsic subtype of breast cancer.* Breast cancer research, 2010. **12**(5): p. R68.
59.   *Prosigna® | NanoString Technologies*. 2019 [cited 2019 060319]; Available from: https://www.nanostring.com/diagnostics/prosigna.
60.   Yersal, O. and S. Barutca, *Biological subtypes of breast cancer: Prognostic and therapeutic implications.* World journal of clinical oncology, 2014. **5**(3): p. 412.
61.   Albain, K.S., et al., *Prognostic and predictive value of the 21-gene recurrence score assay in postmenopausal women with node-positive, oestrogen-receptor-positive breast cancer on chemotherapy: a retrospective analysis of a randomised trial.* The lancet oncology, 2010. **11**(1): p. 55-65.
62.   Harris, L., et al., *American Society of Clinical Oncology 2007 update of recommendations for the use of tumor markers in breast cancer.* Journal of clinical oncology, 2007. **25**(33): p. 5287-5312.
63.   McDonald, E.S., et al., *Clinical diagnosis and management of breast cancer.* J Nucl Med, 2016. **57**(Suppl 1): p. 9S-16S.
64.   Jatoi, I. and M.A. Proschan, *Randomized trials of breast-conserving therapy versus mastectomy for primary breast cancer: a pooled analysis of updated results.* American journal of clinical oncology, 2005. **28**(3): p. 289-294.
65.   Meisel, J.L., et al., *Evolution of Targeted Therapy in Breast Cancer: Where Precision Medicine Began.* American Society of Clinical Oncology Educational Book, 2018. **38**: p. 78-86.
66.   Osborne, C.K., *Tamoxifen in the treatment of breast cancer.* New England Journal of Medicine, 1998. **339**(22): p. 1609-1618.
67.   Harris, M., *Monoclonal antibodies as therapeutic agents for cancer.* The lancet oncology, 2004. **5**(5): p. 292-302.
68.   Khatcheressian, J.L., et al., *Breast cancer follow-up and management after primary treatment: American Society of Clinical Oncology clinical practice guideline update.* J Clin Oncol [internet], 2012.
69.   De Bock, G., et al., *Effectiveness of routine visits and routine tests in detecting isolated locoregional recurrences after treatment for early-stage invasive breast cancer: a meta-analysis and systematic review.* Journal of Clinical Oncology, 2004. **22**(19): p. 4010-4018.
70.   Graham, L.J., et al., *Current approaches and challenges in monitoring treatment responses in breast cancer.* Journal of Cancer, 2014. **5**(1): p. 58.

71.   Hamaoka, T., et al., *Bone imaging in metastatic breast cancer.* Journal of Clinical Oncology, 2004. **22**(14): p. 2942-2953.

72.   Robbins, J.B. and M.A. Pozniak, *Contrast media tutorial.* Reston, VA: American College of Radiology, 2010.

73.   Grassetto, G., et al., *18F-FDG-PET/CT in patients with breast cancer and rising Ca 15-3 with negative conventional imaging: a multicentre study.* European journal of radiology, 2011. **80**(3): p. 828-833.

74.   Groheux, D., et al., *Performance of FDG PET/CT in the clinical management of breast cancer.* Radiology, 2013. **266**(2): p. 388-405.

75.   Erdi, Y.E., *Limits of tumor detectability in nuclear medicine and PET.* Molecular imaging and radionuclide therapy, 2012. **21**(1): p. 23.

76.   Wilms, G., et al., *Spiral CT of cerebral aneurysms.* Journal belge de radiologie, 1995. **78**(2): p. 75-78.

77.   Bedard, P.L., et al., *Tumour heterogeneity in the clinic.* Nature, 2013. **501**(7467): p. 355.

78.   Brooks, J.D., *Translational genomics: the challenge of developing cancer biomarkers.* Genome research, 2012. **22**(2): p. 183-187.

79.   Carlson, R.W., et al., *Metastatic breast cancer, version 1.2012 featured updates to the nccn guidelines.* Journal of the National Comprehensive Cancer Network, 2012. **10**(7): p. 821-829.

80.   Lin, D.C. and J.R. Genzen, *Concordance analysis of paired cancer antigen (CA) 15-3 and 27.29 testing.* Breast cancer research and treatment, 2018. **167**(1): p. 269-276.

81.   Tondini, C., et al., *Comparison of CA15-3 and carcinoembryonic antigen in monitoring the clinical course of patients with metastatic breast cancer.* Cancer research, 1988. **48**(14): p. 4107-4112.

82.   Mavroudis, D., *Circulating cancer cells.* Annals of Oncology, 2010. **21**(suppl_7): p. vii95-vii100.

83.   Pantel, K. and C. Alix-Panabières, *Circulating tumour cells in cancer patients: challenges and perspectives.* Trends in molecular medicine, 2010. **16**(9): p. 398-406.

84.   Allard, W.J., et al., *Tumor cells circulate in the peripheral blood of all major carcinomas but not in healthy subjects or patients with nonmalignant diseases.* Clinical cancer research, 2004. **10**(20): p. 6897-6904.

85.   Alix-Panabières, C. and K. Pantel, *Clinical applications of circulating tumor cells and circulating tumor DNA as liquid biopsy.* Cancer discovery, 2016. **6**(5): p. 479-491.

86.   Bardelli, A. and K. Pantel, *Liquid biopsies, what we do not know (yet).* Cancer cell, 2017. **31**(2): p. 172-179.

87.   Lv, Q., et al., *Prognostic value of circulating tumor cells in metastatic breast cancer: a systemic review and meta-analysis.* Clinical and Translational Oncology, 2016. **18**(3): p. 322-330.

88.   Zhang, W., et al., *Liquid biopsy for cancer: circulating tumor cells, circulating free DNA or exosomes?* Cellular Physiology and Biochemistry, 2017. **41**(2): p. 755-768.

89.   Bidard, F.-C., et al., *Clinical validity of circulating tumour cells in patients with metastatic breast cancer: a pooled analysis of individual patient data.* The Lancet Oncology, 2014. **15**(4): p. 406-414.

90.   Zhang, L., et al., *Meta-analysis of the prognostic value of circulating tumor cells in breast cancer.* Clinical cancer research, 2012. **18**(20): p. 5701-5710.

91.   Ignatiadis, M., et al., *Different prognostic value of cytokeratin-19 mRNA-positive circulating tumor cells according to estrogen receptor and HER2 status in early-stage breast cancer.* Journal of clinical oncology, 2007. **25**(33): p. 5194-5202.

92.   Pierga, J.-Y., et al., *Circulating tumor cell detection predicts early metastatic relapse after neoadjuvant chemotherapy in large operable and locally advanced breast cancer in a phase II randomized trial.* Clinical Cancer Research, 2008. **14**(21): p. 7004-7010.

93.   Lucci, A., et al., *Circulating tumour cells in non-metastatic breast cancer: a prospective study.* The lancet oncology, 2012. **13**(7): p. 688-695.

94.   Rack, B., et al., *Circulating tumor cells predict survival in early average-to-high risk breast cancer patients.* Journal of the National Cancer Institute, 2014. **106**(5): p. dju066.

95.   Jackson, J.M., et al., *Materials and microfluidics: enabling the efficient isolation and analysis of circulating tumour cells.* Chemical Society Reviews, 2017. **46**(14): p. 4245-4280.

96.   Smerage, J.B., et al., *Circulating tumor cells and response to chemotherapy in metastatic breast cancer: SWOG S0500.* Journal of Clinical Oncology, 2014. **32**(31): p. 3483.

97.   Grover, P., et al., *Circulating tumour cells: the evolving concept and the inadequacy of their enrichment by EpCAM-based methodology for basic and clinical cancer research.* Annals of Oncology, 2014. **25**(8): p. 1506-1516.

98.   Witek, M.A., et al., *Discrete microfluidics for the isolation of circulating tumor cell subpopulations targeting fibroblast activation protein alpha and epithelial cell adhesion molecule.* NPJ precision oncology, 2017. **1**(1): p. 24.

99.   Leon, S., et al., *Free DNA in the serum of cancer patients and the effect of therapy.* Cancer research, 1977. **37**(3): p. 646-650.

100.   Zeerleder, S., *The struggle to detect circulating DNA.* Critical Care, 2006. **10**(3): p. 142.

101.   Brock, G., et al., *Liquid biopsy for cancer screening, patient stratification and monitoring.* Translational Cancer Research, 2015. **4**(3): p. 280-290.

102.   Toy, W., et al., *ESR1 ligand-binding domain mutations in hormone-resistant breast cancer.* Nature genetics, 2013. **45**(12): p. 1439.

103.   Paoletti, C., et al., *Development of circulating tumor cell-endocrine therapy index in patients with hormone receptor–positive breast cancer.* Clinical Cancer Research, 2015. **21**(11): p. 2487-2498.

104.   Chu, D., et al., *ESR1 mutations in circulating plasma tumor DNA from metastatic breast cancer patients.* Clinical cancer research, 2016. **22**(4): p. 993-999.

105.   Guttery, D.S., et al., *Noninvasive detection of activating estrogen receptor 1 (ESR1) mutations in estrogen receptor–positive metastatic breast cancer.* Clinical chemistry, 2015. **61**(7): p. 974-982.

106.   Schiavon, G., et al., *Analysis of ESR1 mutation in circulating tumor DNA demonstrates evolution during therapy for metastatic breast cancer.* Science translational medicine, 2015. **7**(313): p. 313ra182-313ra182.

107.   Cui, J., et al., *Cross-talk between HER2 and MED1 regulates tamoxifen resistance of human breast cancer cells.* Cancer research, 2012. **72**(21): p. 5625-5634.

108.   Murtaza, M., et al., *Non-invasive analysis of acquired resistance to cancer therapy by sequencing of plasma DNA.* Nature, 2013. **497**(7447): p. 108.

109.   Bosch, A., et al., *PI3K inhibition results in enhanced estrogen receptor function and dependence in hormone receptor–positive breast cancer.* Science translational medicine, 2015. **7**(283): p. 283ra51-283ra51.

110.   Garcia-Murillas, I., et al., *Mutation tracking in circulating tumor DNA predicts relapse in early breast cancer.* Science translational medicine, 2015. **7**(302): p. 302ra133-302ra133.

111.   Olsson, E., et al., *Serial monitoring of circulating tumor DNA in patients with primary breast cancer for detection of occult metastatic disease.* EMBO molecular medicine, 2015. **7**(8): p. 1034-1047.

112.   Dawson, S.-J., et al., *Analysis of circulating tumor DNA to monitor metastatic breast cancer.* New England Journal of Medicine, 2013. **368**(13): p. 1199-1209.

113.   Bettegowda, C., et al., *Detection of circulating tumor DNA in early-and late-stage human malignancies.* Science translational medicine, 2014. **6**(224): p. 224ra24-224ra24.

114.   Chaput, N. and C. Théry. *Exosomes: immune properties and potential clinical implementations*. in *Seminars in immunopathology*. 2011. Springer.

115.   Skog, J., et al., *Glioblastoma microvesicles transport RNA and proteins that promote tumour growth and provide diagnostic biomarkers.* Nature cell biology, 2008. **10**(12): p. 1470.

116.   Szajnik, M., et al., *Tumor-derived microvesicles induce, expand and up-regulate biological activities of human regulatory T cells (Treg).* PloS one, 2010. **5**(7): p. e11469.

117.   Costa-Silva, B., et al., *Pancreatic cancer exosomes initiate pre-metastatic niche formation in the liver.* Nature cell biology, 2015. **17**(6): p. 816.

118.   Contreras-Naranjo, J.C., H.-J. Wu, and V.M. Ugaz, *Microfluidics for exosome isolation and analysis: enabling liquid biopsy for personalized medicine.* Lab on a Chip, 2017. **17**(21): p. 3558-3577.

119.   Jansen, F., G. Nickenig, and N. Werner, *Extracellular vesicles in cardiovascular disease: potential applications in diagnosis, prognosis, and epidemiology.* Circulation research, 2017. **120**(10): p. 1649-1657.

120.   Gustafson, D., S. Veitch, and J.E. Fish, *Extracellular vesicles as protagonists of diabetic cardiovascular pathology.* Frontiers in cardiovascular medicine, 2017. **4**: p. 71.

121.   Im, H., et al., *Label-free detection and molecular profiling of exosomes with a nano-plasmonic sensor.* Nature biotechnology, 2014. **32**(5): p. 490.

122.   Jenjaroenpun, P., et al., *Characterization of RNA in exosomes secreted by human breast cancer cell lines using next-generation sequencing.* PeerJ, 2013. **1**: p. e201.

123.   Zhang, J., et al., *Exosome and exosomal microRNA: trafficking, sorting, and function.* Genomics, proteomics & bioinformatics, 2015. **13**(1): p. 17-24.

124.   Hannafon, B.N., et al., *Plasma exosome microRNAs are indicative of breast cancer.* Breast Cancer Research, 2016. **18**(1): p. 90.

125.   Eichelser, C., et al., *Increased serum levels of circulating exosomal microRNA-373 in receptor-negative breast cancer patients.* Oncotarget, 2014. **5**(20): p. 9650.

126.   Moon, P.-G., et al., *Fibronectin on circulating extracellular vesicles as a liquid biopsy to detect breast cancer.* Oncotarget, 2016. **7**(26): p. 40189.

127.   Moon, P.-G., et al., *Identification of developmental endothelial locus-1 on circulating extracellular vesicles as a novel biomarker for early breast cancer detection.* Clinical Cancer Research, 2016. **22**(7): p. 1757-1766.

128.   Sina, A.A.I., et al., *Real time and label free profiling of clinically relevant exosomes.* Scientific reports, 2016. **6**: p. 30460.

129.   Fang, S., et al., *Clinical application of a microfluidic chip for immunocapture and quantification of circulating exosomes to assist breast cancer diagnosis and molecular classification.* PLoS One, 2017. **12**(4): p. e0175050.

130. Nilsson, J., et al., *Prostate cancer-derived urine exosomes: a novel approach to biomarkers for prostate cancer.* British journal of cancer, 2009. **100**(10): p. 1603.

131. Hong, B.S., et al., *Colorectal cancer cell-derived microvesicles are enriched in cell cycle-related mRNAs that promote proliferation of endothelial cells.* BMC genomics, 2009. **10**(1): p. 556.

132. Chen, W.W., et al., *BEAMing and droplet digital PCR analysis of mutant IDH1 mRNA in glioma patient serum and cerebrospinal fluid extracellular vesicles.* Molecular Therapy-Nucleic Acids, 2013. **2**.

133. Valadi, H., *Exosome-mediated transfer of mRNAs and microRNAs is a novel mechanism of genetic exchange between cells.* Nature cell biology. **9**(6): p. 654-659.

134. Keup, C., et al., *RNA Profiles of Circulating Tumor Cells and Extracellular Vesicles for Therapy Stratification of Metastatic Breast Cancer Patients.* Clinical Chemistry, 2018. **64**(7): p. 1054-1062.

135. Yáñez-Mó, M., et al., *Biological properties of extracellular vesicles and their physiological functions.* Journal of extracellular vesicles, 2015. **4**(1): p. 27066.

136. van Niel, G., G. D'Angelo, and G. Raposo, *Shedding light on the cell biology of extracellular vesicles.* Nature reviews Molecular cell biology, 2018. **19**(4): p. 213.

137. Kalra, H., G. Drummen, and S. Mathivanan, *Focus on extracellular vesicles: introducing the next small big thing.* International journal of molecular sciences, 2016. **17**(2): p. 170.

138. Akers, J.C., et al., *Biogenesis of extracellular vesicles (EV): exosomes, microvesicles, retrovirus-like vesicles, and apoptotic bodies.* Journal of neuro-oncology, 2013. **113**(1): p. 1-11.

139. Van Engeland, M., et al., *Annexin V-affinity assay: a review on an apoptosis detection system based on phosphatidylserine exposure.* Cytometry: The Journal of the International Society for Analytical Cytology, 1998. **31**(1): p. 1-9.

140. Bergsmedh, A., et al., *Horizontal transfer of oncogenes by uptake of apoptotic bodies.* Proceedings of the National Academy of Sciences, 2001. **98**(11): p. 6407-6411.

141. Zernecke, A., et al., *Delivery of microRNA-126 by apoptotic bodies induces CXCL12-dependent vascular protection.* Sci. Signal., 2009. **2**(100): p. ra81-ra81.

142. Berda-Haddad, Y., et al., *Sterile inflammation of endothelial cell-derived apoptotic bodies is mediated by interleukin-1α.* Proceedings of the National Academy of Sciences, 2011. **108**(51): p. 20684-20689.

143. Vlassov, A.V., et al., *Exosomes: current knowledge of their composition, biological functions, and diagnostic and therapeutic potentials.* Biochimica et Biophysica Acta (BBA)-General Subjects, 2012. **1820**(7): p. 940-948.

144. Saiz, M.L., V. Rocha-Perugini, and F. Sánchez-Madrid, *Tetraspanins as organizers of antigen-presenting cell function.* Frontiers in immunology, 2018. **9**.

145. Li, M. and M. Li, *Analysis of the RNA content of the exosomes derived from blood serum and urine and its potential as biomarkers.* Philosophical transactions. Biological sciences. **369**(1652): p. 20130502-20130508.

146. Huang, X., et al., *Characterization of human plasma-derived exosomal RNAs by deep sequencing.* BMC genomics, 2013. **14**(1): p. 319.

147. Crescitelli, R., et al., *Distinct RNA profiles in subpopulations of extracellular vesicles: apoptotic bodies, microvesicles and exosomes.* Journal of extracellular vesicles, 2013. **2**(1): p. 20677.

148.   Wei, Z., et al., *Coding and noncoding landscape of extracellular RNA released by human glioma stem cells.* Nature communications, 2017. **8**(1): p. 1145.

149.   Théry, C., et al., *Isolation and characterization of exosomes from cell culture supernatants and biological fluids.* Current protocols in cell biology, 2006. **30**(1): p. 3.22. 1-3.22. 29.

150.   Muralidharan-Chari, V., et al., *ARF6-regulated shedding of tumor cell-derived plasma membrane microvesicles.* Current Biology, 2009. **19**(22): p. 1875-1885.

151.   Pospichalova, V., et al., *Simplified protocol for flow cytometry analysis of fluorescently labeled exosomes and microvesicles using dedicated flow cytometer.* Journal of extracellular vesicles, 2015. **4**(1): p. 25530.

152.   Campos, C.D., et al., *Molecular Profiling of Liquid Biopsy Samples for Precision Medicine.* The Cancer Journal, 2018. **24**(2): p. 93-103.

153.   Lobb, R.J., et al., *Optimized exosome isolation protocol for cell culture supernatant and human plasma.* Journal of extracellular vesicles, 2015. **4**(1): p. 27031.

154.   Lucchetti, D., A. Fattorossi, and A. Sgambato, *Extracellular vesicles in oncology: progress and pitfalls in the methods of isolation and analysis.* Biotechnology journal, 2019. **14**(1): p. 1700716.

155.   Sáenz-Cuesta, M., *Methods for extracellular vesicles isolation in a hospital setting.* Frontiers in immunology, 2015. **6**.

156.   Tauro, B.J., et al., *Comparison of ultracentrifugation, density gradient separation, and immunoaffinity capture methods for isolating human colon cancer cell line LIM1863-derived exosomes.* Methods, 2012. **56**(2): p. 293-304.

157.   Schey, K.L., J.M. Luther, and K.L. Rose, *Proteomics characterization of exosome cargo.* Methods, 2015. **87**: p. 75-82.

158.   Muller, L., et al., *Isolation of biologically-active exosomes from human plasma.* Journal of immunological methods, 2014. **411**: p. 55-65.

159.   Tanaka, Y., et al., *Clinical impact of serum exosomal microRNA-21 as a clinical biomarker in human esophageal squamous cell carcinoma.* Cancer, 2013. **119**(6): p. 1159-1167.

160.   Nordin, J.Z., et al., *Ultrafiltration with size-exclusion liquid chromatography for high yield isolation of extracellular vesicles preserving intact biophysical and functional properties.* Nanomedicine: Nanotechnology, Biology and Medicine, 2015. **11**(4): p. 879-883.

161.   Gercel-Taylor, C., et al., *Nanoparticle analysis of circulating cell-derived vesicles in ovarian cancer patients.* Analytical biochemistry, 2012. **428**(1): p. 44-53.

162.   Reátegui, E., et al., *Engineered nanointerfaces for microfluidic isolation and molecular profiling of tumor-specific extracellular vesicles.* Nature communications, 2018. **9**(1): p. 175.

163.   Arraud, N., et al., *Extracellular vesicles from blood plasma: determination of their morphology, size, phenotype and concentration.* Journal of Thrombosis and Haemostasis, 2014. **12**(5): p. 614-627.

164.   Dragovic, R.A., et al., *Sizing and phenotyping of cellular vesicles using Nanoparticle Tracking Analysis.* Nanomedicine: Nanotechnology, Biology and Medicine, 2011. **7**(6): p. 780-788.

165. Greening, D.W., et al., *A protocol for exosome isolation and characterization: evaluation of ultracentrifugation, density-gradient separation, and immunoaffinity capture methods*, in *Proteomic Profiling*. 2015, Springer. p. 179-209.

166. Taylor, D.D. and C. Gercel-Taylor, *MicroRNA signatures of tumor-derived exosomes as diagnostic biomarkers of ovarian cancer.* Gynecologic oncology, 2008. **110**(1): p. 13-21.

167. Mathivanan, S., et al., *Proteomics analysis of A33 immunoaffinity-purified exosomes released from the human colon tumor cell line LIM1215 reveals a tissue-specific protein signature.* Molecular & Cellular Proteomics, 2010. **9**(2): p. 197-208.

168. Koga, K., et al., *Purification, characterization and biological significance of tumor-derived exosomes.* Anticancer research, 2005. **25**(6A): p. 3703-3707.

169. Li, P., et al., *Progress in exosome isolation techniques.* Theranostics, 2017. **7**(3): p. 789.

170. Kalra, H., et al., *Comparative proteomics evaluation of plasma exosome isolation techniques and assessment of the stability of exosomes in normal human blood plasma.* Proteomics, 2013. **13**(22): p. 3354-3364.

171. Davies, R.T., et al., *Microfluidic filtration system to isolate extracellular vesicles from blood.* Lab on a chip, 2012. **12**(24): p. 5202-5210.

172. Cho, S., et al., *Isolation of extracellular vesicle from blood plasma using electrophoretic migration through porous membrane.* Sensors and Actuators B: Chemical, 2016. **233**: p. 289-297.

173. Woo, H.-K., et al., *Exodisc for rapid, size-selective, and efficient isolation and analysis of nanoscale extracellular vesicles from biological samples.* ACS nano, 2017. **11**(2): p. 1360-1370.

174. Liang, L.-G., et al., *An integrated double-filtration microfluidic device for isolation, enrichment and quantification of urinary extracellular vesicles for detection of bladder cancer.* Scientific reports, 2017. **7**: p. 46224.

175. Wang, Z., et al., *Ciliated micropillars for the microfluidic-based isolation of nanoscale lipid vesicles.* Lab on a Chip, 2013. **13**(15): p. 2879-2882.

176. Rahong, S., et al. *Ultrafast separation of small biomolecules by three-dimensional nanowire structure*. in *18th International Conference on Miniaturized Systems for Chemistry and Life Sciences, MicroTAS 2014*. 2014. Chemical and Biological Microsystems Society.

177. Yasui, T., et al. *Nanowires for early cancer and diabetes diagnosis via micro-RNA detection in urine extracellular vesicles*. in *20th International Conference on Miniaturized Systems for Chemistry and Life Sciences, MicroTAS 2016*. 2016. Chemical and Biological Microsystems Society.

178. Lee, K., et al., *Acoustic purification of extracellular microvesicles.* ACS nano, 2015. **9**(3): p. 2321-2327.

179. Destgeer, G. and H.J. Sung, *Recent advances in microfluidic actuation and micro-object manipulation via surface acoustic waves.* Lab on a Chip, 2015. **15**(13): p. 2722-2738.

180. Rezeli, M., et al., *Comparative proteomic analysis of extracellular vesicles isolated by acoustic trapping or differential centrifugation.* Analytical chemistry, 2016. **88**(17): p. 8577-8586.

181. Evander, M., et al., *Non-contact acoustic capture of microparticles from small plasma volumes.* Lab on a Chip, 2015. **15**(12): p. 2588-2596.

182. Wunsch, B.H., et al., *Nanoscale lateral displacement arrays for the separation of exosomes and colloids down to 20 nm.* Nature nanotechnology, 2016. **11**(11): p. 936.

183. Santana, S.M., et al., *Microfluidic isolation of cancer-cell-derived microvesicles from hetergeneous extracellular shed vesicle populations.* Biomedical microdevices, 2014. **16**(6): p. 869-877.

184. Liu, C., et al., *Field-free isolation of exosomes from extracellular vesicles by microfluidic viscoelastic flows.* ACS nano, 2017. **11**(7): p. 6968-6976.

185. Dudani, J.S., et al., *Rapid inertial solution exchange for enrichment and flow cytometric detection of microvesicles.* Biomicrofluidics, 2015. **9**(1): p. 014112.

186. He, M., et al., *Integrated immunoisolation and protein analysis of circulating exosomes using microfluidic technology.* Lab on a Chip, 2014. **14**(19): p. 3773-3780.

187. Shao, H., et al., *Chip-based analysis of exosomal mRNA mediating drug resistance in glioblastoma.* Nature communications, 2015. **6**: p. 6999.

188. Zhao, Z., et al., *A microfluidic ExoSearch chip for multiplexed exosome detection towards blood-based ovarian cancer diagnosis.* Lab on a Chip, 2016. **16**(3): p. 489-496.

189. Ko, J., et al., *Smartphone-enabled optofluidic exosome diagnostic for concussion recovery.* Scientific reports, 2016. **6**: p. 31215.

190. Chen, C., et al., *Microfluidic isolation and transcriptome analysis of serum microvesicles.* Lab on a Chip, 2010. **10**(4): p. 505-511.

191. Ashcroft, B., et al., *Determination of the size distribution of blood microparticles directly in plasma using atomic force microscopy and microfluidics.* Biomedical microdevices, 2012. **14**(4): p. 641-649.

192. Kanwar, S.S., et al., *Microfluidic device (ExoChip) for on-chip isolation, quantification and characterization of circulating exosomes.* Lab on a Chip, 2014. **14**(11): p. 1891-1900.

193. Zhang, P., M. He, and Y. Zeng, *Ultrasensitive microfluidic analysis of circulating exosomes using a nanostructured graphene oxide/polydopamine coating.* Lab on a Chip, 2016. **16**(16): p. 3033-3042.

194. Soper, S.A., et al., *Fabrication of DNA microarrays onto polymer substrates using UV modification protocols with integration into microfluidic platforms for the sensing of low-abundant DNA point mutations.* Methods, 2005. **37**(1): p. 103-113.

195. Jackson, J.M., et al., *UV activation of polymeric high aspect ratio microstructures: ramifications in antibody surface loading for circulating tumor cell selection.* Lab on a Chip, 2014. **14**(1): p. 106-117.

196. ONeil, C.E., et al., *Interrogating surface functional group heterogeneity of activated thermoplastics using super-resolution fluorescence microscopy.* Analytical chemistry, 2016. **88**(7): p. 3686-3696.

197. Adams, A.A., et al., *Highly efficient circulating tumor cell isolation from whole blood and label-free enumeration using polymer-based microfluidics with an integrated conductivity sensor.* Journal of the American Chemical Society, 2008. **130**(27): p. 8633-8641.

198. Dharmasiri, U., et al., *Highly efficient capture and enumeration of low abundance prostate cancer cells using prostate-specific membrane antigen aptamers immobilized to a polymeric microfluidic device.* Electrophoresis, 2009. **30**(18): p. 3289-3300.

199. Thery, C., et al., *Curr Protoc Cell Biol.* 2006; 22: Chapter 3 (Unit 3), 2006.

200. Jackson, J.M., M.A. Witek, and S.A. Soper, in *Circulating Tumor Cells: Isolation and Analysis*, H. Fan, Editor. 2016, John Wiley & Sons. p. 85-119.

201. Battle, K.N., et al., *Solid-phase extraction and purification of membrane proteins using a UV-modified PMMA microfluidic bioaffinity μSPE device.* Analyst, 2014. **139**(6): p. 1355-1363.

202. Chang, K.-C. and D.A. Hammer, *The forward rate of binding of surface-tethered reactants: effect of relative motion between two surfaces.* Biophysical journal, 1999. **76**(3): p. 1280-1292.

203. Springer, T.A., *Adhesion receptors of the immune system.* Nature, 1990. **346**(6283): p. 425.

204. Rao, C.G., et al., *Expression of epithelial cell adhesion molecule in carcinoma cells present in blood and primary and metastatic tumors.* International journal of oncology, 2005. **27**(1): p. 49-57.

205. Gaster, R.S., et al., *Quantification of protein interactions and solution transport using high-density GMR sensor arrays.* Nature nanotechnology, 2011. **6**(5): p. 314.

206. Shelke, G.V., et al., *Importance of exosome depletion protocols to eliminate functional and RNA-containing extracellular vesicles from fetal bovine serum.* Journal of extracellular vesicles, 2014. **3**(1): p. 24783.

207. Van der Pol, E., et al., *Recent developments in the nomenclature, presence, isolation, detection and clinical impact of extracellular vesicles.* Journal of Thrombosis and Haemostasis, 2016. **14**(1): p. 48-56.

208. Witwer, K.W., et al., *Standardization of sample collection, isolation and analysis methods in extracellular vesicle research.* Journal of extracellular vesicles, 2013. **2**(1): p. 20360.

209. Musante, L., et al., *Recovery of urinary nanovesicles from ultracentrifugation supernatants.* Nephrology Dialysis Transplantation, 2012. **28**(6): p. 1425-1433.

210. Ismail, N., et al., *Macrophage microvesicles induce macrophage differentiation and miR-223 transfer.* Blood, 2013. **121**(6): p. 984-995.

211. Lane, R.E., et al., *Analysis of exosome purification methods using a model liposome system and tunable-resistive pulse sensing.* Scientific reports, 2015. **5**: p. 7639.

212. Bell, G.I., *Models for the specific adhesion of cells to cells.* Science, 1978. **200**(4342): p. 618-627.

213. Yoshioka, Y., et al., *Ultra-sensitive liquid biopsy of circulating extracellular vesicles using ExoScreen.* Nature communications, 2014. **5**: p. 3591.

214. Boenisch, T., *Handbook, immunochemical staining methods*. 2001: Dako Corporation.

215. Haycock, J., *Polyvinylpyrrolidone as a blocking agent in immunochemical studies.* Analytical biochemistry, 1993. **208**(2): p. 397-399.

216. Kim, K.M., et al., *RNA in extracellular vesicles.* Wiley Interdisciplinary Reviews: RNA, 2017. **8**(4): p. e1413.

217. Harris, J.R., et al., *Pathology of Invasive Breast Cancer*, in *Diseases of the Breast*. 2014: Lippincott Williams & Wilkins.

218. Zi, F., et al., *Fibroblast activation protein α in tumor microenvironment: Recent progression and implications.* Molecular medicine reports, 2015. **11**(5): p. 3203-3211.

219. Kamande, J.W., et al., *Modular microsystem for the isolation, enumeration, and phenotyping of circulating tumor cells in patients with pancreatic cancer.* Analytical chemistry, 2013. **85**(19): p. 9092-9100.

220. Chen, W.-T. and T. Kelly, *Seprase complexes in cellular invasiveness.* Cancer and Metastasis Reviews, 2003. **22**(2-3): p. 259-269.

221. Van der Pol, E., et al., *Particle size distribution of exosomes and microvesicles determined by transmission electron microscopy, flow cytometry, nanoparticle tracking analysis, and resistive pulse sensing.* Journal of Thrombosis and Haemostasis, 2014. **12**(7): p. 1182-1192.

222. Filipe, V., A. Hawe, and W. Jiskoot, *Critical evaluation of Nanoparticle Tracking Analysis (NTA) by NanoSight for the measurement of nanoparticles and protein aggregates.* Pharmaceutical research, 2010. **27**(5): p. 796-810.

223. Vestad, B., et al., *Size and concentration analyses of extracellular vesicles by nanoparticle tracking analysis: a variation study.* Journal of extracellular vesicles, 2017. **6**(1): p. 1344087.

224. Chevillet, J.R., et al., *Quantitative and stoichiometric analysis of the microRNA content of exosomes.* Proceedings of the National Academy of Sciences, 2014. **111**(41): p. 14888-14893.

225. Takahashi, K., et al., *Analysis of extracellular RNA by digital PCR.* Frontiers in oncology, 2014. **4**: p. 129.

226. Hindson, B.J., *High-Throughput Droplet Digital PCR System for Absolute Quantitation of DNA Copy Number.* Analytical chemistry (Washington). **83**(22): p. 8604-8610.

227. Michael, A., et al., *Exosomes from human saliva as a source of microRNA biomarkers.* Oral diseases, 2010. **16**(1): p. 34-38.

228. Hunter, M.P., et al., *Detection of microRNA expression in human peripheral blood microvesicles.* PloS one, 2008. **3**(11): p. e3694.

229. Melo, S.A., et al., *Cancer exosomes perform cell-independent microRNA biogenesis and promote tumorigenesis.* Cancer cell, 2014. **26**(5): p. 707-721.

230. Zhou, W., *Cancer-Secreted miR-105 Destroys Vascular Endothelial Barriers to Promote Metastasis.* Cancer cell. **25**(4): p. 501-515.

231. Hayden, R.T., *Comparison of droplet digital PCR to real-time PCR for quantitative detection of cytomegalovirus.* Journal of clinical microbiology. **51**(2): p. 540-546.

232. Taylor, S.C., *Droplet Digital PCR versus qPCR for gene expression analysis with low abundant targets: from variable nonsense to publication quality data.* Scientific reports. **7**(1).

233. Hindson, C.M., et al., *Absolute quantification by droplet digital PCR versus analog real-time PCR.* Nature methods, 2013. **10**(10): p. 1003.

234. Abraham, B.K., et al., *Prevalence of CD44+/CD24−/low cells in breast cancer may not be associated with clinical outcome but may favor distant metastasis.* Clinical cancer research, 2005. **11**(3): p. 1154-1159.

235. Prat, A., et al., *Characterization of cell lines derived from breast cancers and normal mammary tissues for the study of the intrinsic molecular subtypes.* Breast cancer research and treatment, 2013. **142**(2): p. 237-255.

236. Fiskaa, T., et al., *Distinct small RNA signatures in extracellular vesicles derived from breast cancer cell lines.* PLoS One, 2016. **11**(8): p. e0161824.

237. Jia, J., et al., *FAP-α (Fibroblast activation protein-α) is involved in the control of human breast cancer cell line growth and motility via the FAK pathway.* BMC cell biology, 2014. **15**(1): p. 16.

238. Kowal, J., et al., *Proteomic comparison defines novel markers to characterize heterogeneous populations of extracellular vesicle subtypes.* Proceedings of the National Academy of Sciences, 2016. **113**(8): p. E968-E977.

239.	Eitan, E., et al., *Extracellular vesicle–depleted fetal bovine and human sera have reduced capacity to support cell growth.* Journal of extracellular vesicles, 2015. **4**(1): p. 26373.

240.	Uchiyama, Y., et al., *Ultra–sensitive droplet digital PCR for detecting a low–prevalence somatic GNAQ mutation in Sturge–Weber syndrome.* Scientific reports, 2016. **6**: p. 22985.

241.	Galindo-Hernandez, O., *Elevated Concentration of Microvesicles Isolated from Peripheral Blood in Breast Cancer Patients.* Archives of medical research. **44**(3): p. 208-214.

242.	Vaidyanathan, R., et al., *Detecting exosomes specifically: a multiplexed device based on alternating current electrohydrodynamic induced nanoshearing.* Analytical chemistry, 2014. **86**(22): p. 11125-11132.

243.	*Are You Eligible? | Oncotype DX Breast Recurrence Score® | Oncotype IQ®.* 2019 [cited 2019 06/07/19]; Available from: https://www.oncotypeiq.com/en-GB/breast-cancer/patients-and-carers/stage-i-iiia-invasive/eligibility-and-testing.

Appendix

A1. Macro used for measuring EV-MAP micropillar diameter and interpillar spacing.

```
macro "PillarAnalysis_10X [s]" {

dir = getDirectory("Choose a Directory ");
list = getFileList(dir);

setBatchMode(true);

Roi_AverageFeret = newArray(list.length);
Roi_StDevFeret = newArray(list.length);
Roi_AverageInterpillar = newArray(list.length);
Roi_StDevInterpillar = newArray(list.length);

for (k = 0; k < list.length; k++) {
        open(list[k]);
        selectWindow(list[k]);

scale = 0.351; //um/pixel, 10XImage

if(roiManager("count") != 0){
roiManager("deselect");
roiManager("delete");
}

if (isOpen("Mask") == true) {
        close("Mask");
}

run("Duplicate...", "title=Mask");

setAutoThreshold("Default dark");
run("Convert to Mask");
//run("Dilate"); //Dilation included to match Keyence measurements
run("Analyze Particles...", "size=30000-Infinity circularity=0.10-1.00 exclude add");
RoiN = roiManager("count");

Roi_X = newArray(RoiN);
Roi_Y = newArray(RoiN);
Roi_Feret = newArray(RoiN);
Roi_Interpillar_Ave = newArray(RoiN);

for (i=0; i<RoiN; i++){
```

```
        roiManager("select",i);
        List.setMeasurements;
        Roi_X[i]=List.getValue("X");

        roiManager("select",i);
        List.setMeasurements;
        Roi_Y[i]=List.getValue("Y");

        roiManager("select",i);
        List.setMeasurements;
        Roi_Feret[i]=List.getValue("Feret");
}

//For each ROI:
//Find nearest ROI and distance -- Output: Roi_Nearest[i], Roi_NearestDistance[i]
for (i = 0; i < RoiN; i++) {
        interpillar_count = 0;
        interpillar_sum = 0;

        for (j = 0; j < RoiN; j++) {
                distance = sqrt((Roi_X[i]-Roi_X[j])*(Roi_X[i]-Roi_X[j])+(Roi_Y[i]-
Roi_Y[j])*(Roi_Y[i]-Roi_Y[j]));

                if (distance != 0) {
                        if (distance < Roi_Feret[i]*1.75) {
                                interpillar = distance - Roi_Feret[i]/2 - Roi_Feret[j]/2;
                                interpillar_count = interpillar_count + 1;
                                interpillar_sum = interpillar_sum + interpillar;
                        }
                }
        }
        Roi_Interpillar_Ave[i] = interpillar_sum/interpillar_count;
}

//print("Roi Feret Interpillar_Average");
print(list[k]);
for (i=0; i<RoiN; i++){
        print(i, Roi_Feret[i]*scale, Roi_Interpillar_Ave[i]*scale);
}
print("");

Roi_AverageFeret[k] = 0;
Roi_AverageInterpillar[k] = 0;
for (i=0; i < RoiN; i++){
        Roi_AverageFeret[k] = Roi_AverageFeret[k] + Roi_Feret[i];
        Roi_AverageInterpillar[k] = Roi_AverageInterpillar[k] + Roi_Interpillar_Ave[i];
```

141

```
}
Roi_AverageFeret[k] = Roi_AverageFeret[k]/RoiN;
Roi_AverageInterpillar[k] = Roi_AverageInterpillar[k]/RoiN;

Roi_StDevFeret[k] = 0;
Roi_StDevInterpillar[k] = 0;
for (i=0; i < RoiN; i++){
        Roi_StDevFeret[k] = Roi_StDevFeret[k] + (Roi_Feret[i]-
Roi_AverageFeret[k])*(Roi_Feret[i]-Roi_AverageFeret[k]);
        Roi_StDevInterpillar[k] = Roi_StDevInterpillar[k] + (Roi_Interpillar_Ave[i]-
Roi_AverageInterpillar[k])*(Roi_Interpillar_Ave[i]-Roi_AverageInterpillar[k]);
}
Roi_StDevFeret[k] = sqrt(Roi_StDevFeret[k]/(RoiN-1));
Roi_StDevInterpillar[k] = sqrt(Roi_StDevInterpillar[k]/(RoiN-1));


close(list[k]);
}

for (k=0; k < list.length; k++) {
        print(list[k], Roi_AverageFeret[k]*scale, Roi_StDevFeret[k]*scale,
Roi_AverageInterpillar[k]*scale, Roi_StDevInterpillar[k]*scale);
}

setBatchMode(false);


}
```

Table A2. Breast cancer patient demographic and diagnostic information.

Table 6. Clinical information for breast cancer patient samples. Samples were obtained either from the Indian Creek clinic at KUMC or from the KUMC BRCF bank. N/A refers to no testing of the receptor. DCIS = ductal carcinoma in situ, ICD = invasive ductal carcinoma, IMC = invasive mammary carcinoma. Nodal involvement means cancer was found to metastasize into the lymph nodes through biopsy after neoadjuvant therapy. All samples collected in 2019 came from the Indian Creek location of the University of Kansas Cancer Center, while the other samples were collected in 2017 and held in liquid nitrogen in the biorepository.

Pt. ID		age	race	collection date	diagnosis	Receptor status				metastasis	History of therapy prior to draw	
						ER	PR	HER2	Ki67		Chemotherapy/ immunotherapy	Radiation
23126	P1	50-55	white	2017-Apr.	DCIS	(+)	(+)	N/A	Favorable	N	Y	N
25206	P2	60-65	white	2017-Apr.	IDC	(+)	(+)	(-)	Unfavorable	N	Y	N
25180	P3	55-60	white	2017-Apr.	IDC	(+)	(-)	(-)	Unfavorable	Y	Y	N
25335	P4	40-45	white	2017-Jul.	IDC	(+)	(+)	(-)	Favorable	N	N	Y
27854	P5	55-60	white	2017-Nov.	IDC	(+)	(+)	(-)	Favorabe	N	Y	N
28738	P6	55-60	white	2017-Nov.	IDC	(-)	(-)	(-)	Unfavorable	N	Y	N
30613	P7	45-50	white	2019-Jan.	IDC	(-)	(-)	(-)	N/A	N	N	N
30650	P8	35-40	white	2019-Feb.	IMC	(+)	(+)	(+)	Borderline	N	N	N
33987	P9	50-55	white	2019-Mar.	IDC	(-)	(-)	(+)	Unfavorable	N	Y	N
35193	P10	45-50	white	2019-Mar.	IDC	(-)	(-)	(-)	Unfavorable	N	Y	N

A3. Macro for measuring intensity in the EV-MAP microchannels produced from Cy-5 labeled oligonucleotide

```
macro "ChannelIntensity [s]" {

roiManager("reset");

Name=getTitle;
NameDup = "Duplicate";

selectWindow(Name);

run("Subtract Background...", "rolling=50");
run("Duplicate...", "title="+NameDup);

selectWindow(NameDup);
getStatistics(area, mean, min, max, std);

setAutoThreshold("Default dark");
//setThreshold(250, max);
setThreshold(400, max);
setOption("BlackBackground", false);
run("Convert to Mask");
run("Create Selection");
roiManager("Add");

roiManager("Select", 0);
selectWindow(Name);
roiManager("Measure");

selectWindow(NameDup);
close ();
}
```